

ARO 12405.2-EL

LEVEL

(12)

BASIC STUDIES OF HIGH PERFORMANCE MULTIALKALI PHOTOCATHODES

FINAL REPORT (9)

by

Professor Clayton W. Bates, Jr.

March 5, 1979

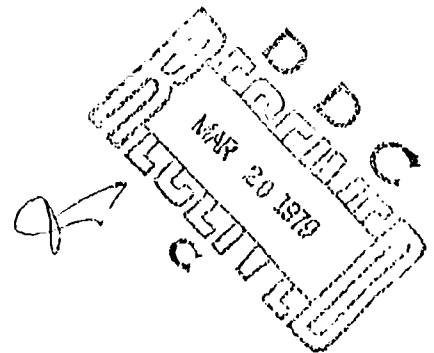
U.S. Army Research Office
Post Office Box 12211
Research Triangle Park, N.C. 27709

Contract DAAG29-75-C-0003
for the period
1 September 1974 - 31 August 1978

Department of Materials Science
and Engineering
Stanford University
Stanford, California 94305

AD A0 66064

DDC FILE COPY



This document has been approved
for public release. Further
distribution is unlimited.

79 03 19 03

Unclassified

SECURITY CLASSIFICATION OF THIS PAGE (When Data Entered)

REPORT DOCUMENTATION PAGE		READ INSTRUCTIONS BEFORE COMPLETING FORM
1. REPORT NUMBER <u>(14) 9</u>	2. GOVT ACCESSION NO.	3. RECIPIENT'S CATALOG NUMBER
4. TITLE (and Subtitle) Basic Studies of High Performance Multialkali Photocathodes		5. TYPE OF REPORT & PERIOD COVERED Final Report 1 September 1974 - 31 August 1978
7. AUTHOR <u>(10)</u> Professor Clayton W. Bates, Jr.		6. PERFORMING ORG. REPORT NUMBER
9. PERFORMING ORGANIZATION NAME AND ADDRESS Department of Materials Science and Engineering Stanford University Stanford, California 94305		8. CONTRACT OR GRANT NUMBER(s) DAAG29-75-C-0003
11. CONTROLLING OFFICE NAME AND ADDRESS U. S. Army Research Office P. O. Box 12211 Research Triangle Park, NC 27709		10. PROGRAM ELEMENT, PROJECT, TASK AREA & WORK UNIT NUMBERS DRXRO-PR P-12405-EL
14. MONITORING AGENCY NAME & ADDRESS (if different from Controlling Office) <u>111</u>		12. REPORT DATE March 5, 1979
		13. NUMBER OF PAGES
		15. SECURITY CLASS. (of this report) Unclassified
16. DISTRIBUTION STATEMENT (of this Report) Approved for public release; distribution unlimited.		15a. DECLASSIFICATION/DOWNGRADING SCHEDULE
17. DISTRIBUTION STATEMENT (of the abstract entered in Block 20, if different from Report)		
18. SUPPLEMENTARY NOTES The view, opinions, and/or findings contained in this report are those of the author(s) and should not be construed as an official Department of the Army position, policy, or decision, unless so designated by other documentation.		
19. KEY WORDS (Continue on reverse side if necessary and identify by block number) Multialkali-antimonide photocathodes; relationship between valence states of components and photoelectric yield; crystal structure of most photosensitive phase; Auger parameter and extraatomic relaxation		
20. ABSTRACT (Continue on reverse side if necessary and identify by block number) X-ray photoemission studies (XPS) of Cs ₃ Sb, Na ₂ KSb, and Na ₂ KSb(Cs) alkali antimonide photocathodes prepared in ultrahigh vacuum on pyrex, suprasil quartz, and stainless steel substrates have been made. The results for these surfaces are the same. Employing the concept of the Auger Parameter we demonstrate that the most photosensitive alkali-antimonide photoemitters are ionic semiconductors with a direct correlation between degree of ionicity and photosensitivity. We further show the dependence of photoemission threshold		

20. Abstract (continued)

on lattice constant and ionicity. It is concluded from these studies that the structure of the most photosensitive s-20 consists of a surface layer of K_2CSb upon a base layer of Na_2KSb and not a monolayer of CS upon Na_2KSb as we commonly thought.

ACCESSION FOR	
NTIS	Section <input checked="" type="checkbox"/>
DOC	Section <input type="checkbox"/>
DATE	<input type="checkbox"/>
BY	
DISTRIBUTION	
A	

PREFACE

This report contains work extending over a four year period on "Basic Studies of High Performance Multialkali Photocathodes" employing the technique of X-ray Photoelectron Spectroscopy (XPS). XPS unlike Auger Electron Spectroscopy is a non-destructive technique resulting in a minimum disturbance of the surface under investigation. It provides information of a qualitative and quantitative nature on charge states and bonding unavailable by other techniques. We have exploited this to obtain a correlation between photosensitivity and valence to obtain a fairly clear picture of the electronic structure of the most photosensitive surfaces. It is the first time that this technique has been used to investigate these materials. For this purpose we have constructed an XPS Spectrometer with a capability of permitting interrogation during any stage of the processing schedule. We have investigated in detail Cs_3Sb , Na_2KSb , and $\text{Na}_2\text{KSb}(\text{Cs})$. Cesium antimonide photoemitters (Cs_3Sb) and $\text{Na}_2\text{KSb}(\text{Cs})$, the S20, are still used in most photoelectronic devices inspite of the large amount of effort that has gone into developing efficient III-V photocathode surfaces. This was the primary motivation for undertaking this study.

No work that we are aware of has studied the correlation of photosensitivity with bonding and much of what is reported here is new. We have emphasized in this study the concept of the Auger Parameter, i.e., the energy difference between the better defined Auger electron and photoelectron peak for an element, which gives information about the

extraatomic relaxation energy due to valence band polarizability at different sites in the crystal lattice. This parameter being the difference in energy between two peaks automatically eliminates any surface charging effects due to highly resistive surfaces.

We have been able to conclusively demonstrate that the most photosensitive alkali-antimonide surfaces are ionic semiconductors, with a direct correlation between the degree of ionicity and photosensitivity. We also show the dependence of photoemission threshold on lattice constant and ionicity. We have also been able to deduce using electron escape depth considerations that the most photosensitive S20 surfaces consist of a surface layer of K_2CsSb upon a base layer of Na_2KSb and not a monolayer or two of Cs upon Na_2KSb as is commonly thought. Na_2KSb with a Cs monolayer produces surfaces of $\sim 100 \frac{\mu a}{\text{lm}}$, whereas K_2CsSb upon Na_2KSb gives surfaces $> 200 \frac{\mu a}{\text{lm}}$.

To make this report as readable as possible most of the theory and derivations are relegated to appendices.

This work was supported by the Army Research Office in Triangle Park, North Carolina and this support is gratefully acknowledged. We would like to thank in particular Dr. Horst Whitman of this office for his patience and consideration throughout the tenure of this grant.

PERSONNEL

In addition to Professor Clayton W. Bates, Jr. two graduate students, Mr. Dhruba DasGupta and Mr. Luis Galan were involved in this project. Mr. DasGupta received the Ph.D. from the Materials Science Department of Stanford University, in December 1978 with a thesis entitled "X-Ray Photoemission Spectroscopy of the Cesium Antimonide Photocathode". A shortened version of this work is being revised for publication in the journal, Thin Solid Films. Mr. Galan is expected to receive the Ph.D. also from the Materials Science Department at Stanford University in March 1979. Two papers are presently being prepared for publication. The title of Mr. Galan's thesis is "X-Ray Photoemission Spectroscopy of Multialkali Antimonide Photocathodes".

TABLE OF CONTENTS

PREFACE	PAGE
PERSONNEL	
I. INTRODUCTION	1-7
II. EXPERIMENTAL TECHNIQUES	8
1. Introduction	8
2. The Photocathode Preparation Chamber	8-11
3. The Sample Wand	11-12
4. The X-ray Source	13-15
5. The Energy Analyzer	16-18
6. The Electron Counter	18-19
7. The Variable Retarding Voltage Generator	19-23
8. The Sample Cage	23
9. Preparation of the Photocathodes	23-24
III. X-RAY PHOTOEMISSION STUDIES OF CESIUM ANTIMONIDE PHOTOEMITTERS	25
1. Introduction	25
2. Results and Discussion	26-40
IV. X-RAY PHOTOEMISSION STUDIES OF MULTIALKALI-ANTIMONIDE PHOTOEMITTERS: BOND IONICITY AND ELECTRONIC STRUCTURE OF ALKALI ANTIMONIDE PHOTOCATHODES FROM XPS	41
1. XPS Spectra of Valence Band Region	41-48
2. Analysis of Electron Binding Energies from XPS	48-54
2.1 Na in Alkali Antimonides. Comparison with Alkali Halides	55-57
2.2 K in Alkali Antimonides. Comparison with Alkali Halides	58-61
2.3 Cs in Alkali Antimonides. Comparison with Alkali Halides	61-65
2.4 Antimony in Alkali Antimonides. Photoemission Threshold Dependence on Lattice Constant and Ionicity	65-67
3. Valence Band Localization from XPS Relaxation Energies	68-70
3.1 Valence Band Electronic Polarizability	71-73
3.2 Comparison of Alkali Halides and Antimonides	73-77
4. Band-Bending and Other Surface Effects	
5. Electronic Structure of Alkali-Antimonides	

TABLE OF CONTENTS (continued)

	PAGE
V. OTHER EXPERIMENTAL EVIDENCE OF IONICITY IN THE ALKALI-ANTIMONIDES	78
1. Photoelectric Emission	78-79
2. Hole Mobility	79-80
3. Crystal Structure	80-86
4. Heats of Formation	87-88
5. Refractive Index	88-90
VI. ANALYSIS OF XPS RELATIVE INTENSITIES. COMPOSITION AND STRUCTURE OF $\text{Na}_2\text{KSb}(\text{Cs})$ PHOTOCATHODES	91-95
VII. CONCLUSIONS	96-99
APPENDICES	

LIST OF APPENDICES, ILLUSTRATIONS AND TABLES

Appendix A	The Basic Physics of X-Ray Photoelectron Spectroscopy
Appendix B	Auger Electrons and the Auger Parameter
Appendix C	The Point Charge Electrostatic Model
Appendix D	Madelung Crystal Field for the Cubic DO_3 Structure

ILLUSTRATIONS

Fig. 1.1	Cubic DO_3 - structure
Fig. 1.2	Hexagonal Na_3Sb structure
Fig. 2.1	Photocathode Preparation Chamber
Fig. 2.2	X-Ray Sources
Fig. 2.3	Experimental Setup
Fig. 2.4	Pulse-Height Discriminator and One-Shot Multivibrator
Fig. 2.5	Active Filter
Fig. 2.6	Linear Voltage Ramp Generator
Fig. 3.1	$\frac{\text{Area under Cs } 5s \text{ peak}}{\text{Area under Cs } 5p \text{ peak}}$ vs. \log_{10} Photosensitivity $\left(\frac{\mu\text{A}}{\text{Lumen}}\right)$.
Fig. 3.2	The Crystal Structure of Cs_3Sb
Fig. 3.3	The Crystal Structure of Cs_3Sb . Comparison of the 5s and 5p XPS data for Xe (gas phase) with those of a good Cs_3Sb photocathode $\left(25 \frac{\mu\text{A}}{\text{Lm}}\right)$.
Fig. 3.4	Valence Band and some Core Level Peaks of a good Cesium Antimonide Photoemitter

Fig. 3.5 Cs4d Doublet

Fig. 3.6 Spectral Yield of Cesium Antimonide Photoemitter

Fig. 3.7 Bond-Orbital Calculation of Cesium Antimonide Band Structure

Fig. 4.1 XPS of Valence Band region of Cs₃Sb

Fig. 4.2 XPS of Valence Band region of K₃Sb

Fig. 4.3 XPS of Valence Band region of Na₂KSb

Fig. 4.4 XPS of Valence Band region of Na₃Sb(Cs)

Fig. 4.5 XPS of Valence Band region of Na₂KSb(Cs)

Fig. 4.6 XPS of Valence Band region of CsI

Fig. 4.7 XPS of Valence Band region of Sb Metal

Fig. 4.8 Comparison of Valence Band region in rhombohedral Sb and Cs₃Sb

Fig. 4.9 Electronic Structure of Cs₃Sb from XPS and UPS Data

Fig. 4.9 Electronic Structure of CsI from XPS Data

Fig. 5.1 Coordination for Sb nearest neighbors in cubic DO₃ - Structure

Fig. 5.2 Coordination for Sb nearest neighbors in hexagonal Na₃Sb - Structure

Fig. 6.1 Band diagram for Na₂KSb

Fig. 6.2 Band diagram for Na₂KSb(Cs)

Table 1.1 Summary of properties of Alkali-Antimonide Photocathodes

Table 4.1 Na1s Binding Energies

Table 4.2 K2p_{3/2} Binding Energies

Table 4.3 Cs3d_{5/2} Binding Energies

Table 4.4 Sb3d_{5/2} Binding Energies

Table 4.5 Photoemission Threshold correlation with Lattice Constant and Valence Charge transfer

Table 4.6 Electronic Polarizabilities

Table 4.7 Polarization Effective Radius for Na^+

Table 5.1 Comparison of Nearest Neighbor Distance and Ionic Radii for some Alkali-Antimonide with DO_3 Structure.

Table 5.2 Comparison of Hexagonal Na_3Sb and Cubic DO_3 structures for Alkali-Antimonides having an Hexagonal phase

1. INTRODUCTION

Since the discovery by Gorlich¹ in 1936 that cesium antimonide has a photosensitivity several orders of magnitude higher than the photocathodes known at that time, the compounds of antimony with the alkali metals have been the subject of considerable technological and scientific research.

In 1955 Sommer^{2,3} discovered that the Na, K alkali antimonide, Na_2KSb , has even higher sensitivity and extended spectral response (to the red). He also found that the addition of Cs to the Na_2KSb photocathode improved further both photosensitivity and spectral response. The $\text{Na}_2\text{KSb}(\text{Cs})$ or S20 photoemissive surface has been since then the most efficient photocathode in technology until the recent development of III-V Negative-Electron Affinity (NEA) photocathodes.

Alkali antimonide photocathodes as Cs_3Sb , Na_2KSb , K_2CsSb , $\text{Na}_2\text{KSb}(\text{Cs})$ are still very important in technology because of their relatively high quantum efficiency combined with a simple synthesis. The fact that they are easily produced in large extended areas and their high efficiency in the semitransparent mode make them irreplaceable in image intensifier tubes and other photoelectronic imaging devices.

Because of the great chemical activity of the alkali metals and even of Sb, alkali antimonide photocathodes have to be processed and kept in very high vacuum, their photoelectric properties are strongly influenced by contamination from residual gases and substrate.

Their processing procedure, found by trial and error, are based on the alkali metal vapor pressure, and their rate of diffusion in antimony and alkali antimonides, both increasing with atomic radius from Na to Cs.

Usually the larger alkali A' is evaporated on a thin film of Sb until peak photoresponse, when A'_3Sb is formed. If $A_2A'Sb$ is to be formed the smaller alkali A is then evaporated until peak photoresponse again. This has been proved from the work of A. Sommer and references to other work may be found in his book.³ The temperatures for the alkali vapor reaction with the substrate are, 200-225°C for Na, 180-150°C for K and Rb and 140-170°C for Cs. At these temperatures the vapor pressure of the corresponding alkali is about 10^{-3} torr and the diffusion rate is just enough to displace larger alkalis and to diffuse into the substrate.

A summary of the properties of the alkali antimonides is given in Table 1.1. These properties are taken from reference 3. A very thorough and complete review of the work done until 1968 is also given in this reference.

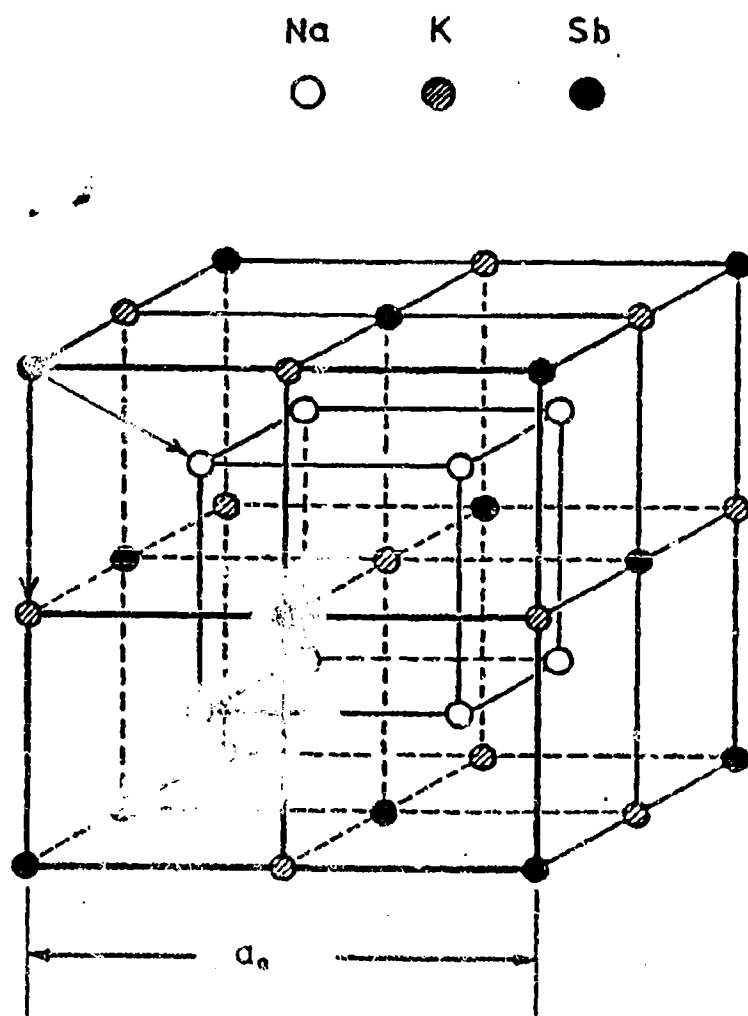
The crystal structure, found from X-ray or electron diffraction, is either cubic DO_3 , Fig. 1.1, or hexagonal Na_3Sb , Fig. 1.2. The photoemission threshold is measured from the spectral dependence of the photoemission yield. From conductivity and absorption spectra the band gap can be determined.

TABLE 1.1

Summary of properties of Alkali Antimonide Photocathodes of the type $(\text{Na}, \text{K}, \text{Rb}, \text{Cs})_3\text{Sb}$

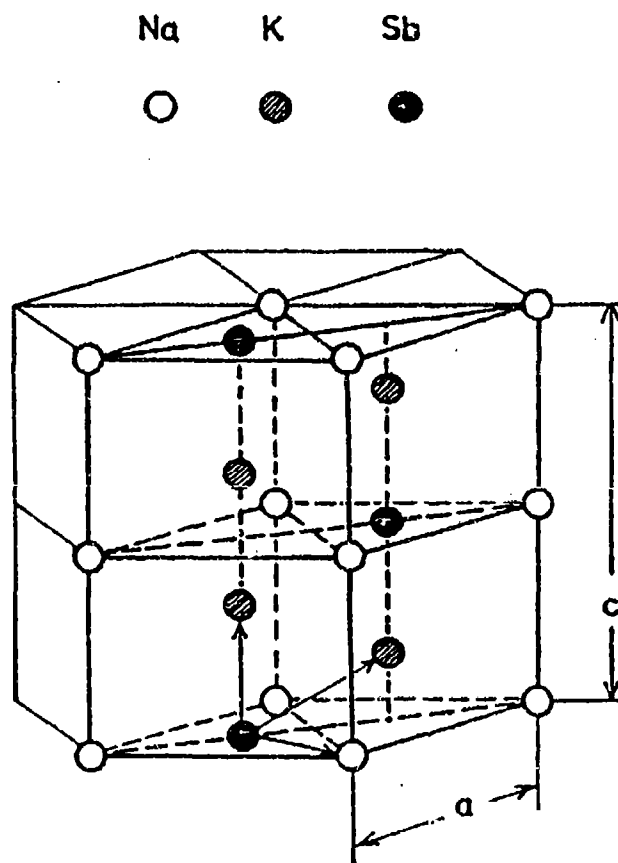
Na_3Sb	Na_2KSb	Na_2RbSb	Na_2CsSb
H $a=5.37$ $c=9.51$ $E_T=3.5$ $E_G=1.1$ n-type $Y_m=0.02$	C $a_s=7.73$ $E_T=2.0$ $E_G=1.0$ p-type $Y_m=0.3$ $60 \mu\text{A/lm}$	 $E_T=1.8$ $E_G=1.0$ $Y_m=0.01$	 $E_T=1.5$ $E_G=0.8$ $Y_m=0.03$
K_2NaSb	K_3Sb	K_2RbSb	K_2CsSb
H $a=5.61$ $c=10.93$ n-type	H $a=6.64$ $c=10.72$ C unstable $a_s=8.49$ $E_T=2.8$ (H) $E_T=2.5$ (C) $E_G=1.1$ (H) $E_G=1.4$ (C) n-type (H) p-type (C) $Y_m=0.07$ (H) $5 \mu\text{A/lm}$ (H) $25 \mu\text{A/lm}$ (C)	 $E_T=2.0$ $E_G=1.2$ $30 \mu\text{A/lm}$	C $a_s=8.61$ $E_T=2.0$ $E_G=1.2$ intrinsic $Y_m=0.3$ $100 \mu\text{A/lm}$
		Rb_3Sb	Rb_2CsSb
		H $a=6.32$ $c=11.19$ C $a_s=8.80$ $E_T=2.2$ (C) $E_G=1.2$ " p-type (C) n-type (H) $25 \mu\text{A/lm}$	C $E_T=1.7$ $E_G=1.5$ $45 \mu\text{A/lm}$
			Cs_3Sb
			C $a_s=9.14$ $E_T=2.0$ $E_G=1.6$ p-type $Y_m=0.2$ $30 \mu\text{A/lm}$

C cubic, a , lattice constant (\AA), Fig 1.1H hexagonal, a, c lattice constants (\AA), Fig 1.2 E_T photoemission threshold in eV E_G band gap in eV Y_m maximum quantum efficiency



CUBIC DO_3 -STRUCTURE OF Na_2KSb

Fig 1.1 Cubic DO_3 - structure of alkali antimonides, showing the two alkali nearest neighbor distances (arrows) for Sb.



HEXAGONAL Na_3Sb - STRUCTURE OF K_2NaSb

Fig 1.2 Hexagonal Na_3Sb -structure of some alkali antimonides, Na_3Sb , K_2NaSb , K_3Sb , Rb_3Sb , showing the three alkali nearest neighbor distances (arrows) for Sb.

Alkali antimonides are believed to be n-type or p-type semiconductors because of excess or defect of alkali. It is also believed that there is a correlation between cubic and p-type alkali antimonides. Good photocathodes are cubic, p-type with surface states producing favorable band bending at the surface.

Alkali antimonides have large absorption constants, if compared with the III-V semiconductor photoemitters, the absorption constant is about one order of magnitude larger within a few tenths of an eV from the absorption edge. They have also large refractive indices about 3.0.

Since its discovery by Sommer there has been some controversy about the role of Cs in the $\text{Na}_2\text{KSb}(\text{Cs})$ photocathode and about its structure.

Spicer³ concluded from his measurements of optical and photoelectric properties that Cs forms a monolayer on the surface of Na_2KSb .

Mac Carrol et al³ observed a small change in the lattice constant from $a_0 = 7.73 \text{ \AA}$ for Na_2KSb to $a_0 = 7.75 \text{ \AA}$ for $\text{NaKSb}(\text{Cs})$, concluding that about 1% by volume of Cs had been incorporated in the volume.

Nimomiya et al³ found a lattice constant of 8.7 \AA .

Hoene³ reported upon the chemical analysis of S-20 photocathodes. He found that the Na to K ratio was significantly smaller than 2 to 1. The Cs content was higher, about 10%, than normally assumed.

First the scanning electron studies of Dowman et al³ and then the X-ray diffraction studies of Dolizy et al³, both "in situ", of the finished photoemitting surface and processing of S-20 photocathodes, finally suggested the S-20 as a polycrystalline, multiphase composite structure of Na_3Sb , Na_2KSb , K_2NaSb , K_3Sb and K_2CsSb . These studies also show the large variations in the relative amounts present of each phase depending on small variations in the processing schedule.

Not too much attention has been dedicated in the past to elucidate the type of binding in alkali antimonide crystals. The proposed models, involve two types of bonds in the lattice of $\text{A}_2\text{A}'\text{Sb}$. $(\text{A}_2\text{Sb})^-$ forming a covalent structure through formation of $(\text{sp})^3$ hybridized orbitals with fourfold coordination typical of III-V covalent semiconductors and the A'^+ ions in the octahedral holes of the covalent $(\text{A}_2\text{Sb})^-$ structure, bonded ionically. This appears to be the prevailing attitude regarding these surfaces. And it is in this area that our efforts were concentrated. On the contrary we will present what we consider fairly conclusive evidence that the most photosensitive alkali-antimonide photocathodes are ionic semiconductors. We demonstrate this first for Cs_3Sb and then later for the S20.

II. EXPERIMENTAL TECHNIQUES

1. Introduction

The system, which has been developed especially for processing and XPS study of alkali antimonide photocathodes, is described in detail. The electron energy analyzer was obtained from Varian Associates and is described in detail in the literature. As such, this part of the apparatus will be described only briefly.

2. The Photocathode Preparation Chamber

A schematic diagram of the chamber is given in Fig. 2.1. It consists of a stainless-steel cylinder 13.0 cm by 10.5 cm dia., one end of which can be sealed by a 6" (15.2 cm.) stainless-steel conflat flange. Metal-ceramic feedthroughs mounted on this flange are used to support a standard setup for photocathode processing. This consists of (i) the various alkali channels; (ii) an antimony bead mounted on a nickel wire; and (iii) a stainless-steel cylinder 2.5 cm by 2 cm dia. with a 1 cm wide lip. The small stainless-steel cylinder serves the purpose of shielding the antimony bead from alkali deposits and also as the collecting electrode (anode) which allows one to monitor the photocurrent while processing. The channels and the Sb-bead are heated electrically from the outside. The alkali metals, because of their high vapor pressure, reach the sample surface by diffusion, whereas Sb atoms, being less mobile, are deposited along a line-of-sight.

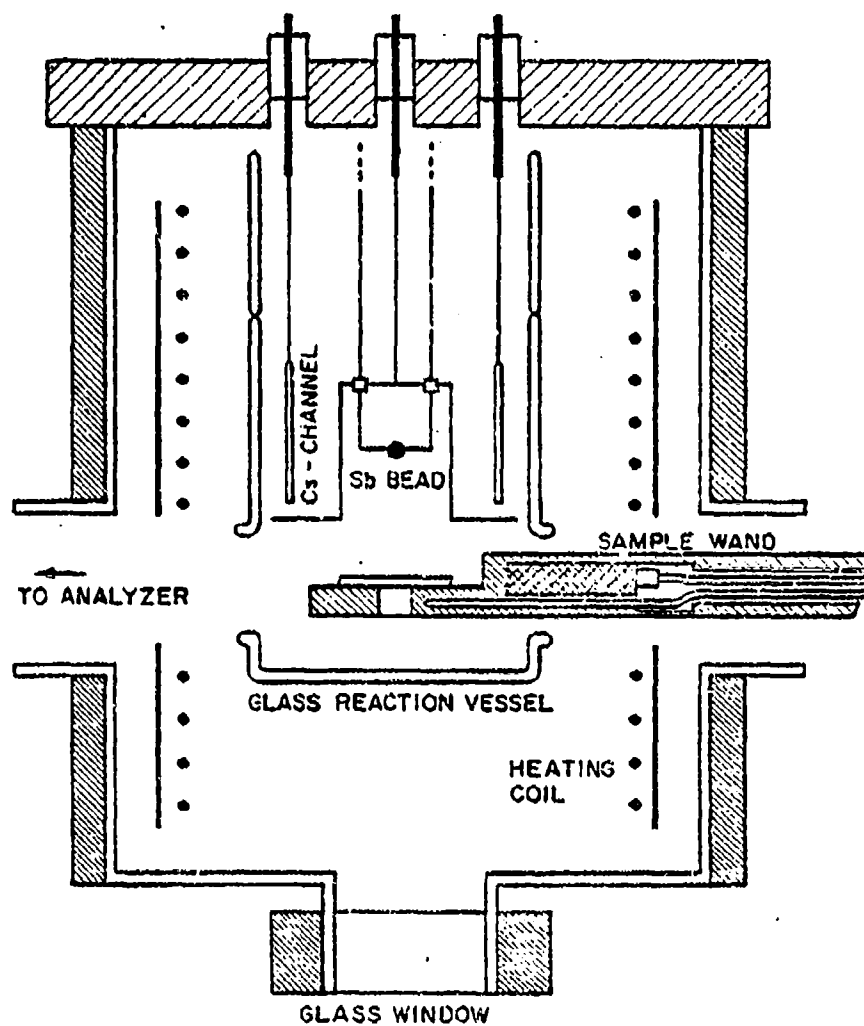


Fig. 2.1 Schematic diagram of the photocathode preparation chamber and the sample wand.

A glass bulb, 7.8 cm by 5 cm dia., closed at one end and with two 2 cm diameter holes opposite one another and 0.5 cm from the closed end, covers the whole arrangement. The purpose of the bulb is to isolate the sample from the UHV pump to a certain extent so that a sufficiently high vapor pressure of the alkalis can be generated and maintained near the sample. This, however, does not obstruct the attainment of an initial ultra-high vacuum (3×10^{-10} Torr) prior to the deposition process, as the pumping can proceed through the open end of the bulb. The two 2 cm diameter holes are necessary for the introduction of the sample wand and its subsequent transfer to the analyzer chamber for investigation. The bulb is surrounded by a cylindrical oven, which is constructed out of 1/1000" (.0254 mm) thick Molybdenum foil mounted with the help of ceramic stand-off insulators on another stainless steel cylinder 10.5 cm by 9 cm dia. with a wall thickness of 1/32" (0.79 mm). The latter is fixed with stainless-steel legs and mounting screws to the flange. The oven is necessary to achieve the proper temperature for processing. The supporting cylinder improves the efficiency of heating by cutting down the radiation loss. It has three 3 cm diameter holes on its curved surface, two facing one another for passage of the sample wand as mentioned before, and the other for providing a low-conductance path to the UHV pump.

The above design permits a rapid dismantling and reassembly of the constituent parts when replacement of the exhausted channels and/or the Sb-bead becomes necessary. The flat side of the outer stainless-steel cylinder opposite the 6" (15.2 cm) flange is sealed with a stainless-steel plate 1/2" (1.27 cm) thick and on which a 2 3/4" (6.99 cm) conflat flange has been welded. This flange is closed by a glass window mounted on a similar flange. The window lets light into the chamber and onto the sample surface, in order that the photocurrent can be measured while processing continues.

The curved side of the outer cylinder has also three ports terminated by 2 3/4" conflat flanges. Of these, two, situated opposite one another, permits the preparation chamber to be connected through a straight-through valve to the analyzer chamber on the one side, and through a polyimide low-conductance seal, to the backing pressure chamber on the other. The third port, at right angles to the other two, permits connection to the 80 litres/sec. UHV pump. Heating tape is wound around the preparation chamber. In addition to helping one carry out a proper degassing of the inner walls of the chamber, this allows, in conjunction with the inner oven and sample heater, the temperature to be raised to a preset value.

3. The Sample Wand

The sample wand permits easy transfer of the sample from the preparation chamber to the analyzer and vice versa, while maintaining both chambers in ultra-high vacuum. It is important to keep the two

chambers separate as any deposit of the alkali metals on the analyzer parts can change its work function and, as a result, its calibration. The wand also serves to hold the sample heating cartridge and the thermocouple for measuring the sample temperature.

A schematic diagram is given in Fig. 2.1. A stainless-steel tube, 1/2" (1.27 cm) outer diameter by 1.5 meters long and .095" (2.413 mm) wall thickness is welded onto a stainless-steel "head" constructed out of a stainless-steel rod of the same diameter and 2 3/4" (6.99 cm) long. The other end of the rod is cut longitudinally into half up to a length of 1 1/8" (2.86 cm). The flat side thus obtained is used to hold the sample substrate with the help of a 3/8" by 5/8" (9.53 mm by 15.88 mm) stainless-steel frame and mounting screws. It has also a 1/4" (6.34 mm) dia. hole drilled at the center to allow light to be incident on the photocathode from the substrate side when it is to be used in the semitransparent mode.

The heater cartridge and the tip of the thermocouple are positioned inside cylindrical holes drilled inside the solid stainless-steel head so that they are situated as near the substrate as possible. This is especially important for the thermocouple as it is necessary to measure the substrate temperature as accurately as possible for proper processing of the photocathode. The cartridge is in the form of a cylinder 1/4" (.635 cm) dia. by 1" (2.54 cm) long and has a capacity of 100 watts. The thermocouple is a standard chromel-alumel type mounted inside a stainless-steel sheath 1/16" (1.59 mm) in diameter. The connections for the cartridge and the thermocouple are brought outside through the hollow part of the sample wand.

4. The X-ray Source

The X-ray source was designed so that it can project inside the analyzer chamber with the anode situated as close to the sample surface as practicable. This is to ensure a sufficiently high X-ray intensity being incident on the sample.

Figure 2.2 shows the arrangement. The anode is a hollow wedge-shaped piece of copper, 1 3/4" (4.45 cm) long and with a cross-section roughly equal to 1/4" (.635 mm) square, on which highly pure (99.9999%) Aluminum is deposited to a thickness of about 25 μ m by sputtering. This particular arrangement is used to provide adequate cooling of the anode surface. The cooling water passes through two 1/4" (.635 mm) copper tubes welded to the side of the anode. The cathode consists of two tungsten filaments .007" (.18 mm) dia. and 1 1/2" (3.81 cm) long situated at a distance of 1/8" (3.18 mm) from each other and parallel to each other and the anode. There is a grounded shield of tantalum in between the anode and the tungsten filaments, which produces a suitable distribution of field lines in order that the emitted electrons follow a curved trajectory and strike the proper (oblique) face of the anode. The whole assembly is encased in a grounded stainless-steel housing. The purpose of the housing is twofold; first, it isolates the UHV analyzer chamber from the relatively higher pressure present ($\approx 10^{-8}$ Torr) near the (hot) X-ray source. Secondly, the positively charged

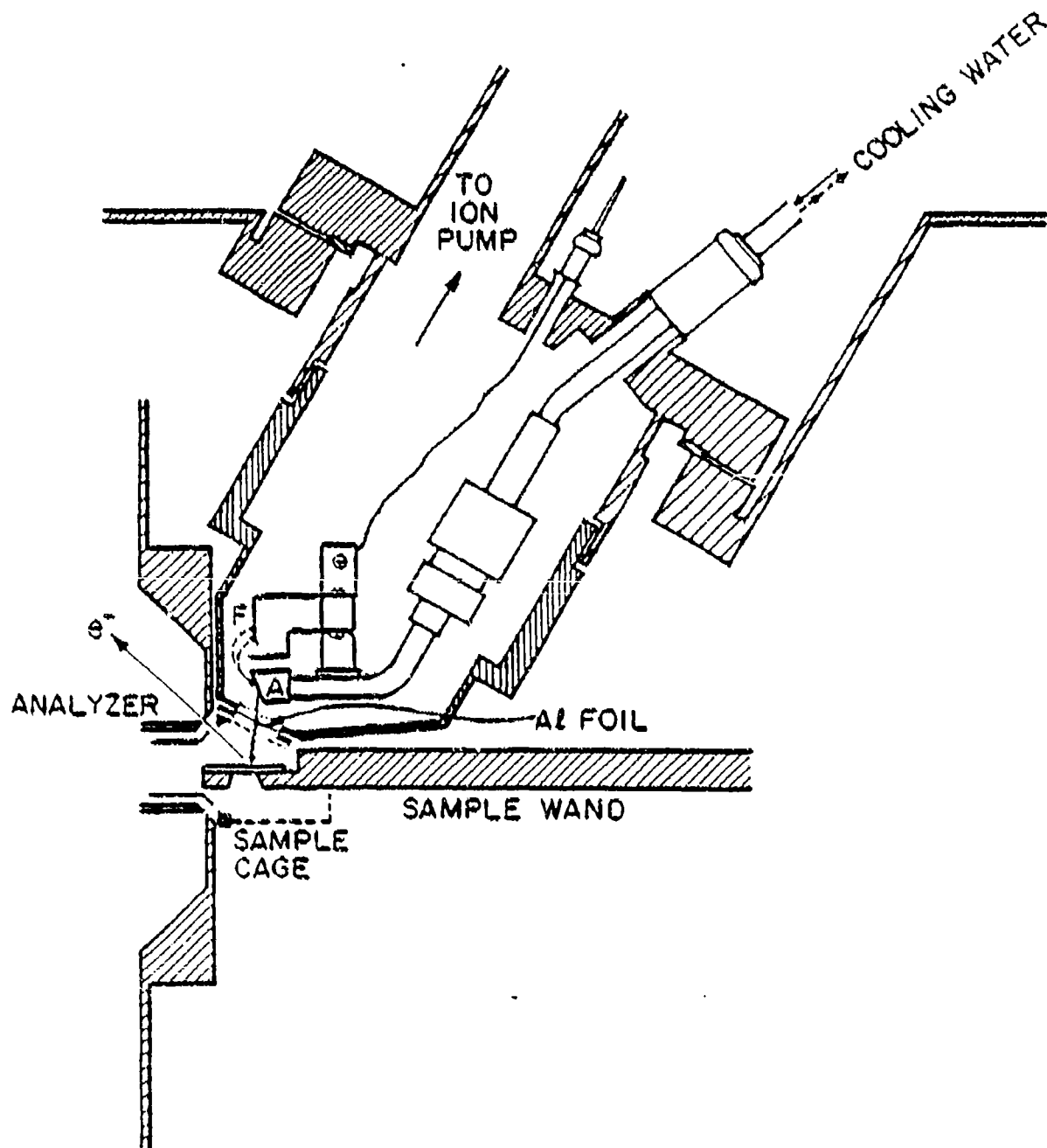


Fig. 2.2 Schematic diagram of the X-ray source. A, Copper Anode; F, Tungsten Filaments.

anode produces a corresponding negatively charged image, the repulsive effect of which serves to confine the electrons to the space between the housing and the anode. Thus, thermally emitted electrons which would otherwise be lost are brought back and forced to strike the anode, thereby increasing the efficiency of the X-ray source. Use of the two separately positioned filaments instead of only one was found necessary to counteract the space-charge effects which prevent one from drawing a sufficiently high anode current (and thereby obtaining enough X-ray intensity) with a reasonable amount of heating current in the cathode.

The anode cooling tube (which also serves as the electrical connection to the anode) and the cathode terminals are brought out through appropriate ceramic feedthroughs mounted on a 6" (15.2 cm) conflat flange. A bent piece of standard 1 1/2" (3.81 cm) dia. stainless-steel vacuum tubing, also welded to the flange, connects the assembly to a 20 liter/sec. Vacion pump. The pressure obtained in the X-ray chamber, after pump-down and necessary bakeout was 6×10^{-8} Torr.

A 12 KV, 100 mA Power Supply which also supplies the heating current for the filament was obtained from Varian Associates. The Power Supply also has provisions to regulate the filament heating current so that the anode current can be maintained at a constant, preset value. With a filament current of 5 amps, an X-ray current of 100 mA could be easily obtained at 12 KV.

5. The Energy Analyzer

The Electron Energy Analyzer (EEA) is the same as used in the Varian IEE spectrometer. It consists of a double-sphere electrostatic deflector followed by a cylindrical condenser. The spherical conductors, which occupy the region between polar angles (with the sample-image line as axis) 45° and 135° , have diameters of $6\frac{1}{2}$ " (16.51 cm) and 8" (20.32 cm). The cylindrical condenser has the following specifications: inner cylinder, $3\frac{1}{2}$ " (8.89 cm) by $1\frac{3}{4}$ " (4.45 cm) dia.; outer cylinder, $4\frac{1}{2}$ " (11.43 cm) by $3\frac{3}{4}$ " (9.53 cm) dia. (all of the above figures represent outside dimensions for the inner electrode and vice versa). The electrons coming from the sample are focused, first on the exit slit of the spherical analyzer, and then focused again, after passage through the condenser, upon the electron multiplier. To provide for the correction of any mismatch between the image formed by the spherical analyzer and the corresponding exit slit, a set of eight sector-shaped electrodes are used, the potential of which can be varied individually to obtain the maximum sensitivity. All the necessary electrode potentials are derived from a Hewlett-Packard 6116A Power Supply and a suitably designed voltage divider. By changing the output voltage of the power supply, the nominal voltage for which the analyzer is set can also be adjusted from 10-100 eV. The total linewidth is approximately 1 eV taking into account the contribution from the AlK α X-ray line.

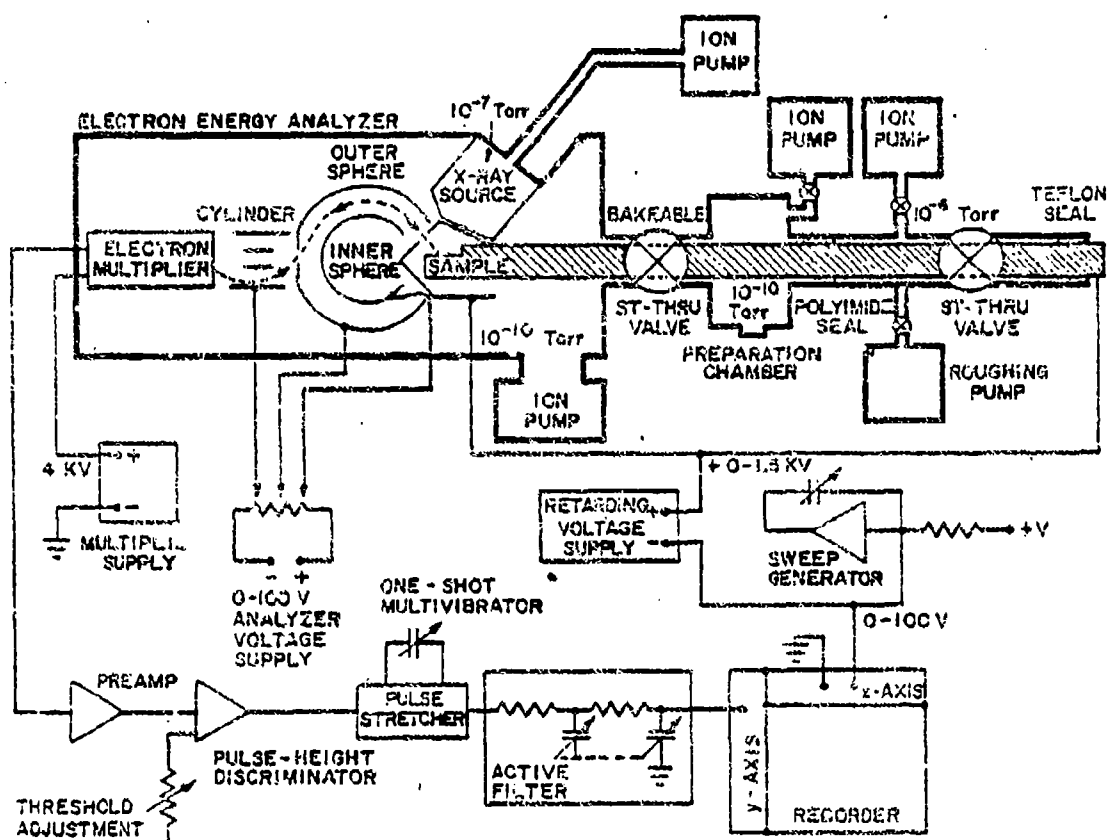


Fig. 2.3 Block diagram of the complete experimental set-up.

The usual method of recording an XPS spectrum is to vary the retarding voltage applied to the photoemitted electrons with respect to time, keeping the analyzer electrodes at a constant potential. This method has the following two advantages: (i) the resolution of the spectrometer remains the same at all portions of the spectrum; and (ii) the net dependence of sensitivity is inversely proportional to the analyzer energy, which means that retardation has an enhancing effect on the sensitivity.

6. The Electron Counter

A block diagram of the counting arrangement appears in Fig. 2.3. The purpose of the counter is to develop a voltage which is proportional to the number of electrons arriving per second through the analyzer.

An EMI 9603/2B type electron multiplier tube (EMT) is mounted inside the analyzer assembly so that the electrons coming out of the analyzer are focused on it. The dynodes of the EMT are connected, through a resistor chain also situated in UHV, to a 4 kV, 500 μ A Power Supply.

The output pulses from the EMT have a height of the order of 300 mV. These are first passed through a discriminator, which has an adjustable level setting. Thus, only those pulses which have a height equal to or greater than a specified value (usually 100 mV) appear at the output of the discriminator. The discriminator output is a series

of pulses of constant height (5 V). These are then used to trigger a one-shot multivibrator, whose time period can be varied from 0.5 μ s to 400 μ s in 12 approximately equal steps (Fig. 2.4).

The DC component of the one-shot multivibrator output is a measure of the repetition frequency of the pulses, i.e., the number of electrons arriving through the analyzer per second. These are fed into an active filter built around an NE 536 Op Amp (Fig. 2.5), the time constant of the filter being variable in 6 steps from 20 seconds to .1 sec. The filter has provision for offset adjustment of the output voltage by 0.1 V. The filter output is connected to the Y-terminals of an X-Y recorder for recording the XPS spectra.

7. The Variable Retarding Voltage Generator

The retarding (positive) voltage, applied to the sample cage and the sample wand, has to be varied over a certain range to scan a definite portion of the photoemission spectrum of the same width. This is achieved by connecting a precision variable setting power supply in series with a ramp generator.

The power supply is a COHU model 326 programmable DC voltage standard, with a precision of less than 50 mV, and whose output can be set from 0 to ± 1355 volts in steps of 1 volt. The ramp generator is shown in Fig. 2.6. It is a simple Miller integrator built out of an Analog Device 118A precision Op Amp and an RCA 40012 field-effect transistor. The output of the ramp generator varies from 0 to 100 V with the rate of increase of voltage variable from 25 V/sec. to .005/sec. in 12 roughly equal steps.

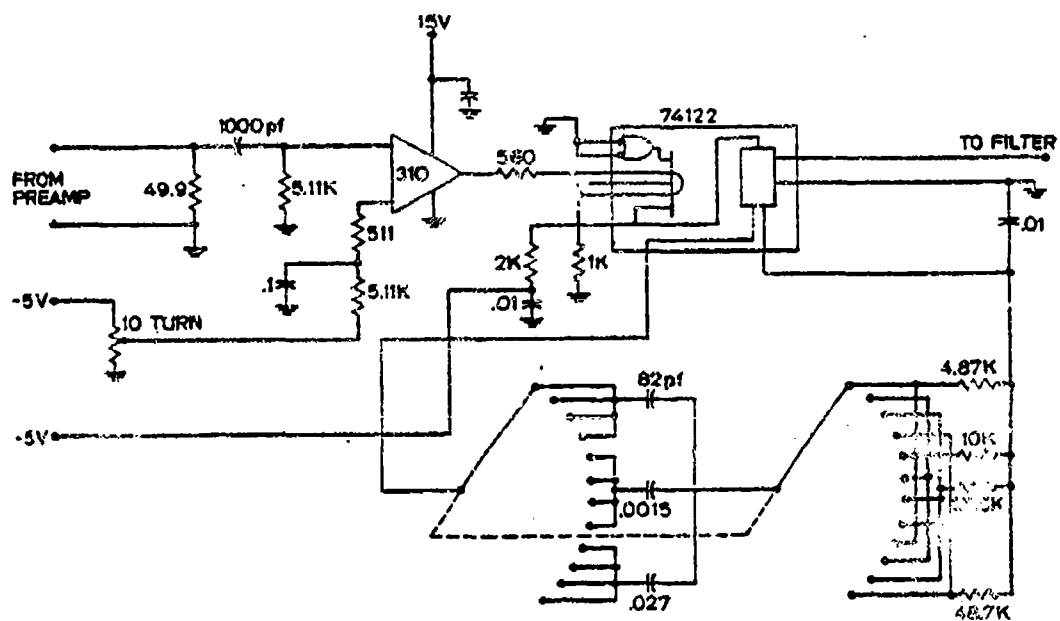


Fig. 2.4 Circuit diagram of the Pulse-height Discriminator and the One-shot Multivibrator.

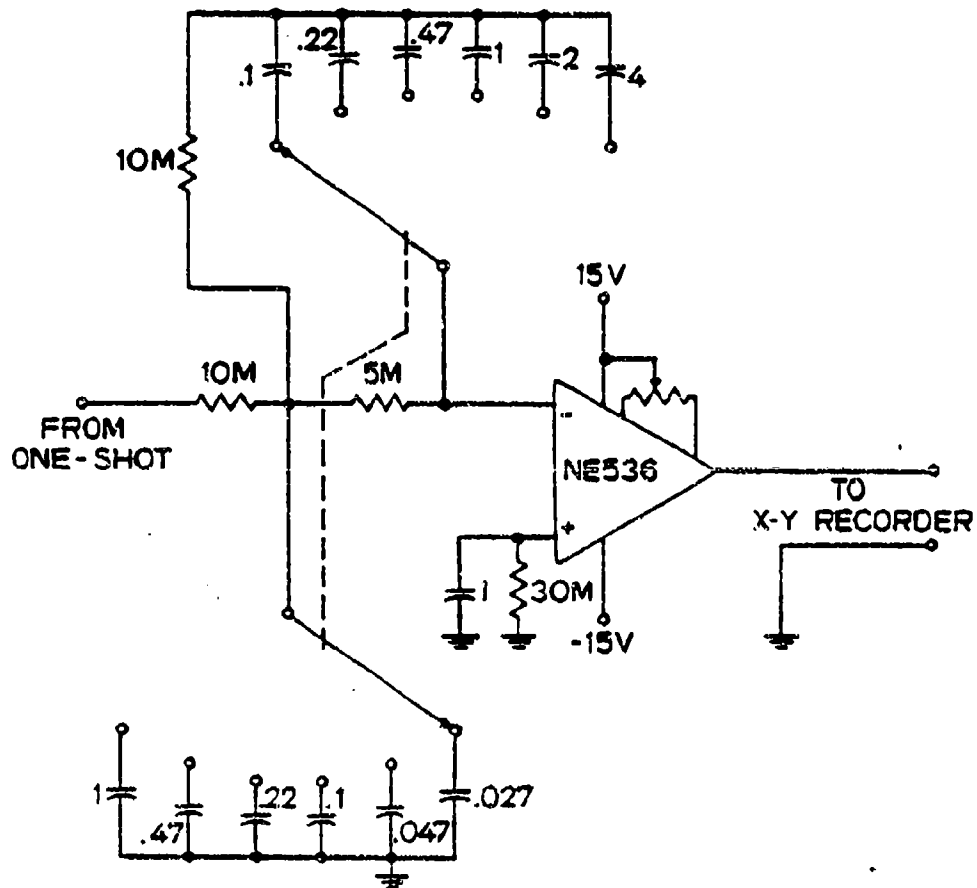


Fig. 2.5 Circuit diagram of the Active Filter.

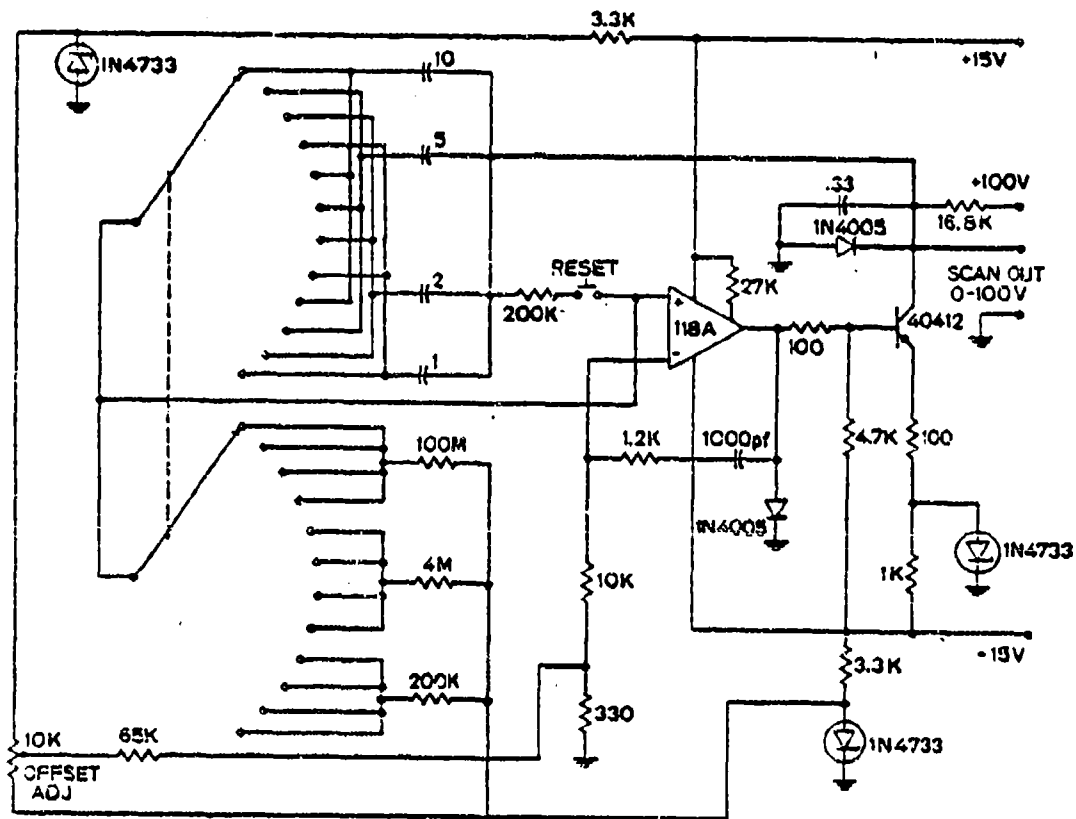


Fig. 2.6 Circuit diagram of the Linear Voltage Ramp Generator.

8. The Sample Cage

The Sample Cage, which is also connected to the variable retarding voltage, acts as an electrostatic shield around the sample. In this way, electrons coming out from different parts of the sample experience the same retarding potential. The cage is built out of .03" (.76 mm) thick perforated stainless-steel, with holes cut out in it to permit X-ray and UV beams to be incident on the sample (Fig. 2.2).

9. Preparation of the Photocathodes

Fifteen Cs_3Sb photocathodes of $25 - 100 \frac{\mu\text{a}}{\text{cm}^2}$, ten Na_2KSb of $30-50 \frac{\mu\text{a}}{\text{cm}^2}$, twenty $\text{Na}_2\text{KSb}(\text{Cs})$ (S20) of $100-250 \frac{\mu\text{a}}{\text{cm}^2}$, five Na_3Sb , five $\text{Na}_3\text{Sb}(\text{Cs})$, and five K_3Sb photoemitting surfaces were studied. They were prepared by variations of the techniques described by A. Sommer in his book "Photoemissive Materials". Their properties are described in following portions of this report.

Prior to the actual deposition of a photosurface, the preparation chamber was subjected to a degassing bake-out according to the following schedule. First, the current in the three heaters were slowly increased, over a period of about six hours, until the temperatures of the outside wall of the chamber and the substrate reached nearly 250°C and 400°C , respectively. The channels were then outgassed by passing currents through them successively until they fired for 1 minute. The channel currents were then shut off. The system was then allowed to

bake out for 24 hours at the same temperature settings. Finally, the heating currents were turned down so that the proper temperatures necessary for processing were reached.

III. X-RAY PHOTOEMISSION STUDIES OF CESIUM ANTIMONIDE PHOTOEMITTERS

1. Introduction

X-ray photoemission spectra (XPS) of cesium antimonide¹⁻⁶ photo-surfaces prepared in ultrahigh vacuum on pyrex, suprasil quartz and stainless steel substrates have been measured. The experiments indicate that the results for these surfaces are the same for cesium antimonide photocathodes as well as for the S20. Cesium antimonide but not S20 surfaces were also prepared in an HP 5950A ESCA spectrometer with monochromatized AlK α . Other than improved resolution (0.8 eV vs. 0.6 eV) with the HP unit no differences were observed between the spectra obtained with the two instruments. The spectral yield measurements were taken with a calibrated tungsten light source and filters. Corrections were made for the transmission of light through the glass windows on the vacuum chambers but reflection losses were neglected. Those features of XPS that are associated with a high photosensitivity were studied in the following manner. A Cs₃Sb photo-surface was prepared and then progressively destroyed by baking it at progressively higher temperatures (>150°C). This was done because experiments indicated that whether the photosensitivity was produced by "processing" (these procedures have been discussed previously³) or heating a processed surface to produce one of lower sensitivity, the results are essentially the same. The photosensitivity and the XPS data were recorded after every step.

2. Results and Discussion

A very close relationship between the intensity of the Cs5s-level XPS peak and the photosensitivity was found to exist. A high photosensitivity was invariably associated with an extremely weak Cs5s peak. As the photosensitivity dropped as a result of baking, the Cs5s peak increased in intensity. These results are shown in Fig. 3.1 where the ratio of the area under the Cs5s peak to that of the nearby Cs5p peak is plotted as a function of \log_{10} photosensitivity in microamps per lumen. This shows an almost linear relationship over five orders of magnitude for the photosensitivity.

Satellite peaks were observed very clearly on the lower-kinetic-energy side of the strongest Cs3d peaks, and less prominently to the left of the other Cs and Sb 4d peaks. These were separated from the main peak positions by about 7 eV. They were also observable most clearly with a good photosensitive surface. They were identified as being due to excitation of plasma oscillations of the valence-band electrons produced by the passage of the photoexcited electron through the solid. An attempt will now be made to explain these results.

The crystal structure of Cs_3Sb was originally determined by Jack and Wachtel.⁷ Their structure was somewhat disordered compared to the one that is currently accepted as being associated with the most

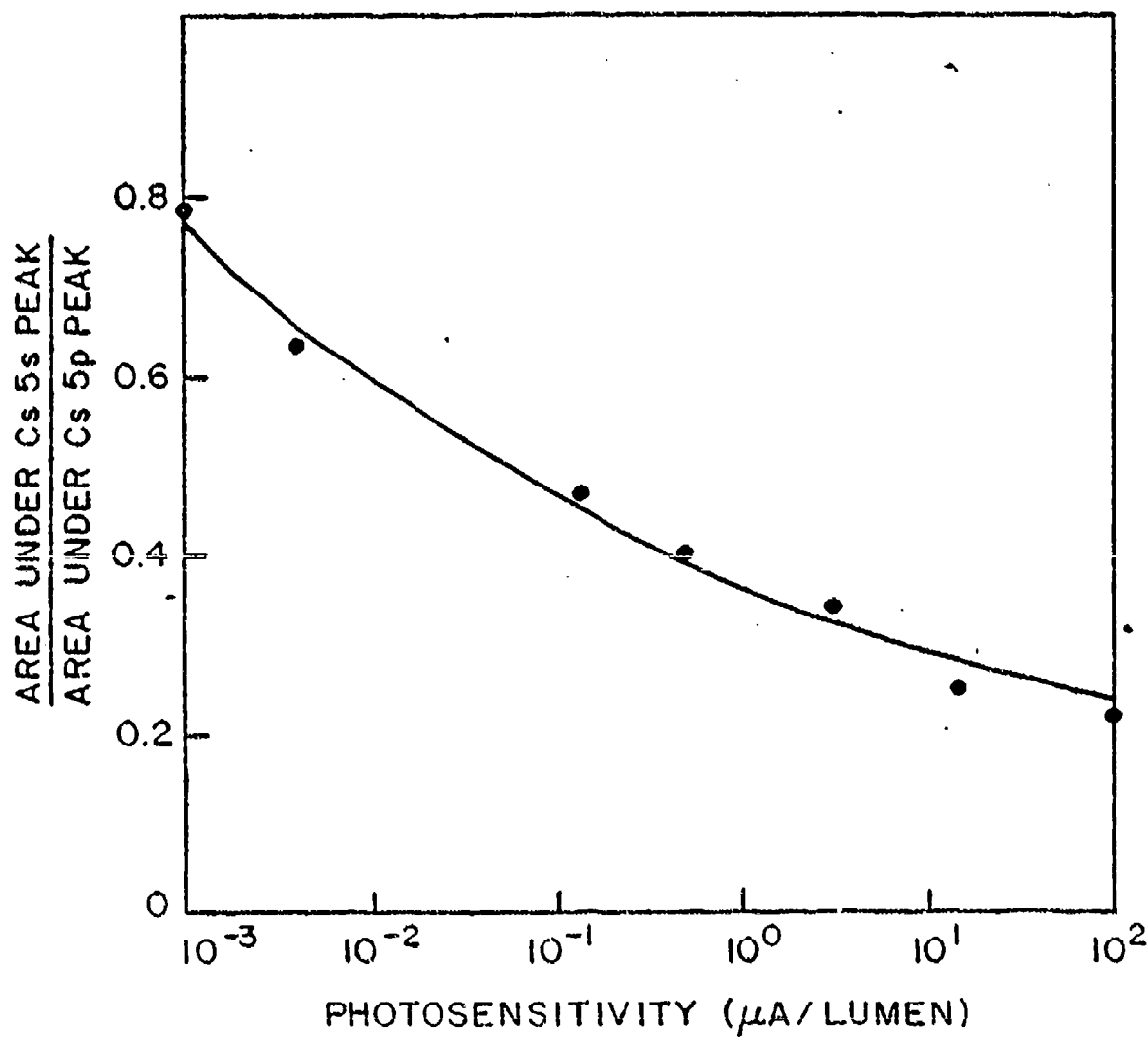


Fig. 3.1 $\frac{\text{Area under Cs 5s peak}}{\text{Area under Cs 5p peak}}$ vs. Log Photosensitivity ($\frac{\mu\text{A}}{\text{Lumen}}$).

photosensitive surfaces.^{6,8,9} We show the latter in Fig. 3.2. All research to date has described the most photosensitive Cs_3Sb as a "normal valency" intermetallic compound, being classified as neither wholly ionic, nor metallic, Jack and Wachtel⁷ had some of the Cs covalently bonded to Sb and some as Cs^+ . This is the commonly accepted theory for this surface. From a close look at the results obtained with XPS, this conjecture does not appear to be a correct one for the following reasons.

The loss of intensity of Cs5s peaks is explained as being due to Cs being present in the substance mostly as Cs^+ ions. Cs and Sb have a fairly large electronegativity difference (1.2). Thus there is a strong tendency for charge separation from the Cs to the Sb.

The photoexcitation of a 5s electron in Cs^+ ion is accompanied by a large probability of configuration interaction (CI) of the excited state with a large number of possible final states which, although having the same values of the quantum numbers $L, S(\text{total})$, differ in their individual electronic configuration. Since the alkali metal ions are isoelectronic with the rare gases, one expects from atomic considerations similar behavior with regard to the production of satellite structure.

Similar existence of strong satellites with accompanying loss of intensity of the main peak have been observed in other alkali ions in the alkali halides and in closed-shell atoms such as Xe. Xe is isoelectronic with Cs^+ and the peak positions and intensities are found

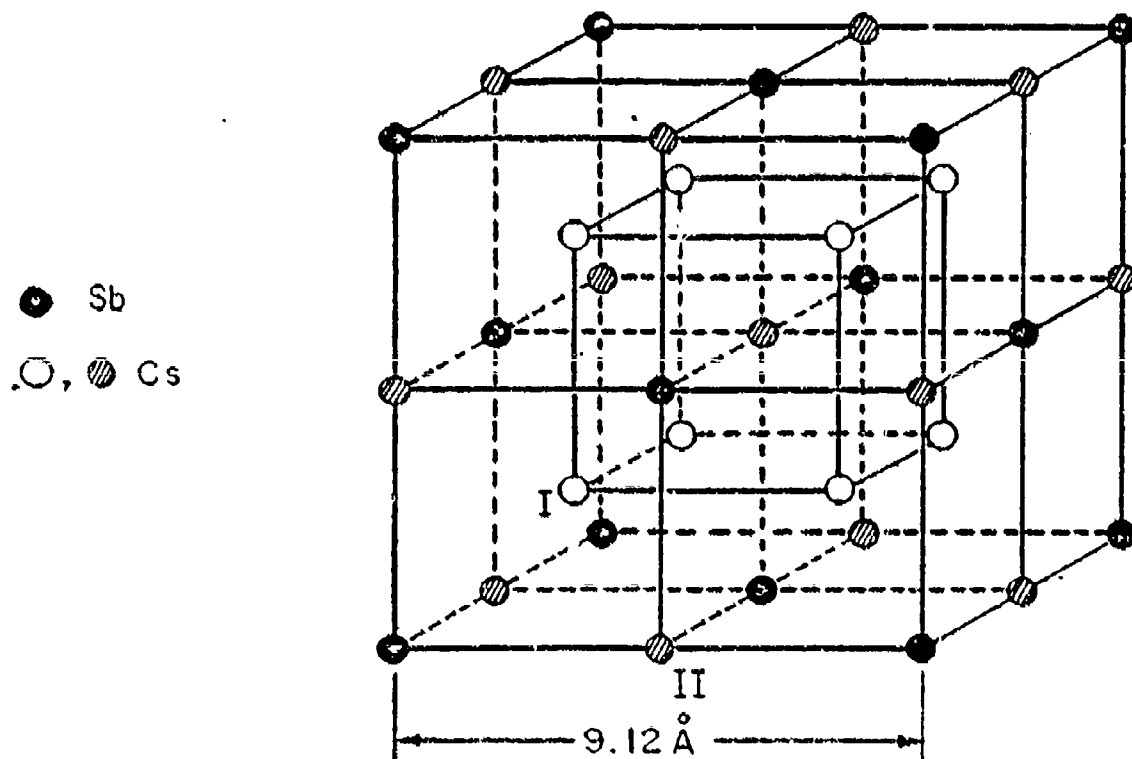


Fig. 3.2 The Crystal Structure of Cs_3Sb .

to match very well (Fig. 3.3). We do not observe the satellites in cesium antimonide because of the presence of the Sb4d that obscures them.

The fact that in a good Cs_3Sb photocathode, the Cs5s peak is quite weak indicates that almost all of the Cs is present as Cs^+ ions. Cs metal itself has a fairly strong 5s peak. Thus, if any nonionized Cs were present a reasonably intense Cs5s peak would be observed. It is probable that as the photosurface is destroyed by baking, Cs^+ ions diffuse towards the surface, giving rise to a thin surface film of metallic Cs which is responsible for the gradual rise in the Cs5s peak intensity with decreasing photosensitivity.¹⁰ This agrees with our observations that as the surface is destroyed by baking, the Cs and Sb shift to their free metal values.

W. E. Spicer⁴ found in his photoconductivity studies on Cs_3Sb photoemitters ionic conduction to be the overwhelming conduction taking place.

We measured the Auger parameters¹¹ for Cs in CsI thin films and Cs in the photosensitive Cs_3Sb surfaces and found 191.0 eV and 190.25 eV respectively, both results evidence for the Cs^+ model we are proposing. We also note in passing that we have been referring to Cs^+ as though whole electronic charges are transferred. What we really mean is that the dominant character is ionic with ~0.6 to 0.8 electronic charges being transferred as in the case of CsAu, an ionic semiconductor, where

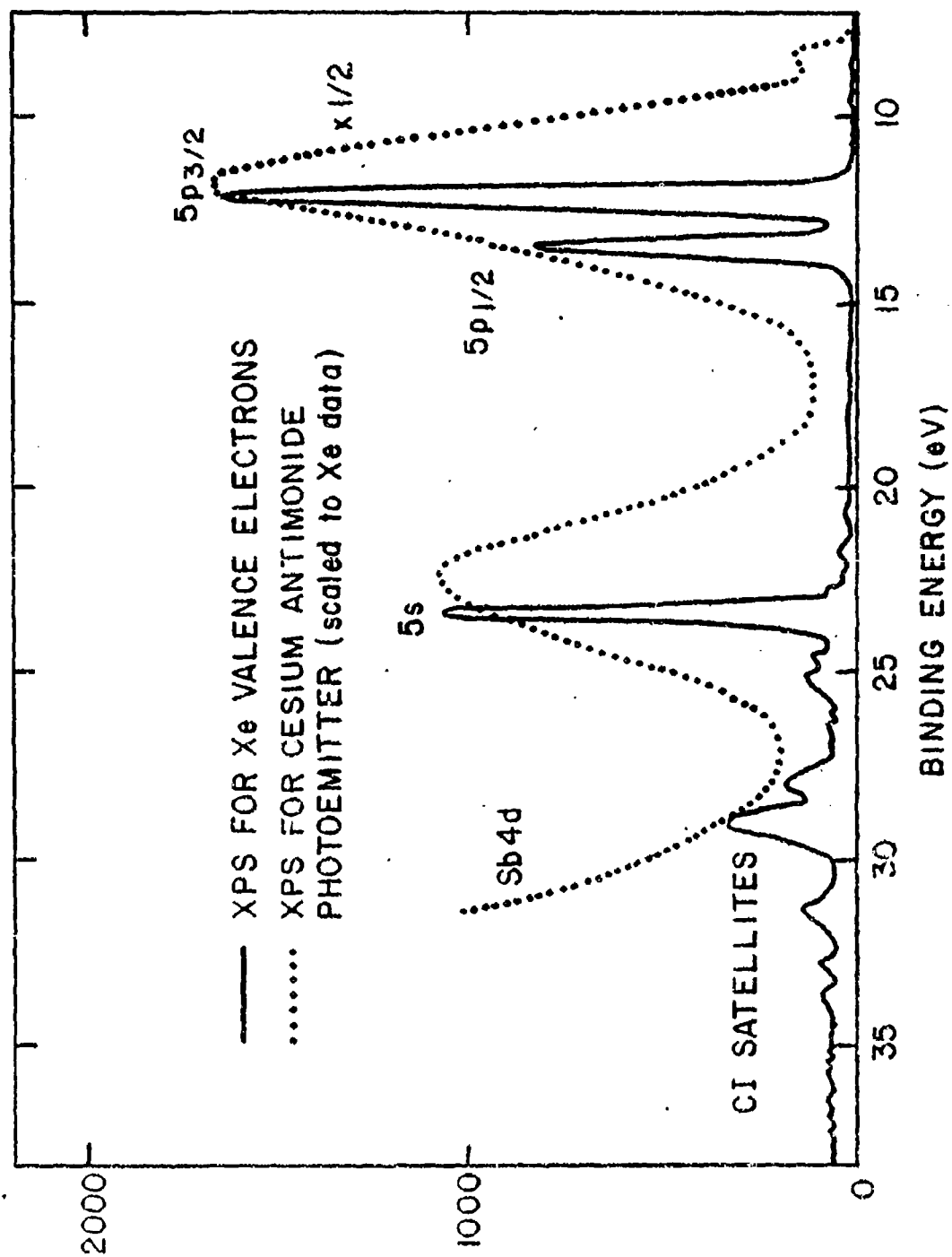


Fig. 3.3 The Crystal Structure of Cs_3Sb . Comparison of the 5s and 5p XPS data for Xe (gas phase) with those of a good Cs_3Sb photocathode ($25 \frac{\mu\text{A}}{\text{Lm}}$).

the calculated charge transfer from the Cs to the Au was found from the experimental data to be $\sim(0.6 \pm 0.2)$ electronic charges.¹²

Additional evidence for the ionic character of cesium antimonide is given in Fig. 3.4 where we show the XPS data for the valence band and the Cs5p, Cs5s, and Sb4ds core levels for a good cesium antimonide photoemitter. As can be seen from the figure the valence band (Sb5p) is approximately 2 eV wide. This is to be contrasted with the valence band for Sb metal which is approximately 5.5 eV in width. The shape and width of the valence band can be compared with the valence band of LaSb which is also triangular in shape and 2 eV wide.¹³ LaSb is an ionic compound with the rock salt crystal structure. There is a reasonably clear splitting of about 0.4 eV in the XPS data corresponding to the two different types of Cs-atoms (marked I and II in Fig. 3.2). This is shown in Fig. 3.5 for the Cs4d doublet. Experiments performed on the HP 5950 ESCA spectrometer with monochromatized AlK α on two good cesium antimonide surfaces with one inclined 22-1/2° with respect to the other, showed that the same two Cs configurations existed in the surface region as well as in the bulk. If there is an additional Cs configuration on the surface, the present technique is not capable of revealing it, either through lack of resolution, or it is obscured (because of its low intensity by the main cesium peaks).

The inherently large width (~ 1.4 eV at half-maximum) of the XPS peaks made any definite conclusion about the extent of band-bending

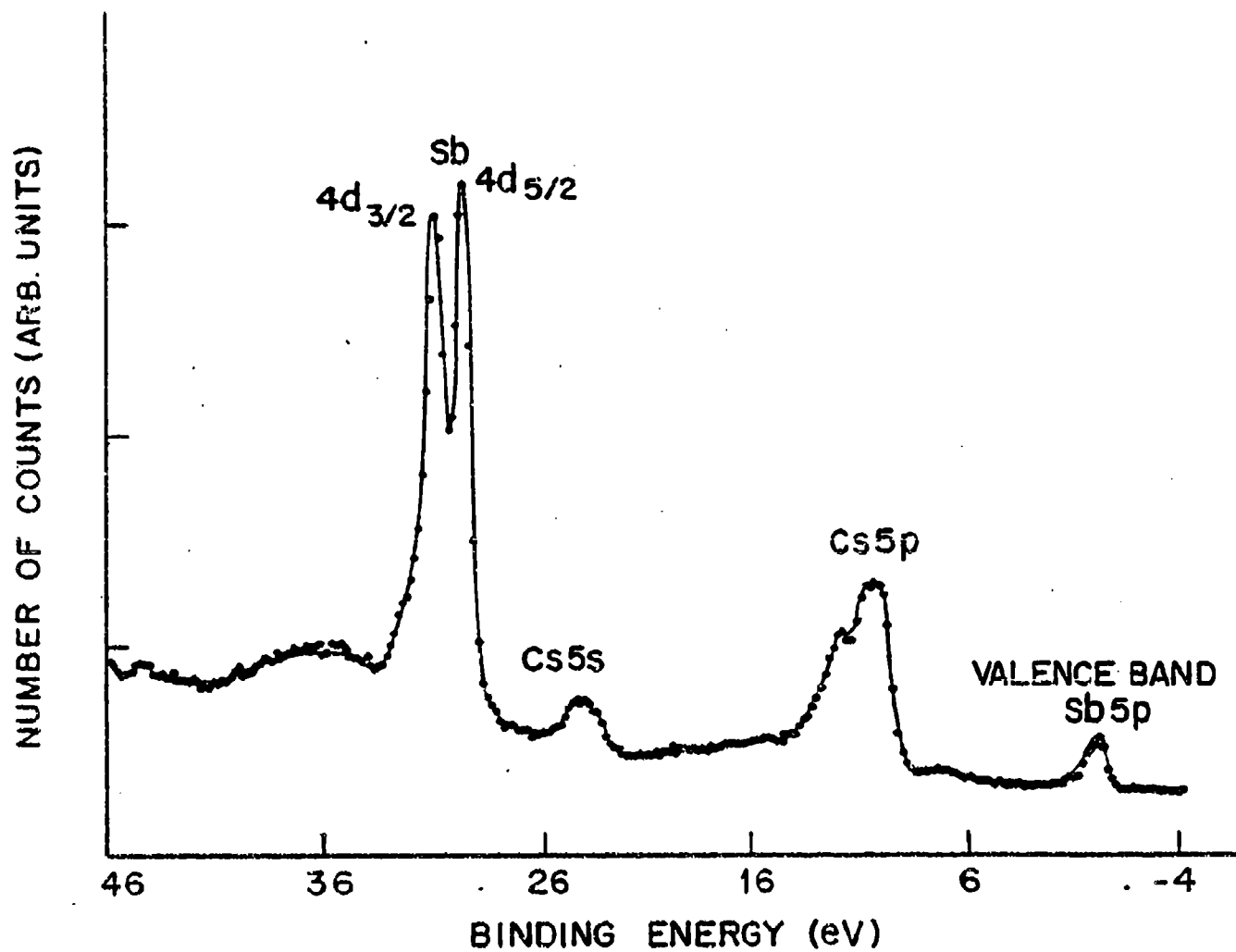


Fig. 3.4 Valence Band and some Core Level Peaks of a good Cesium Antimonide Photoemitter.

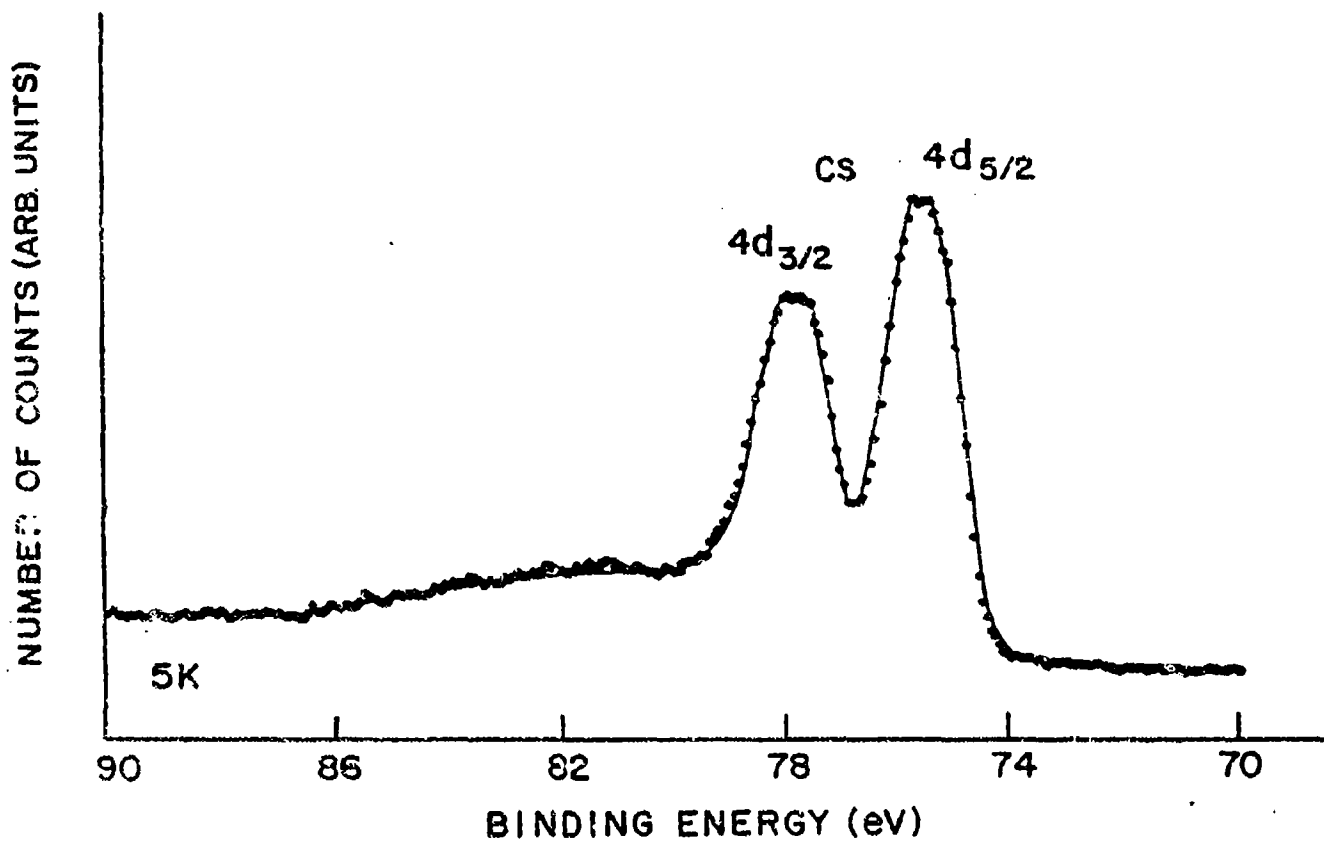


Fig. 3.5 Cs4d Doublet.

at the surface of the photoemitter somewhat tenuous. A band-bending of 0.5 eV, which might produce a large change in the photoemission threshold and the yield, would barely be detectable by our method. We have noted the following however. The shifts of all cesium core levels measured (3d's 4d's, 5s and 5p) were all negative with respect to the free metal binding energy value. The shift was 1 eV for surfaces with photosensitivities in the 100 to 15 $\frac{\mu\text{A}}{\text{cm}^2}$ range (good to fair photoemitters) and 0.75 eV for surfaces with photosensitivities of 3 to 5 $\frac{\mu\text{A}}{\text{cm}^2}$ (poor). As the photosensitivity decreased to very small values (10^{-3} $\frac{\mu\text{A}}{\text{cm}^2}$) both cesium and antimony core levels shifted to their free metal binding energy values, indicative of a separation of cesium and antimony into separate layers with the cesium as the surface layer. Here one can no longer speak of a cesium antimonide photoemitter.

The band-bending region in cesium antimonide photoemitters has been estimated to be $\sim 60 \text{ \AA}$ to 100 \AA in depth.¹⁰ An XPS samples depths of $\sim 20 \text{ \AA}$ it is very difficult using this technique to determine the effects of band-bending. However, one might infer its effect from the 0.25 eV change in binding energy as the photosensitivity varied from 100 to 5 $\frac{\mu\text{A}}{\text{cm}^2}$. But as structural changes are most likely occurring over this range of photosensitivity also, it may not be possible to determine the effects of band-bending alone on photosensitivity without measuring it separately such as with a kelvin probe.

It is of interest that the cesium binding energy is smaller in the compound, relative to the free metal, where because of the charge transfer of a large fraction of an electronic charge to the antimony you would expect a larger one. This is not an isolated incident. For example, the Pb4f binding energy of PbO_2 is lower than that of PbO ¹⁴ despite a more positive charge expected to reside on the Pb^{4+} of PbO_2 compared to that on the Pb^{2+} ion of PbO . Another example are the Na1s binding energies in Na metal, NaI and NaF. The latter two are lower by about 1 and 3 eV, respectively despite the positive charge expected to reside on the Na atom in the two very ionic compounds.¹⁵

In solids with predominantly ionic bonding as exists in good cesium antimonide photoemitters, the polarization energy will be large and since the binding energy will be reduced by a corresponding amount it is quite possible that a smaller binding energy in the solid will occur for an electron in an atom than when the atom is free. This could explain the negative shift of the cesium core levels with respect to the free metal values. We cannot discount the fact that in these experiments we have chosen the Fermi level as our reference energy. As this energy at the surface of a semiconductor can vary considerably the negative shifts could be a reflection of these variations. A better reference for these measurements would be the vacuum level which would require measuring the position of the Fermi level at the surface. These uncertainties concerning core do not affect the results of this work.

Using Scofield's¹⁶ photoionization cross section data we obtain $\frac{\text{Cs}}{\text{Sb}} = 2.8 - 2.9$. This indicates a stoichiometric excess of Sb over cesium from that given by Cs_3Sb . This is consistent with the model of this surface³ in which acceptor levels due to a slight stoichiometric excess of Sb are responsible for the long wavelength threshold occurring at a value slightly below the 1.6 eV bandgap value. This result is shown in Fig. 3.6. where the spectral yield of a typical cesium antimonide photoemitter produced in our experimental arrangement is compared with one from Spicer's work.⁴

It is interesting to note that Cs_3Sb , although having predominantly ionic character, has a low bandgap of 1.6 eV. The energy difference between the Cs6s and the Sb5p (outermost) energy levels is about 3.7 eV. One can explain the observed low bandgap by noting the close proximity of the Cs^+ ions among themselves (nearest neighbor distance - 3.96 Å) which splits and broadens the Cs6s levels, so that the bottom of this (conduction) band is lowered towards the top of the valence (Sb5p) band. To demonstrate the validity of this assertion, we show in Fig. 3.7 a band-structure calculation of the $\Gamma - L$ part of the reciprocal lattice of Cs_3Sb performed by Walter Harrison¹⁷ according to his Bond-Orbital model. Basically, it is a tight-binding calculation taking into account only the Cs6s and Sb5p states, and interactions between nearest neighbors and next-nearest-neighbors only. The energy eigenvalues are obtained from Hartree-Fock (Hermann-Skillman) calculations. In Harrison's model, the interaction matrix elements vary with internuclear distance d as d^{-2} .

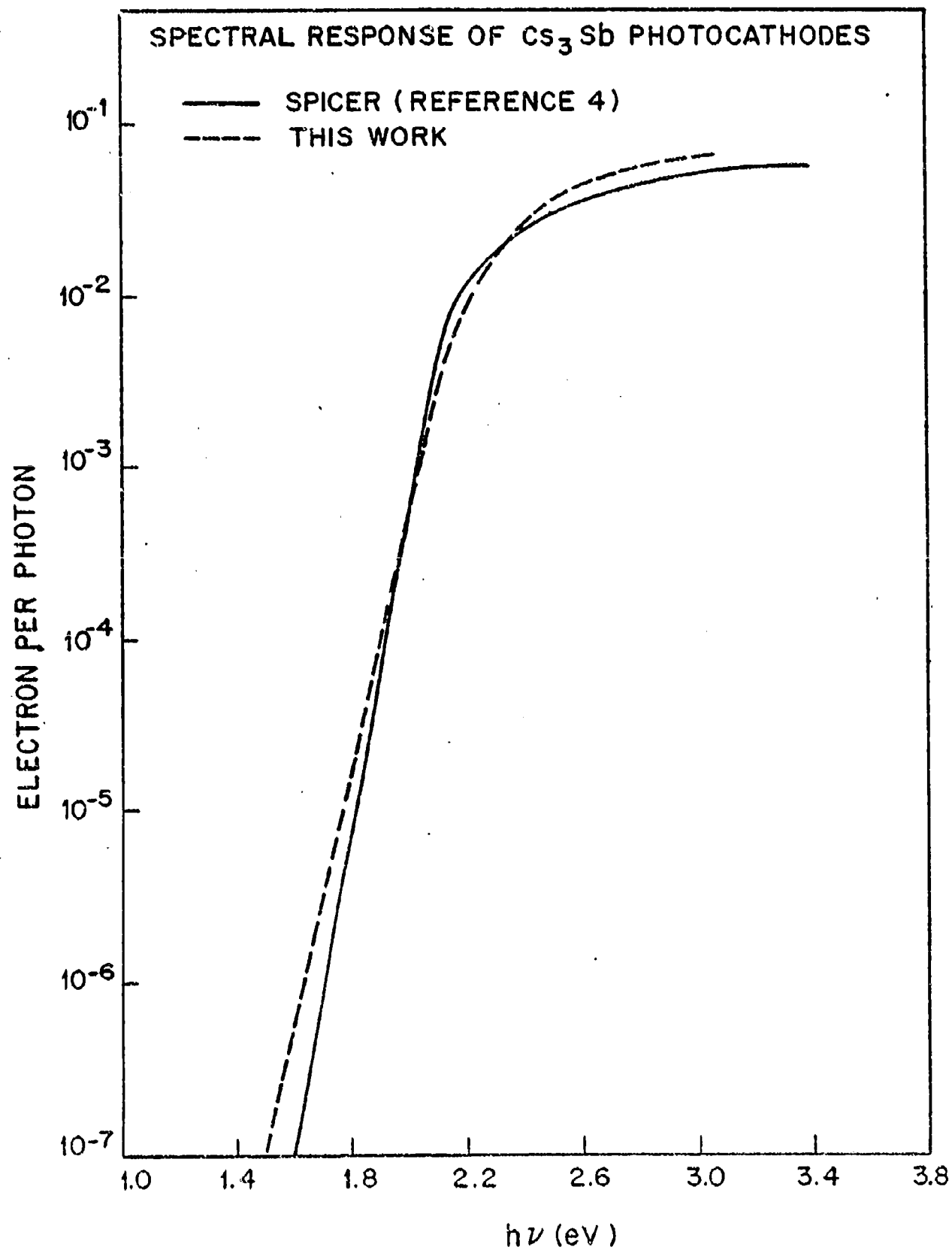


Fig. 3.6 Spectral Yield of Cesium Antimonide Photoemitter.

BOND-ORBITAL CALCULATION OF Cs_3Sb BAND STRUCTURE

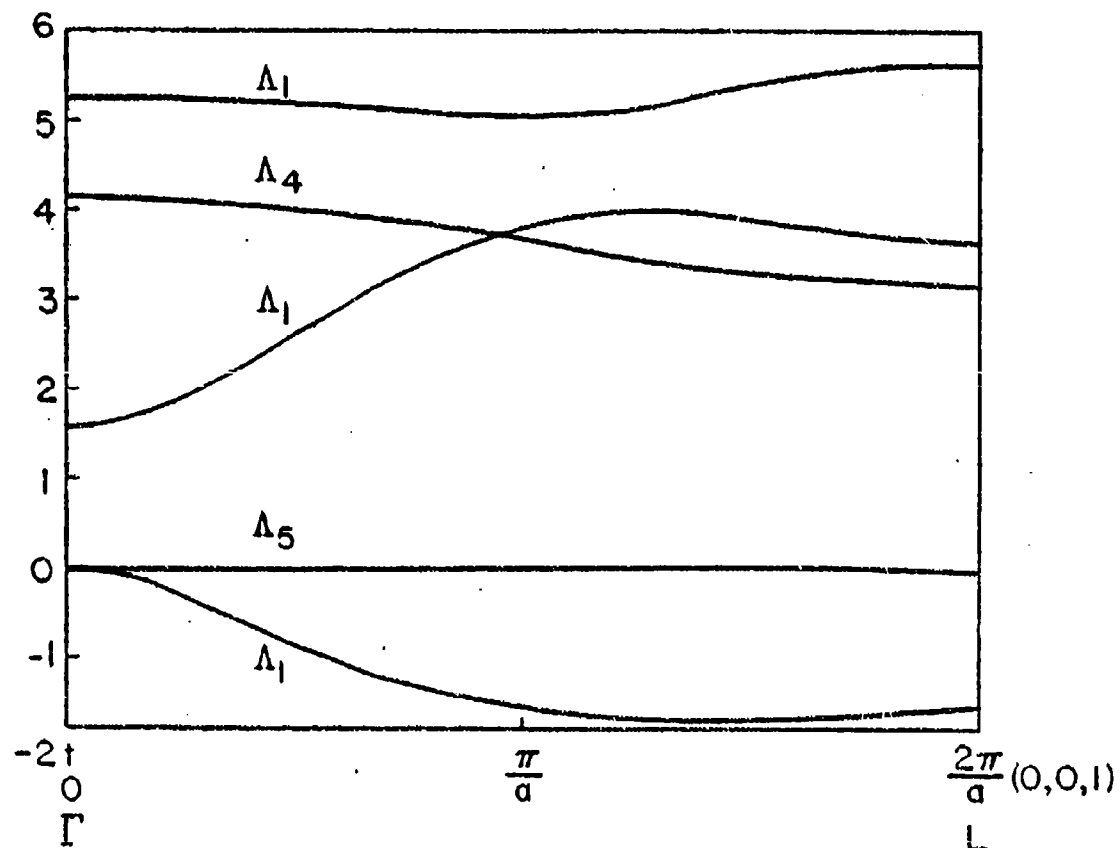


Fig. 3.7 Bond-Orbital Calculation of Cesium Antimonide Band Structure.

However, use of the same proportionality constants that are found to apply for most of the compounds as given by Harrison¹⁸ pushes the bottom of the Cs6s band below the top of the Sb5p level, leading to zero bandgap, i.e., metallic behavior, which is not the case. The s-s matrix elements were thus scaled by a factor of 0.47 in order to give the correct value of the bandgap. This is justified by the fact that Cs compounds do not fit quantitatively very well into the general scheme of the Bond-Orbital model. Figure 8 is only presented to show how the interaction between Cs atoms can decrease the bandgap by such a large extent. The fact that this interaction has to be scaled by a factor of 2 so that the bandgap does not collapse to zero lends further support to the above argument.

This combination of the two characteristics usually not found together (Ionicity and small bandgap) is perhaps what makes Cs₃Sb (and other alkali and multialkali antimonides) a sensitive photoemitting substance. The small bandgap makes it possible to excite electrons in the conduction band with visible light. The ionic character ensures a rapid rise of the optical absorption coefficient at the threshold, resulting in the electrons excited very near the surface (at distances of the order of the escape depth) and also making the effect of nonuniformities in the substance less important.

IV. BOND IONICITY AND ELECTRONIC STRUCTURE OF ALKALI ANTIMONIDE PHOTOCATHODES FROM XPS

4.1 XPS Spectra of Valence Band Region

Typical valence band region spectra for some alkali antimonide photocathodes are shown in Figs. 4.1 to 4.5. Identified structures are labeled. The $\text{Sb}4d_{3/2,5/2}$, $\text{Cs}5p_{1/2,3/2}$, $\text{K}3p$ are clearly core-like with very little broadening apart from spin-orbit doublet splitting (0.5 eV) and instrumental resolution. The $\text{Na}2p$ level just happens to be under the $\text{Sb}4d$ peak. The valence band has been labeled $\text{Sb}5p$ since, it is essentially the atom-like $5p$ levels of Sb , strongly localized on the Sb^{3-} ions.

The valence band is quite flat and very well separated from the $\text{Sb}5s$ level and the less bonded alkali p levels. The $\text{Cs}6s$, $\text{K}4s$ and $\text{Na}3s$ levels should be at a few eV above $\text{Sb}5p$ levels forming the conduction band. The apparently no admixture of alkali ion levels into the valence band formed by the $\text{Sb}5p$ levels would require the transfer of almost one electron, showing the strong ionic character of alkali antimonides.

The possibility of a covalent bond through formation of $(sp)^3$ hybridized orbitals is completely rejected.

For comparison, the XPS valence band region spectrum of a typical ionic solid, CsI , is shown in Fig. 4.6, taken also in our spectrometer. The similarity with alkali antimonide spectra is clear, in particular with respect to Cs_3Sb , due to the iso-electronic structure of I^- and Sb^{3-} ions.

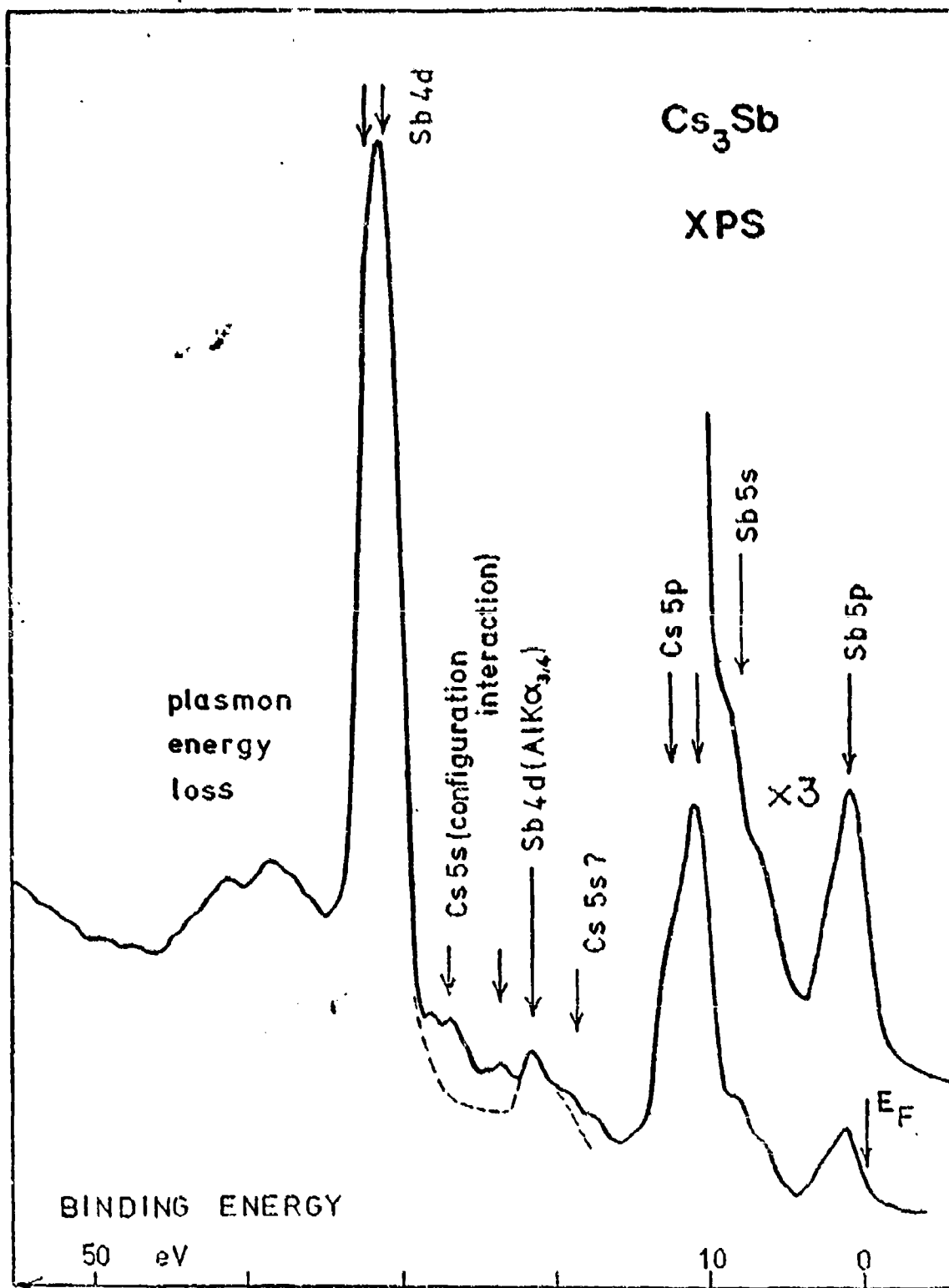


Fig 4.1 XPS of Valence Band region of Cs_3Sb . Fermi level as reference

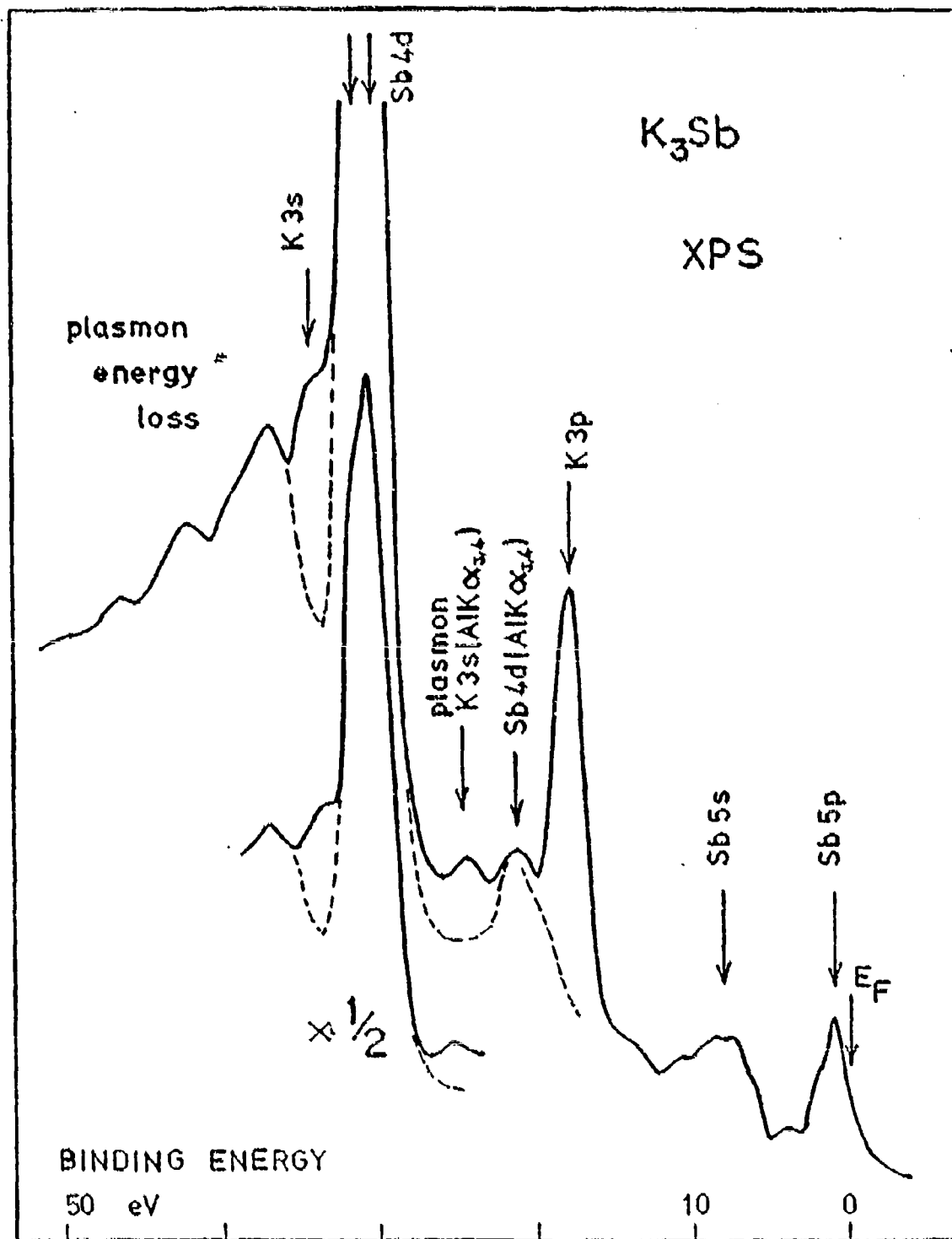


Fig 4.2 XPS of Valence Band region of K_3Sb . Fermi level as reference

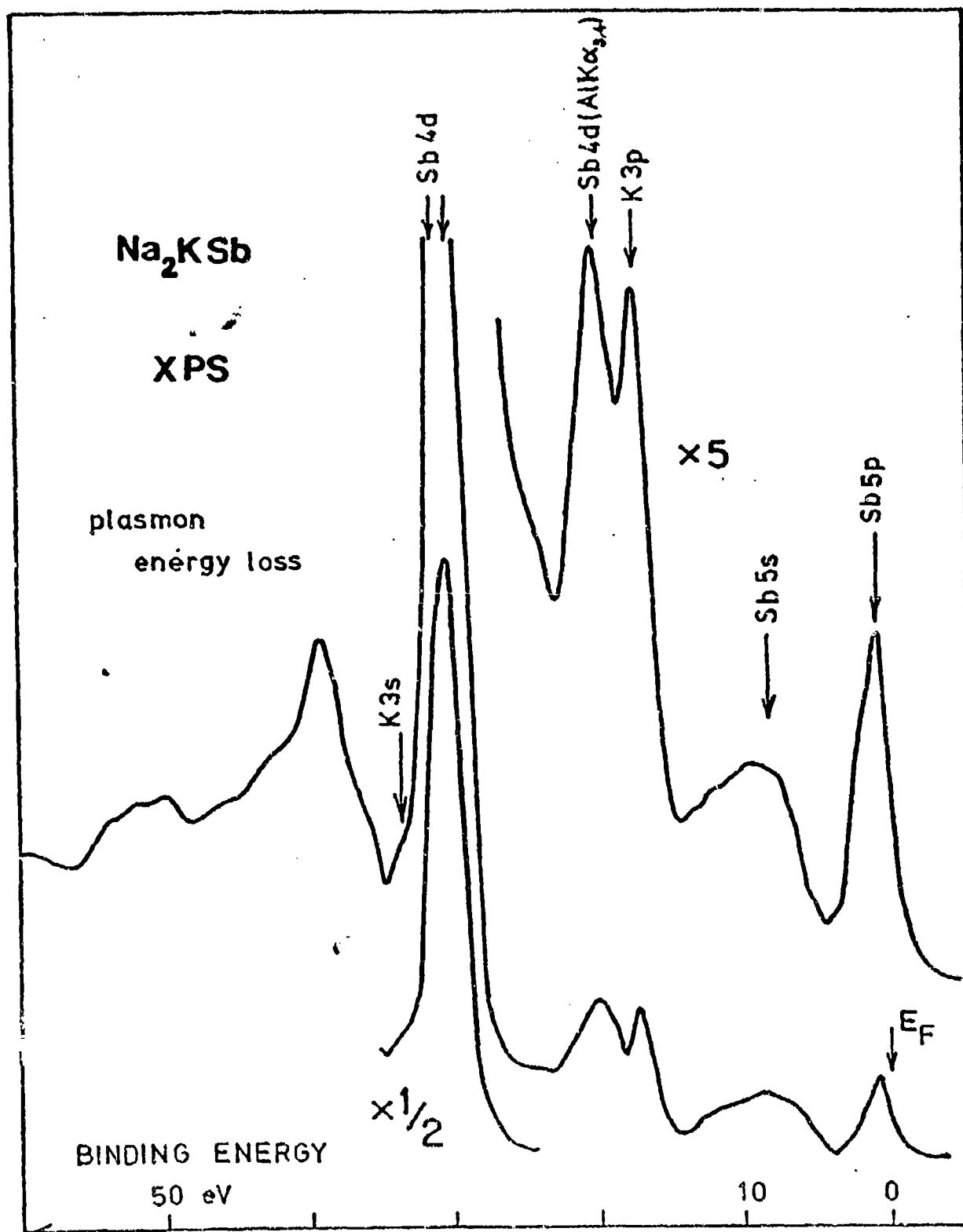


Fig 4.3 XPS of Valence Band region of Na₂KSb. Fermi level as reference

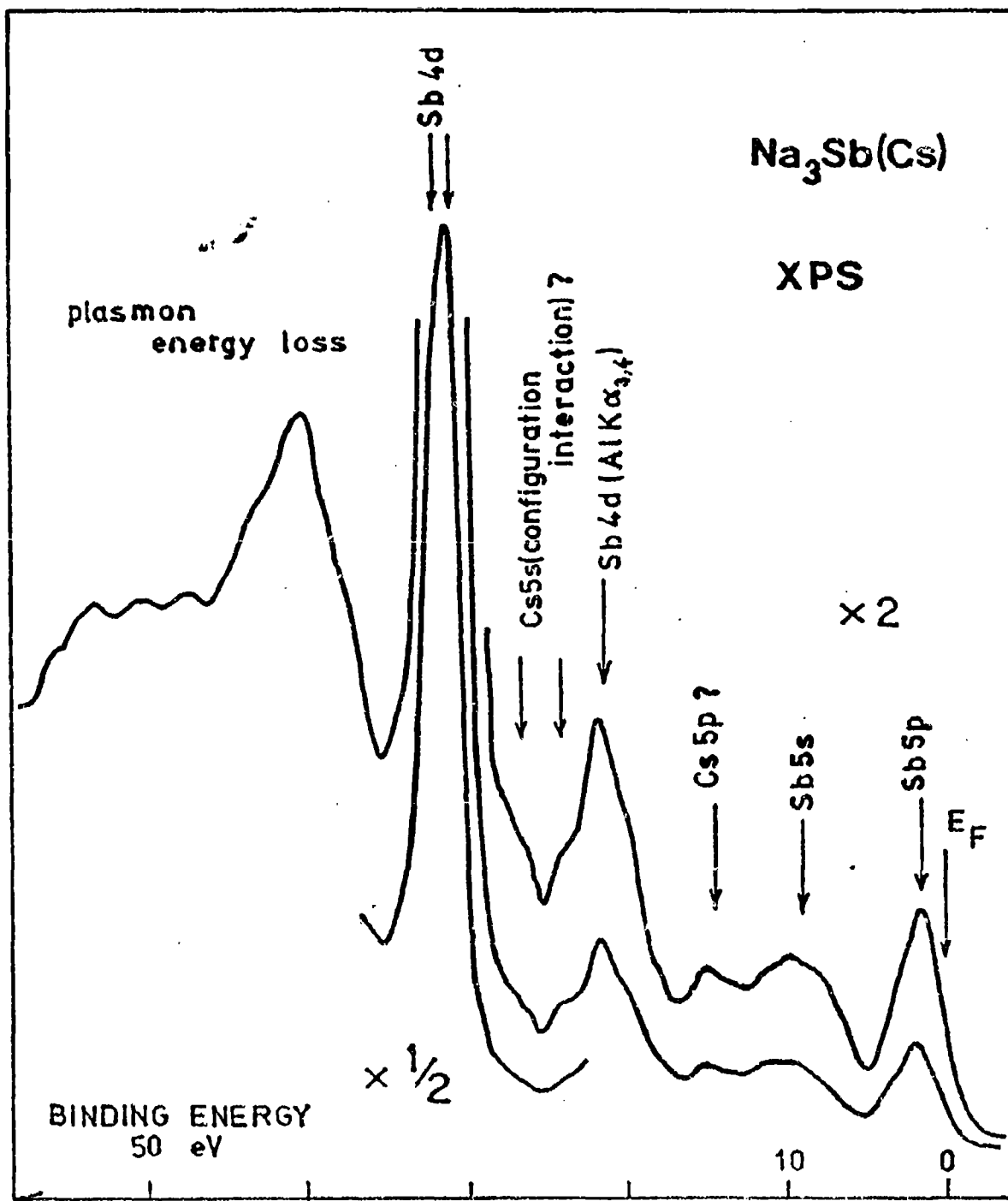


Fig 4.4 XPS of Valence Band region of Na₃Sb(Cs). Fermi level as reference. Probably, Na₃Sb bulk and Na₂CsSb surface layer.

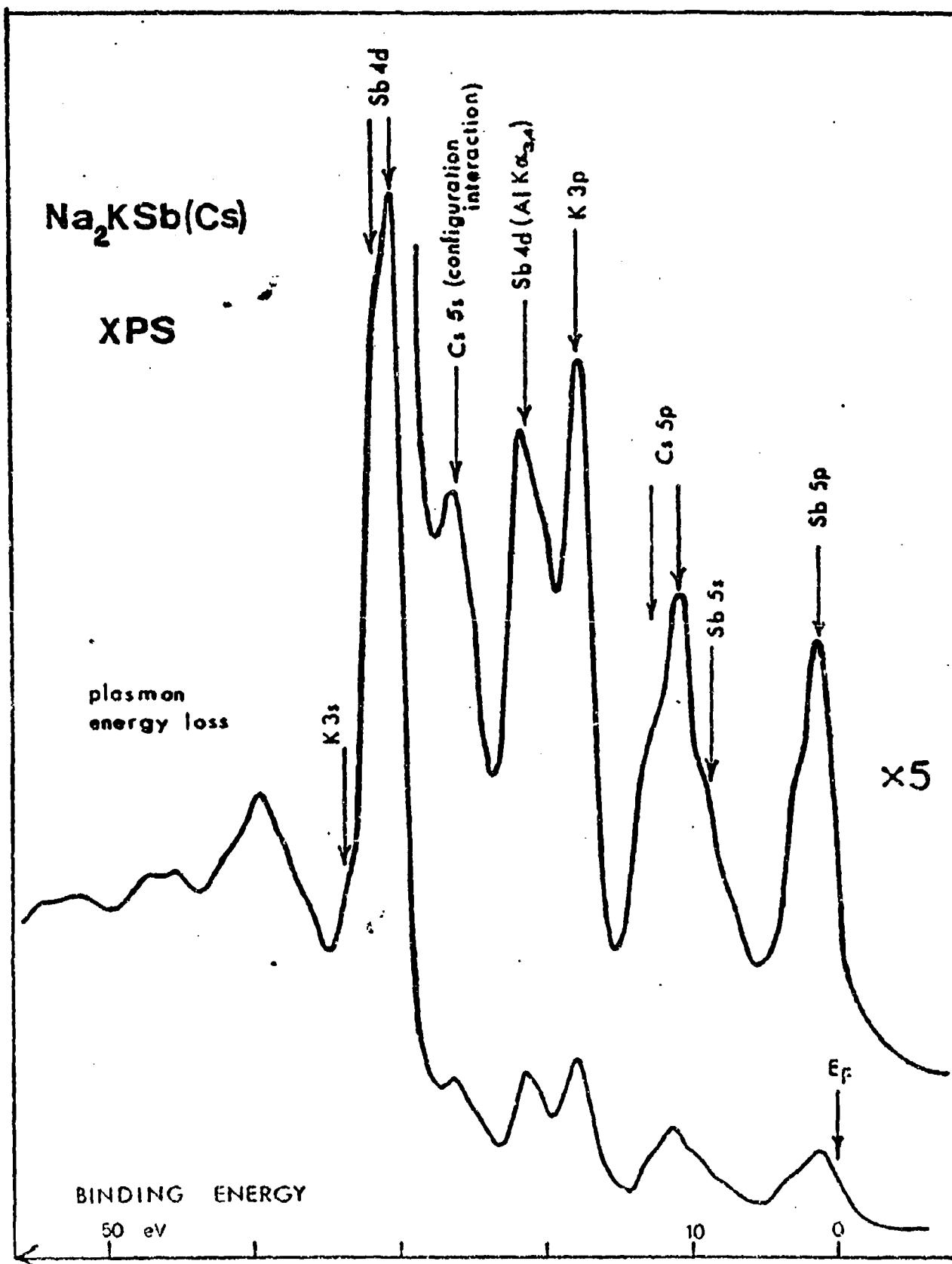


Fig 4.5 XPS of Valence Band region of Na₂KSb(Cs). Fermi level as reference
Probably, Na₂KSb bulk and Na₂CsSb.K₂CsSb surface layer

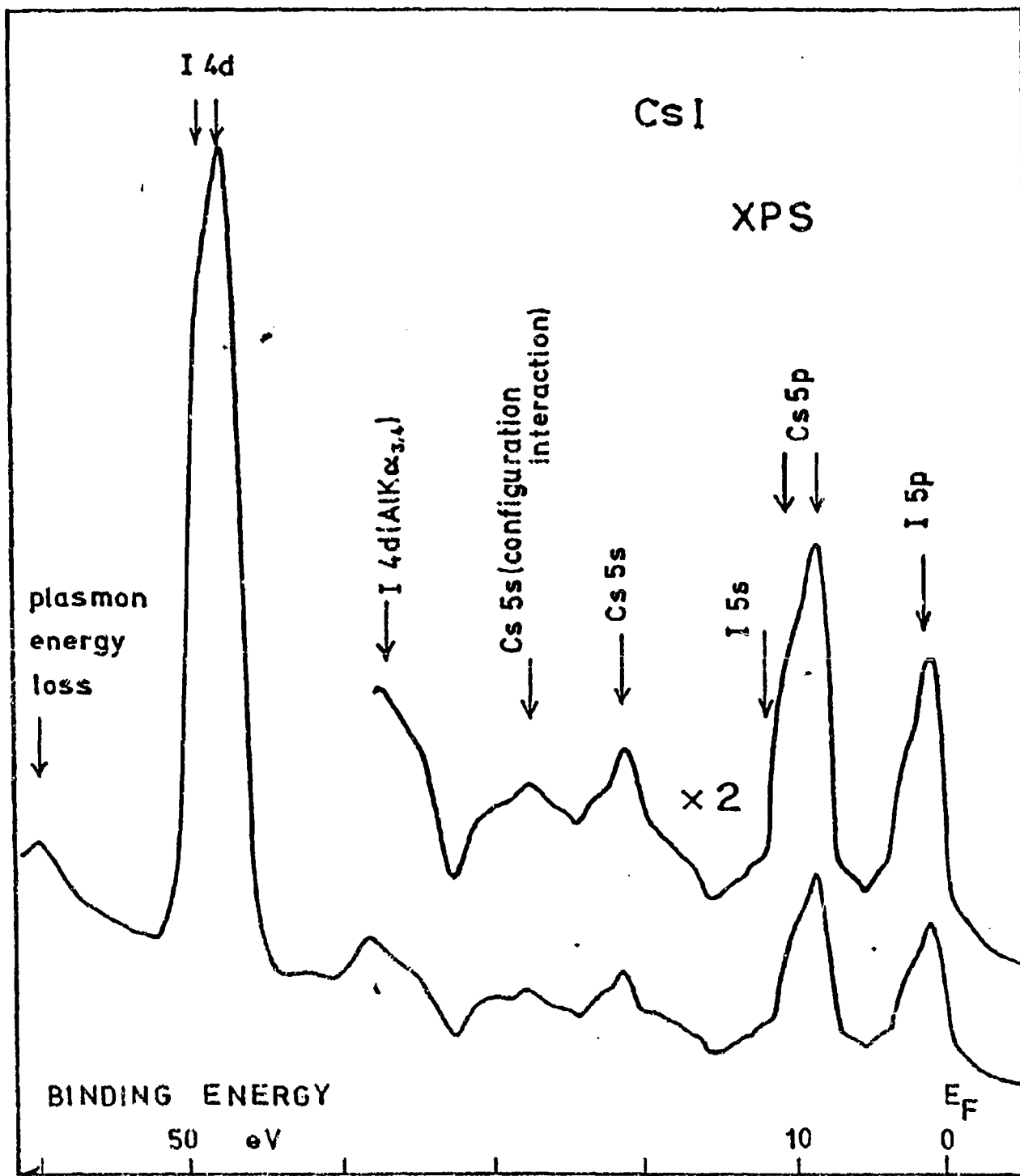


Fig 4.6 XPS of Valence Band region of CsI. Fermi. level as reference

As a comparison the spectrum of Sb, a semimetal, is shown in Fig. 4.7. The broadening of the valence band and interaction with the 5s levels are clear.

For further illustration the valence and conduction band density of states in Cs_3Sb as determined by Spicer¹⁹ and the valence band of Sb metal from XPS by Ichikawa²⁰ are shown together in Fig. 4.8.

4.2 Analysis of Electron Binding Energies from XPS

4.2.1 Sodium in Alkali Antimonides. Comparison with Alkali Halides

Table 4.1 lists experimental Nals absolute binding energies (referenced to the vacuum level) and Auger parameters for alkali halides and antimonide photocathodes, for Na metal, atomic Na, and Na^+ free ion.

Both, from our experimental results and from data in the literature (photoelectron and X-ray data) relative binding energies among orbitals in an atom are constant within experimental error (0.5 eV), independent of atomic, ionic or metal state, in agreement with the point charge electrostatic approximation. These relative binding energies have been used whenever the Nals level (or $\text{K}2p_{3/2}$, $\text{Cs}3d_{5/2}$, $\text{Sb}3d_{5/2}$, below) was not directly given in the literature.

Photocathode Nals binding energies were obtained from our experimental measurements referenced to the valence band peak, plus 1.5 eV for valence band width, plus 3.0 eV for photoemission threshold. A valence band width of 1.5 eV is in agreement with our XPS data and known values for ionic solids. The photoemission threshold given in the literature, 2.0 eV for Na_2KSb and 1.5 eV for $\text{Na}_2\text{KSb}(\text{Cs})$, were measured

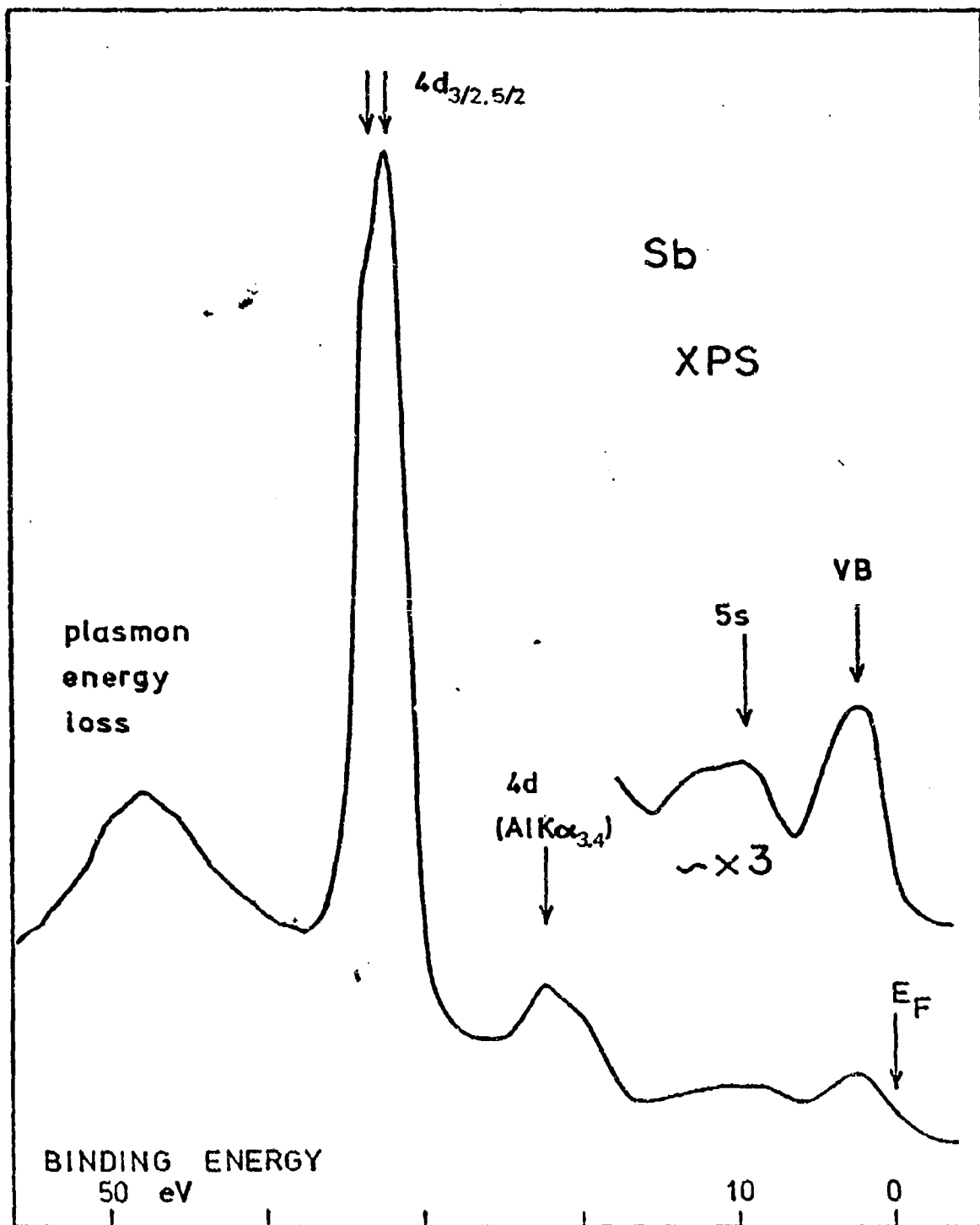


Fig 4.7 XPS of Valence Band region of Sb metal. Fermi level as reference

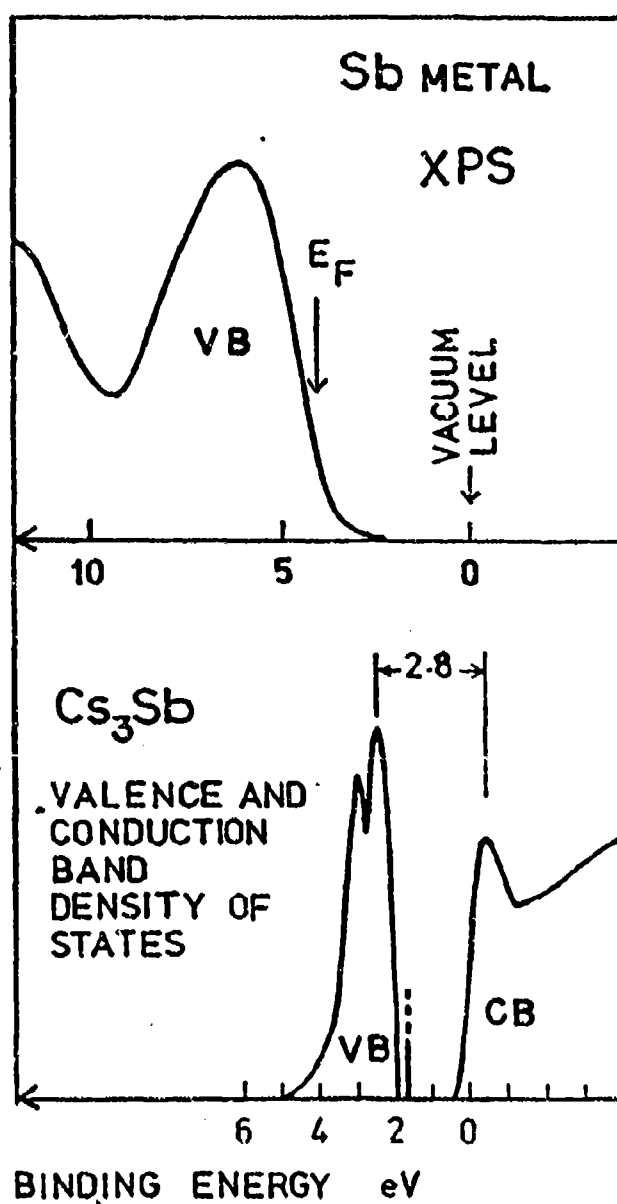


Fig 4.8 Comparison of Valence Band region in rhombohedral Sb²⁰ and Cs₃Sb.¹⁹ Reference: vacuum level. The Average Band Gap between Sb5p (VB) and Cs6s (CB) appears to be ~ 3 . eV in Cs₃Sb.

for photon energies in the UV and Visible range with photoemission escape depths at least one order of magnitude larger than in XPS, and include band bending effects and K_2CsSb -surface layer effects for $Na_2KSb(Cs)$ (see next section).

The Madelung crystal potential for the cubic DO_3 structure is calculated in Appendix D and its value for Na in Na_2KSb is shown in Table 4.1.

Crystal electronic polarization energies $e^2 \frac{1}{2} (1-1/\epsilon)/r$ were computed for a refractive index $n=3.0$ and polarization effective radius $r=0.5 R$. The values of n are known to vary from sample to sample, probably due to errors in thickness measurements, from 2.5 to 3.5. In Mott and Littleton²⁷ treatment of polarization energy the polarization effective radius for cations is about $0.6R$ in alkali halides, and somewhat smaller for Na, so the extreme value $0.5R$ has been used.

Extraatomic relaxation energies calculated from Auger parameter shifts are also shown in Table 4.1. They seem to be a little larger than values predicted by Mott and Littleton theory even for $r=0.5R$.

Table 4.1 lists also calculated binding energies for the sodium halides and alkali antimonide photocathodes predicted by the point charge electrostatic model assuming total ionicity and extraatomic relaxation energies both, measured from Auger parameter shifts, and calculated from crystal electronic polarizability.

TABLE 4.1

Na 1s Binding Energies in Sodium Halides and Alkali Antimonide Photocathodes. Comparison between experimental and calculated values assuming total ionicity. Reference: vacuum level, units: eV.

Material	Experimental E_B	α	Crystal Field $\frac{q}{R}$	Crystal Electronic Polarizability $\frac{1}{4}\Delta\alpha$	$\frac{1}{2}(1-\frac{1}{e})\frac{e^2}{r}$	Calculated E_B for $E_R = \frac{1}{4}\Delta\alpha$, $= e^2 \frac{1}{2}(1-1/e)/r$	E_B
Na free atom	1079.1	569.5					
Na ⁺ free ion	1088.3						
NaF	1075.8	573.2	-10.9	-1.9	-1.9	1075.3	1075.3
NaCl	1077.5	575.3	-8.9	-2.9	-2.5	1076.3	1076.7
NaBr	1076.5	575.7	-8.4	-3.1	-2.6	1076.6	1077.1
NaI	1076.4	576.2	-7.8	-3.4	-2.7	1076.9	1077.6
Na ₂ KSb	1074.8	578.5	-7.6	-4.5	-3.8	1076.2	1076.9
Na ₂ KSb(Cs)	1075.0	578.0	-7.6	-4.3	-3.8	1076.4	1076.9
Na ₃ Sb(Cs)	1074.3	578.2		-4.4			
Na metal	1074.2	579.7		-5.1			

References

- 21, 22 Free ion from Na⁺ 2p. 23 Metal, 24 $\phi = 2.4$ eV. 25
 Free atom. 25, 26, 27 Auger parameter, 11 q^*/R and $e^2 \frac{1}{2}(1-1/e)/r$.
 Alkali halides, 25, 26, 27 Auger parameter, 11 q^*/R and $e^2 \frac{1}{2}(1-1/e)/r$.
 Other this work

For the alkali halides a very good agreement is obtained between experimental and calculated values. This not only proves the validity of the ionic model for alkali halides, but also proves the validity of the approximation $\frac{1}{2}\Delta q = E_R^L$ for the extraatomic relaxation energy.

For the alkali antimonide photocathodes the absolute binding energies are approximately explained. The difference of 1.0 - 1.5 eV has no quantitative meaning, since the absolute binding energies are not exactly known and large errors are probably involved in their somewhat arbitrary estimation. There is no total ionicity and charge transfer is less than 1.0, but it cannot be estimated from absolute binding energies.

In order to avoid systematic errors in absolute binding energies, charge transfer may be calculated from Na1s-Sb3d_{5/2} relative binding energies, that are directly measured from XPS spectra. In this case the Sb3d_{5/2} binding energy for the Sb³⁻ ion is not known experimentally, but it may be extrapolated from known values for atomic Sb and Sb⁺, Sb⁻ free ions, see Section 4.2.4 and Table 4.4.

Thus, for Na₂KSb, from our experimental XPS data and from data in Tables 4.1 and 4.4

$$\text{Na1s, Sb3d}_{5/2} \Delta E_B (\text{free ion} - \text{atom}) = kq = 31 \text{ eV} \quad (q=1)$$

$$\Delta(\Delta q \Phi / R) - \Delta E_R^L = -28. \Delta q - 2.7 \quad (\text{eV})$$

$$\begin{aligned} \text{Na1s, Sb3d}_{5/2} \Delta E_B (\text{Na}_2\text{KSb} - \text{atom}) &= -0.2 \text{ eV} \\ &= 31 \Delta q - 28 \Delta q - 2.7 \quad (\text{eV}) \end{aligned}$$

Therefore, if about the same charge transfer is assumed for K

$$\Delta q = 0.8$$

This value is expected to be just an approximate estimation since this calculation is very sensitive to small errors in the binding energies, Δq is obtained from the difference of two large quantities ~ 10 and the $\text{Sb}^{3-} 3d_{5/2}$ binding energy is not exactly known. But its value is expected to be 512 eV (Table 4.4) or more since the ionic radius increase significantly from Sb^0 to Sb^{3-} . Thus the charge transfer should be at least 0.8.

This charge transfer may be compared with expected ionicity. The Pauling definition of ionicity, based on elemental electronegativities (calculated from empirical heats of formation), yields

$$f_p = 1 - \frac{N}{M} \exp\left(-\frac{1}{4} (X_{\text{Sb}} - X_{\text{Na}})^2\right) = 0.8$$

from $X_{\text{Sb}} = 1.9$, $X_{\text{Na}} = 0.9$, $N=1$, $M=4$, for Na with valence 1 and four Sb nearest neighbor ions. This relatively large ionicity would imply a large charge transfer in good agreement with our estimation.

If a 0.8 charge transfer is assumed, the calculated absolute binding energy is

$$N_{\text{als}} E_B = 1075.9 \text{ eV for } \text{Na}_2\text{KSb}$$

4.2.2 Potassium in Alkali Antimonides. Comparison with Alkali Halides

Table 4.2 summarizes an analysis of $K2p_{3/2}$ binding energy data analogous to the one done for NaI in previous section. In this case only the Auger parameter for KR is well known. The Auger parameter for KCl has been calculated from photoelectron and Auger data from different workers, thus it is subject to larger errors. In order to estimate the unknown value of the Auger parameter for atomic K, it has been calculated to fit experimental data for KF and KCl. Values in Table 4.2 calculated using this estimation are shown in parenthesis.

Photocathode $K2p_{3/2}$ binding energies were obtained from our measurements referenced to the valence band peak, plus 1.5 eV for valence band width, plus 3.0 eV for photoemission threshold, as was discussed in the case of Na, above.

Crystal field energies were calculated from known values of lattice and Madelung constants for K halides, and in Appendix D for the photocathodes. For $Na_2KSb(Cs)$ the Madelung potential was calculated for K_2CsSb .

As in the case of Na, the agreement between experimental and calculated binding energies for the alkali halides is very good.

For the alkali antimonides, the difference between calculated and experimental values seems mostly due to

a) the calculated extraatomic relaxation energies $\frac{1}{2}\Delta\alpha$ are too small compared with values for Na^+ , in spite of Na^+ and K^+ radii are comparable with respect to Sb^{3-} radius, moreover, relaxation energies for Cs^+ are even larger, see section 4.2.3 below. This might be due

TABLE 4.2

K $2p_{3/2}$ Binding Energies in Potassium Halides and Alkali Antimonide Photocathodes. Comparison between experimental and calculated values assuming total ionicity.

Reference: vacuum level; units: eV.

Material	Experimental E_B	α	Crystal Field $\frac{q}{R}$	Crystal Electronic Polarizability $\frac{1}{4}\alpha, \frac{1}{4}(1-\frac{1}{\epsilon})\frac{e^2}{r}$	Calculated E_B for $E_R = \frac{1}{4}\Delta\alpha$, $= e^2 \frac{1}{2}(1-1/\epsilon)/r$
K free atom	300.5	(53.2)			
K ⁺ free ion	308.4				
KF	297.6	56.0	-9.4	(-1.4)	-1.7
KCl	298.5	57.4	-8.0	(-2.1)	-1.9
KBr	298.4		-7.6		-2.1
KI	298.5		-7.1		-2.1
Na ₂ KSb	296.6	60.4	-5.5	(-3.6)	-3.8
Na ₂ KSb(Cs)	296.5	60.6	-6.8	(-3.7)	-3.8
K ₃ Sb	297.1	60.2			
K metal	296.9	(61.2)			
K on stainless steel	296.5	61.3		-4.0	

References

- Free atom, ²² Free ion, ²³ Metal, ^{22,28} $\phi = 2.2$ eV . Alkali halides, ²⁷
 KF Auger parameter, ²⁹ KCl Auger parameter, ^{29,30,26} $\frac{1}{2}(1-1/\epsilon)/r$. ²⁷
 Others this work.

to error in the estimation of atomic K Auger parameter. And

b) the theoretical Madelung crystal potential at the K site in the Na_2KSb structure is very small, about 2 eV smaller than at the Na site, such a difference would be noticeable in XPS of Cs_3Sb , but this is not the case. This will be discussed further below.

Thus, assuming $E_R = 4.5$ eV, and for $\text{Na}_2\text{KSb}(\text{Cs})$ an intermediate value $\Delta q/R = 6.5\Delta q$ eV, the calculated binding energies for $\Delta q = 0.8$ are

$$\begin{aligned} K2P_{3/2}E_B &= 297.2 \text{ eV calculated for } \text{Na}_2\text{KSb} \\ &= 296.9 \text{ eV calculated for } K_2\text{CsSb in } \text{Na}_2\text{KSb}(\text{Cs}) \end{aligned}$$

in relatively good agreement with experimental values in Table 4.2.

Experimental relative binding energies are

$$\begin{aligned} \text{Sb}3d_{5/2}, K2P_{3/2}\Delta E_B &= 233.1 \text{ eV exp. for } \text{Na}_2\text{KSb} \\ &= 233.4 \text{ eV exp. for } \text{Na}_2\text{KSb}(\text{Cs}) \\ &= 232.9 \text{ eV exp. for } K_3\text{Sb} \end{aligned}$$

Using the same assumptions as before, the calculated values are

$$\begin{aligned} \text{Sb}3d_{5/2}, K2P_{3/2}\Delta E &= 234.1 \text{ eV calculated for } \text{Na}_2\text{KSb} \\ &= 232.4 \text{ eV calculated for } \text{Na}_2\text{KSb}(\text{Cs}) \end{aligned}$$

The difference from experimental values, about 1 eV, is comparable with errors involved.

4.2.3 Cesium in Alkali Antimonides. Comparison with Alkali Halides

Table 4.3 summarizes an analysis of $\text{Cs}3d_{5/2}$ binding energy data analogous to the ones done in previous sections. In this case no Auger parameter data is available in the literature. The only available data are from measurements in our laboratory on CsI and Cs vapor deposited on stainless steel. The Auger parameter of atomic Cs has been calculated to fit experimental data for CsI and Cs metal. Values in Table 4.3 calculated using this estimation are shown in parenthesis.

Photocathode $\text{Cs}3d_{5/2}$ binding energies were obtained from our measurements referenced to the valence band peak, plus 1.5 eV for valence band width, plus 3.0 eV for photoemission threshold, as was discussed in the case of Na, above.

Crystal polarization energies $e^2 \frac{1}{2}(1-1/\epsilon)/r$ were calculated for $n=3.0$ and $r=0.6R$, following Mott and Littleton theory.

For the alkali antimonides, the Madelung crystal potential calculated for the two possible sites in the cubic DO_3 structure, Appendix D, means an energy difference of about 2 eV that is not shown in the XPS spectra of Cs_3Sb , where even a difference of 1 eV would be noticeable in the peak width. So, either the charge transfer or the ion position or both are self adjusted to produce the same binding energy. Therefore, an intermediate value for the Madelung potential has been calculated in Table 4.3. In the case of $\text{Na}_2\text{KSb}(\text{Cs})$ the crystal field was calculated for K_2CsSb , the relatively good agreement shown

TABLE 4.3

Cs $3d_{5/2}$ Binding Energies in Cesium Halides and Alkali Antimonide Photocathodes. Comparison between experimental and calculated values assuming total ionicity

Reference: vacuum level; units: eV.

Material	Experimental E_B	α	Crystal Field $\frac{q}{R}$	Crystal Electronic Polarizability $\frac{1}{4}\Delta\alpha$	$\frac{1}{4}(1-\frac{1}{\epsilon})\frac{e}{r}$	Calculated E_B for $E_R = \frac{1}{4}\Delta\alpha$, E_B	$=e^2 \frac{1}{4}(1-1/\epsilon)/r$ E_B
Cs free atom	732.5	(801.4)					
Cs ⁺ free ion	739.5						
CsF	729.7		-8.4		-1.5		729.6
CsCl	730.3		-7.1		-2.2		730.2
CsBr	730.2		-6.8		-2.2		730.5
CsI	730.1	807.4	-6.4	(-3.0)	-2.3		730.8
Na ₂ K Sb(Cs)	729.0	809.3	-6.0	(-4.0)	-3.2	729.5	730.3
Na ₃ Sb	729.1	809.5		(-4.1)			
Cs ₃ Sb	728.5	809.5	-5.5	(-4.1)	-2.7	729.9	731.3
Cs metal	727.9						
Cs on stainless steel	728.5	810.0		(-4.3)			

References 31 Free atom, 25, 27 q/R 32 Metal. 27 Alkali halides; $e^2 \frac{1}{4}(1-1/\epsilon)/r$ and Auger parameter Cs metal C. W. Bates, Jr. (unpublished work). Others, this work

with experimental values supports the theory of Cs in K_2CSb phase for Cs in $Na_2KSb(Cs)$ photocathodes (next section).

For the Cs halides nearly total ionicity explains the observed shifts within experimental error, as in the studies of Na and K halides before.

For the alkali antimonide photocathodes the agreement between calculated and experimental values is relatively good. For a charge transfer of $\Delta q=0.8$, the calculated values are

$$\begin{aligned} Cs3d_{5/2} E_B &= 729.3 \text{ eV calc. for } Na_2KSb(Cs) \\ &= 728.9 \text{ eV calc. for } Cs_3Sb \end{aligned}$$

and the agreement is again very good.

From our experimental measurements, the Cs, Sb relative electron binding energies are

$$\begin{aligned} Cs3d_{5/2}, Sb3d_{5/2} \Delta E_B &= 199.1 \text{ eV exp. for } Na_2KSb(Cs) \\ &= 199.6 \quad Na_3Sb(Cs) \\ &= 198.6 \quad Cs_3Sb \end{aligned}$$

The calculated values, for $\Delta q=0.8$, are (see Table 4.4).

$$\begin{aligned} Cs3d_{5/2}, Sb3d_{5/2} E_B &= 199.9 \text{ eV calc. for } Na_2KSb(Cs) \\ &= 200.7 \quad Cs_3Sb \end{aligned}$$

The larger disagreement for Cs_3Sb could be explained by more ionicity and charge transfer in this case.

4.2.4 Antimony in Alkali Antimonides. Photoemission Threshold Dependence on Lattice Constant and Ionicity

From available 5p binding energy data for free Sb^+ , Sb^0 , and Sb^- , a value for Sb^{3-} free ion may be extrapolated

$\text{Sb}^+ 3d_{5/2} E_B$	$= +7.9 \text{ eV}$	(experimental)
Sb	$= 0$	
Sb^-	$= -7.6$	(experimental)
Sb^{2-}	$= -7.6-7.3$	(extrapolated)
Sb^{3-}	$= -7.6-7.3-7.0$	(extrapolated)

Thus we expect $\text{Sb}^{3-} 3d_{5/2} E_B$ to be at least 512. eV, (see Table 4.4) since the valence shell radius increases significantly from Sb^0 to Sb^{3-} . The atomic radius for Sb is 1.6 Å, the Sb^{3-} ionic radius is 2.5 Å.

From the Sb metal shift and Auger parameter, see Table 4.4 the Auger parameter for the atomic state could be estimated to be 502 eV, but Sb in KSbF_6 has an Auger parameter of 500.7 eV. If intraatomic relaxation energy differences among different ions are neglected, the atomic Sb Auger parameter should be at most 500.5 eV. This estimation is in good agreement with calculated polarization energies for alkali antimonides, Table 4.4. These energies were calculated for $n=3.0$ and $r=0.9R$.

TABLE 4.4

Sb $3d_{5/2}$ Binding Energies in Alkali Antimonide Photoecathodes. Comparison between experimental and calculated values assuming charge transfer $Aq = 0.8$. Reference: vacuum level; units: eV.

Material	Experimental E_B	α	Crystal Field $\frac{q}{R}$	Crystal Electronic Polarizability $\frac{1}{4}A\alpha$	$e^2 \frac{1}{4}(1-e)/r$	Calculated E_B for $E_R = \frac{1}{4}A\alpha$
Sb ⁺ free	541.9					
Sb "	534.0	(500.5)				
Sb ⁻ "	526.4					
Sb ²⁻ "	(519.0)					
Sb ³⁻ "	(512.0)					
Na ₂ KSb	529.7	504.0	20.7q	(-1.8)	-2.1	531.2
Na ₂ KSb(Cs)	529.9	504.2	18.6q	(-1.9)	-1.9	529.4
Na ₃ Sb(Cs)	529.6	504.0		(-1.8)		
K ₃ Sb	529.8	504.1		(-1.8)		
Cs ₃ Sb	529.9	504.9	17.5q	(-2.2)	-1.8	528.2
Sb metal	532.1	505.8				

References

Sb, Sb⁺ free.²³Sb⁻ free.³³Sb metal.²⁹

Others, this work.

Experimental absolute binding energies for the photocathodes were obtained as always from our measurements referenced to the valence band peak, plus 1.5 eV for valence band width, plus 3.0 eV for photoemission threshold. Table 4.4 just shows that the photocathode valence band is the Sb5p levels at 525.3 eV from $\text{Sb}3d_{5/2}$.

Crystal field for Sb in K_2CsSb was calculated in the case of $\text{Na}_2\text{KSb}(\text{Cs})$ photocathode.

Calculated values are very good on the average. They show a trend, large values correlated with small lattice constant through a larger crystal potential. This implies a parallel behavior of the valence band and photoemission threshold. Using $\text{Sb}3d_{5/2}, 5p \Delta E_B = 525.3 \text{ eV}$ and a valence band width of 1.5 eV, the calculated values for the photoemission threshold are

$$\begin{aligned} E_T &= 4.4 \text{ eV} \quad \text{for } \text{Na}_2\text{KSb} \\ &= 2.6 \quad \quad \quad \text{K}_2\text{CsSb} \\ &= 1.4 \quad \quad \quad \text{Cs}_3\text{Sb} \end{aligned}$$

This shows that large lattice constants contribute to produce small photoemission thresholds, but the differences are too large compared with experimental values. This contribution may be partially compensated by more charge transfer (electropositivity increases with radius in the alkali metals) since Madelung potential is proportional to charge transfer, but chemical shift $k\Delta q \approx \Delta q/r_v$ is not exactly so, because r_v increases with Δq . Both contribution are clearly shown in Table 4.5.

TABLE 4.5

Experimental evidence of Photoemission Threshold correlation with Lattice Constant and Valence Charge Transfer in Alkali Antimonides. Photoemission Threshold E_T in eV and Nearest Neighbor Distance R in Å

LATTICE CONSTANT , (IONICITY)				
→				
Na ₃ Sb	Na ₂ KSb	Na ₂ RbSb	Na ₂ CsSb	
3.5	2.0	1.8	1.5	
3.10	3.34	---	---	
K ₂ NaSb	K ₃ Sb	K ₂ RbSb	K ₂ CsSb	
---	2.8 (H) 2.5 (C)	2.0	2.0	
3.24	3.57 3.68	---	3.72	
		Rb ₃ Sb	Rb ₂ CsSb	
		2.2	1.7	
		3.81	---	
			Cs ₃ Sb	
			2.0	
			3.96	
				↓ (LATTICE CONSTANT), IONICITY

(LATTICE CONSTANT), IONICITY

H, hexagonal phase ; C, cubic phase. For references see Table 1.1

Thus the ionic model for the alkali antimonides not only can explain a photoemission threshold of about 2-3 eV, but also its dependence on lattice constant and ionicity, by reasonable values of the charge transfer and valence shell radius of Sb^{3-} ion.

4.3 Valence Band Localization from XPS Relaxation Energies

4.3.1 Valence Band Electronic Polarizability

Both, calculated values from Mott and Littleton theory and experimental values from Auger parameter shifts, show that in ionic solids the crystal electronic polarizability is much larger at the cation sites than at the anion sites. This difference is even larger in the experimental values. The dependence of electronic polarization potential on lattice site is due to the valence electron localization on the anions, since electronic polarization is mostly due to relaxation of the loosely bound valence electrons. Thus experimental determination of extraatomic relaxation energies from Auger parameter data becomes a probe for valence band localization and ionicity.

In the classical treatment of electronic polarizability by Mott and Littleton induced point dipoles are assumed at the cation and anion lattice sites, using electronic polarizabilities of ions. These ion electronic polarizabilities M_i are obtained from correlation of optical data of different ionic compounds by means of the Drude relation, that for optical frequencies reduces to

$$n^2 = \epsilon = 1 + 4\pi \sum N_i M_i$$

where N_i are atomic densities. Relevant ion electronic polarizabilities are shown in Table 4.6. This table shows the large difference between anions and cations, suggesting the strong contribution of the valence electrons. This contribution is probably underestimated by the highly indirect measurement method compared with photoemission relaxation energies that probe directly the cation and anion sites.

In the photoemission process electronic relaxation towards the core hole occurs through core hole - valence electron interaction as has been studied for the case of metals by Lundqvist.³⁴ The coupling of core holes to the density fluctuations of valence band electrons (plasmons) is in the long wavelength limit completely equivalent to the coupling with a free electron gas, because the plasmon frequency $\hbar\omega_p$ is higher than the valence electron binding energy. This relaxation process may be seen as a "crystal shake-up". At the high excitation energies of XPS photoemission occurs in the sudden approximation, the crystal is left in an excited state formed by a core hole in an ion plus several plasmons in the valence band that would decay producing the relaxation of valence electrons towards the hole. The result in the spectrum is a narrow strong peak, the one-electron peak, at an energy corresponding to the complete relaxation around the hole, plus a broad intrinsic plasmon resonance structure at higher binding energies. The relative weight of this shake-up structure is such that the average energy of the total spectrum (including the one-electron peak) coincides with the Hartree-Fock orbital energy. This same rule shows the relation between the relaxation energy and the satellite structure, when one is large the other must be correspondingly large.

TABLE 4.6

Electronic Polarizabilities of Ions in \AA^{-3} .

		F^-	Ne	Na^+	Mg^{2+}	Al^{3+}	Si^{4+}
		1.0	0.4	0.18	0.09	0.05	0.017
		0.7	---	0.14	---	---	---
		Cl^-	Ar	K^+	Ca^{2+}		
		3.7	1.6	0.8	0.5		
		3.0	---	1.3	1.1		
Sb^{3-}	Te^{2-}	I^-	Xe	Cs^+	Ba^{2+}		
32.	14.	7.1	4.0	2.4	1.55		
---	9.	6.4	---	3.3	2.5		

4.3.2 Comparison of Alkali Halides and Antimonides

Localization of valence band electrons on the anions in strongly ionic crystals is reflected in very different extraatomic relaxation energies for anions and cations. Because the valence shell radius, approximated by the anion radius, is large, the cation polarization radius, defined by the equivalent polarization in a continuous medium

$$E_R = e^2 \frac{1}{2} (1 - 1/\epsilon) / r ,$$

should be smaller than the nearest neighbor distance R . However, for an anion the nearest anions are at the next nearest neighbor distance, taking in account the anion radius, this should give a polarization radius about R .

For Na in the alkali halides experimental data are available. In Table 4.7 experimental polarization effective radii, calculated from Auger parameter shifts, are compared with calculated values from Mott and Littleton theory. The difference can be explained by the reduction of the valence shell to a point dipole in Mott and Littleton theory.

For the alkali antimonides, using the average value $n=3.0$, the polarization effective radius for Na^+ and Cs^+ is $0.4 R$ in good agreement with experimental values for the alkali halides.

TABLE 4.7

Polarization Effective Radius for Na^+ in the Alkali Halides from Mott and Littleton theory and from Auger Parameter shifts. The optical Dielectric Constant and the Nearest Neighbor Distance are also shown

Material	ϵ	R (Å)	Polarization Effective Radius from	
			M&L Theory r/R	Auger Parameter r/R
NaF	1.74	2.31	0.70	0.70
NaCl	2.25	2.81	0.57	0.49
NaBr	2.62	2.97	0.62	0.52
NaI	2.91	3.23	0.54	0.43

ϵ and R from ;³⁵

others, see Table 4.1

In the alkali antimonides the ratio of the anion to cation polarization radii is about 1.8-2.5, while for the alkali iodides these ratio, from Mott and Littleton theory, varies from 1.11 for CsI to 1.83 for NaI. The agreement is good if we consider that in Mott and Littleton theory the cation polarization radii are about 17% larger than experimental ones.

From values in Table 4.4, the polarization effective radius of Sb^{3-} in alkali antimonides can roughly be estimated in about R.

4.4 Band Bending and other Surface Effects

It is known that XPS core level peaks of alkali halides are structureless and very narrow, with an intrinsic width smaller than 1 eV.³⁰

Any important structure with an energy separation of 0.5 eV could be detected. Our experimental XPS data for alkali antimonides also show such lack of broadening and structure as far as our instrumental resolution allows.

That should be explained since there are many effects that could modify binding energies at the surface.

a) Madelung crystal potential at the surface can be as small as 80% of the bulk,³⁶ this may be 1 - 2 eV less.

b) Also electronic relaxation energies should be smaller at the surface; for materials with very large relaxation energies as CsI and alkali antimonides, this should give a noticeable contribution.

c) For cubic alkali antimonides even the bulk Madelung potential can be different in 2 eV for the alkali A and A' in $A_2A'Sb$, see Appendix 1.

d) An extreme case is that of K in $Na_2KSb(Cs)$ photocathodes. In these photocathodes several phases are present, at least Na_2KSb , K_2NaSb and K_2CsSb , see chapter 6. But binding energies are the same in all cases.

e) It is well known that strong band bending may occur at the surface of alkali antimonides.^{3,37} But the depth of this phenomenon can be as large as 200 Å, and contribution to XPS with escape depths of the order of 20 Å, might be smaller than 0.5 eV, and not detectable.

f) Since ion coordination is different at the surface, charge transfer can also be different.

g) Our XPS data seem to show an excess of alkali at the surface, see chapter 6. Also AES studies ³⁸ suggest that an alkali excess might be in equilibrium at the surface of alkali antimonides that are alkali deficient at the bulk. This is related with e) above.

A satisfactory explanation cannot be given to this problem. But it is reasonable to think that all these effects will adjust themselves to produce the same binding energies with respect the Fermi level, or at most varying slowly at the surface as is believed for the band bending effect. Otherwise there will appear gradients in the electrochemical potential, creating a driving force for electron or ion diffusion.

The very low Madelung potential at the A' cation site in cubic $A_2A'Sb$, is due to the eight nearest neighbors, all A cations. That such a difference between the A, A' sites is not present in actual alkali antimonides may be explained by:

i) Alkali vacancies and Sb interstitials might partially compensate this difference in Madelung potential. Such defects are believed to explain surface band bending

ii) Cations may be displaced from theoretical sites in the cubic DO_3 structure in order to compensate the difference of Madelung potential. In section 5.3. below, it will be shown that such phenomenon is the driving force to form the hexagonal phase of some alkali antimonides. In cubic alkali antimonides the distortion of the perfect DO_3

structure may be so small and random that most of the DO_3 symmetry and lattice parameters are maintained.

Experimental support for this is given by some unexplained features in the X-ray diffraction and electron diffraction studies of cubic alkali antimonides,^{39,40} To explain these features, these workers found necessary Debye temperature factors as large as 6.5 \AA^2 for Sb and 14.5 \AA^2 for Cs. They found also superlattice reflections that they could not explain by the DO_3 structure or any other unit cell. Downman et al.,⁴⁰ suggested that Na and K atoms are displaced from their theoretical positions in Na_2KSb breaking the threefold symmetry of the four (111) axis. This is just what happen in going from cubic DO_3 to hexagonal Na_3Sb structures, see section 5.3 .

4.5 Electronic Structure of Alkali Antimonides

From considerations in section 4.4, above, it appears that, due to the ionic character and crystal structure of alkali antimonides, cation diffusion is very large, producing an equilibrium situation where the bulk is alkali deficient and the surface has an excess of alkali. This is extreme in cubic $A_2A'Sb$ where the A' cation is comparable in radius with the A cation, see section 5.3, as in Na_2KSb and Cs_3Sb , producing a p-type bulk and n-type surface, and strong band bending. This explains the low photoemission threshold of these photocathodes. This also explains why the cubic K_2CsSb is not so strongly p-type,⁴¹ it is nearly intrinsic.

In sections 4.2 , above, it has been shown that the ionic model for alkali antimonides explains XPS relative binding energies to within errors involved. But it was found a systematic difference of about 1 eV between the top of the valence band, calculated from the ionic model, and experimental values for the photoemission threshold. This can be explained by surface band bending, since the escape depth for photoemission threshold measurements is one order of magnitude larger than the XPS probe depth.

In Fig 4.9, experimental binding energies for free ions together with our XPS measurements of relaxation and relative binding energies, and calculation of Madelung energies, are combined with data from UPS to explain the electronic structure of Cs_3Sb . Total ionicity has been assumed in Fig 4.9, but any difference from this extreme value of the charge transfer, will nearly compensate its effect through a proportional change in Madelung potential. Solid state effects broadening valence and conduction bands to about 1 eV, have been included for the solid.

For the free ion $\text{Sb}^{3-}5p$ level two values are shown. One calculated from experimental data for free Cs^+ and Cs_3Sb solid, and the other extrapolated from data for free Sb^- , Sb^0 , and Sb^+ . The large Sb^{3-} radius can explain that this extrapolated value should be larger, see section 4.2.4 .

In Fig 4.10 the electronic structure of CsI is explained in a similar way. It can be seen that again the photoemission threshold calculated from XPS data, ~ 8 eV, is about 1 eV larger than experimental

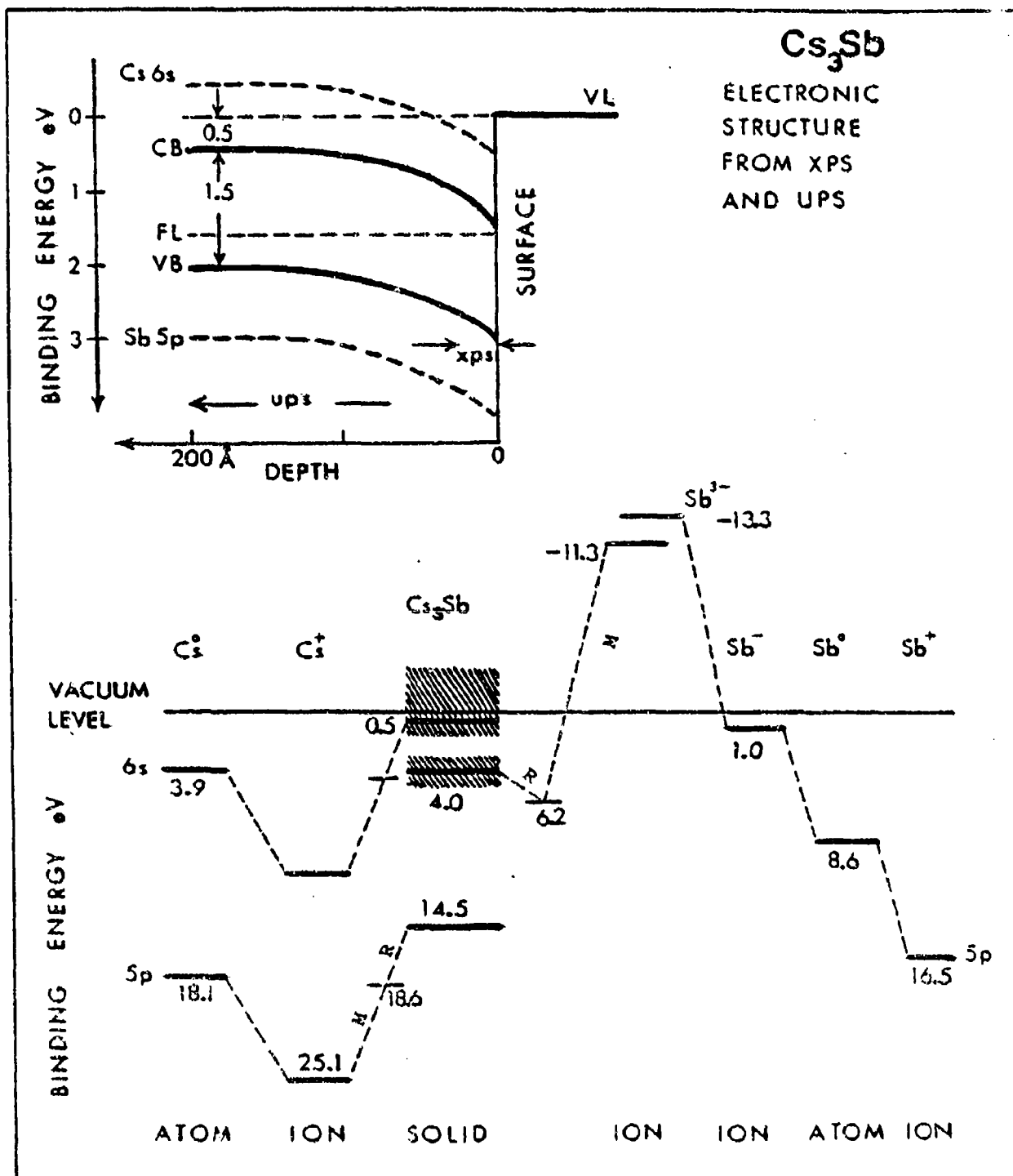


Fig 4.9 Electronic structure of Cs₃Sb from XPS and UPS data.

M, Madelung energy. R, electronic relaxation energy. For references see sections 4.2.3 and 4.2.4 and Tables 4.3 and 4.4 . For UPS see Fig 4.8 .

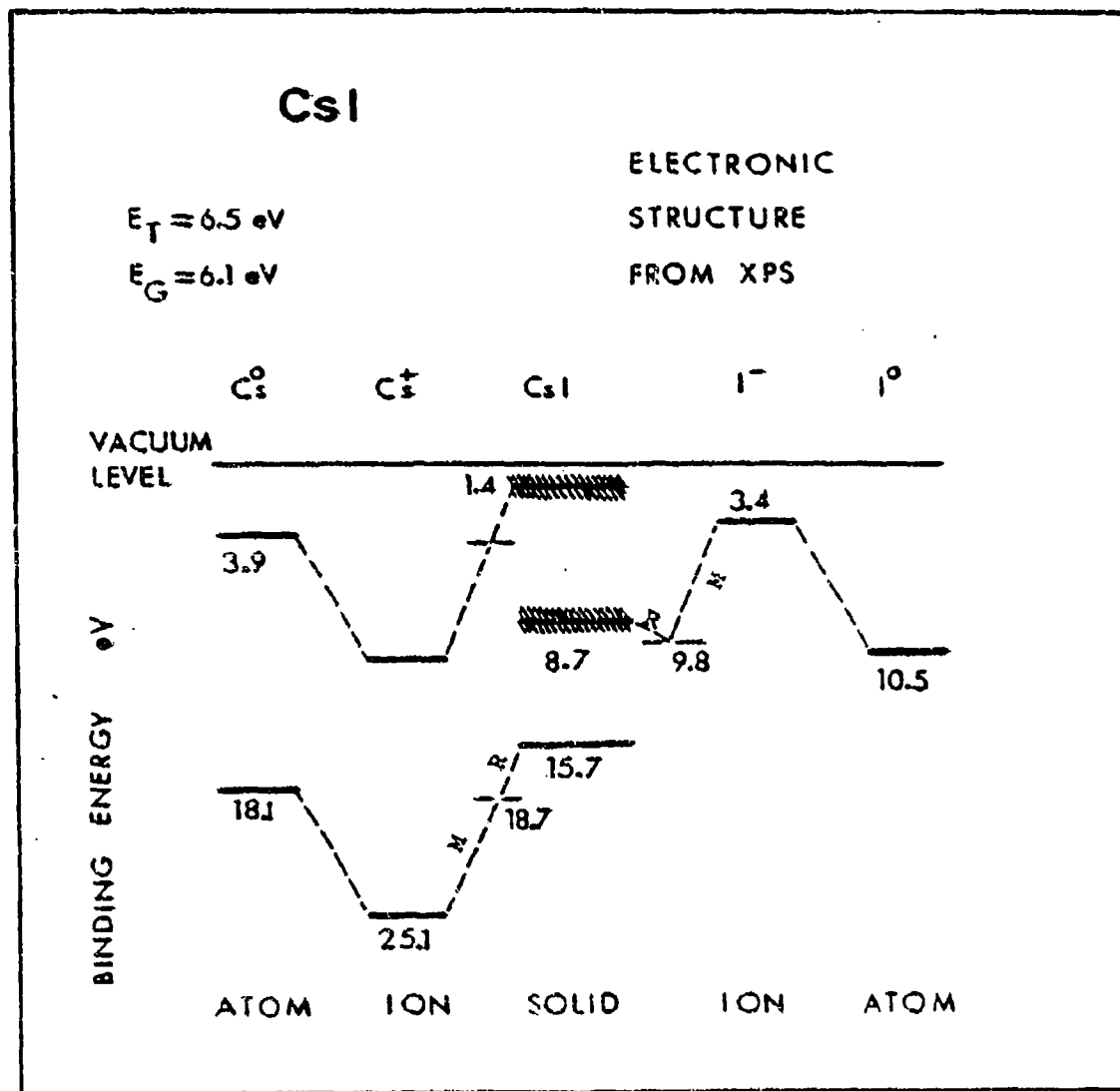


Fig 4.10 Electronic structure of CsI from XPS data.

M, Madelung energy. R, electronic relaxation energy. For references see section 4.2.3 and Table 4.3. E_T and E_G from ⁴⁷.

values from UPS. This might indicate surface band bending effects also in alkali halides.

In this chapter and in the next one, alkali halides and antimonides are shown with many similar properties due to their common ionic crystal binding. However, as photocathodes, they are very different. Comparing Fig 4.9 and 4.10, it is clearly seen that the difference in photoemission threshold is due to the Sb^{3-} ion. Alkali antimonides have very small photoemission threshold due to the small electron binding energies of the Sb^{3-} ion, and to the large electronic relaxation energies, both due to the valence electrons of the Sb^{3-} ion.

V. OTHER EXPERIMENTAL EVIDENCE OF IONICITY IN THE ALKALI
ANTIMONIDES

5.1 Photoelectric Emission

The similarities between the energy distribution of photoelectric emission for excitation in the visible and UV range, in alkali halides and alkali antimonides, as well as the differences between them and covalent solids, are well known since the works of Spicer,⁴ Taft and Philipp,⁴² Philipp et al.,⁴³ Krolikowski,⁴⁴ DiStefano,⁴⁵ DiStefano and Spicer,⁴⁶ See reviews by Spicer in.^{47,48}

For alkali halides and antimonides no structure is found due to direct transitions between singular points (Van Hove) in the valence and conduction bands as it is typical of covalent crystals. Rather the structure in the EDC's is due to the electronic structure of the valence band. This valence band structure was found to correlate very well with the free halide or antimony ion spin-orbit splitting, see Fig 4.8, showing the atomic, localized character of the valence band. Spicer⁴ pointed out localization of the hole created in the photoemission process as an explanation for these characteristics of the EDC's.

In the alkali halides and antimonides the electric dipole transition between the atom-like valence band, formed by the last p orbitals of the halide or antimony, and the conduction band formed by the last s levels of the alkali, is allowed and strong.

In covalent solids the valence and conduction bands are the bonding and antibonding (sp) hybridized orbitals, the electric dipole transition is weak except in some singular points in the Brillouin zone (Van Hove singularities) due to Bragg reflection or crystal symmetry, where the mixing is strong and the energy bands are flat.

Occurrence only of non direct transitions is further discussed in next section.

5.2 Hole Mobility

As it could be expected, in the alkali halides and antimonides and other strongly ionic solids with narrow valence bands strongly localized on the anions, the hole mobility is very small, less than $10 \text{ cm}^2/\text{V-s}$,⁴⁷ compared with covalent solids where the hole mobility is always larger than $100 \text{ cm}^2/\text{V-s}$; for example, for InSb it is $750 \text{ cm}^2/\text{V-s}$ (60,pE-100).

Spicer⁴⁷ pointed out the correlation between very small hole mobility, less than $10 \text{ cm}^2/\text{V-s}$, and the occurrence only of non direct transitions in the photoemission process, i.e., no \underline{k} momentum conservation.

Hole localization or small hole mobility and occurrence only of non direct transitions are consequences of a crystal valence band formed by the non interacting atom-like valence bands of the anions. The strong localization on the anion produces an indetermination in the momentum \underline{k} , through the Heisenberg principle

$$\Delta \underline{k} \cdot \Delta x \geq 1$$

For a localization of the valence band of about $4a_0$, as in the alkali antimonides, using the anion radius, the indetermination in k becomes $\Delta k > 4/a_0$, of the order of the Brillouin zone.

In covalent solids a crystal valence band is formed by mixing of the last s and p orbitals of both component atoms through a strong nearest neighbor interaction, producing a wide energy band where electrons have a free-like dispersion relation, modulated by the crystal symmetry, with a definite k momentum due to very strong delocalization.

5.3 Crystal Structure

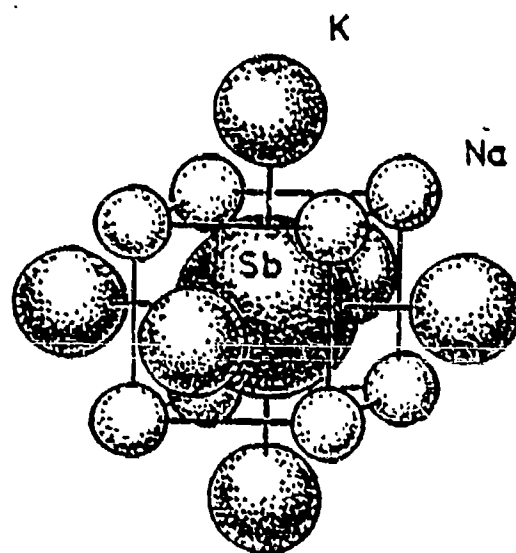
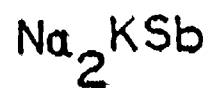
Crystal structures of alkali antimonides, Fig 1.1 and 1.2, have high coordination numbers and large nearest neighbor distances typical of ionic solids. Nearest neighbor distance varies from $R = 3.96 \text{ \AA}$ for Cs_3Sb to $R = 3.10 \text{ \AA}$ for Na_3Sb , that are just a little smaller than calculated from ionic radii 0.95 , 1.69 , 2.45 \AA for Na, Cs, Sb, respectively.

Actually the high coordination numbers required in the ionic structure of $A_2A'Sb$, where A and A' are two different or equal alkalis, are not achieved through an unique nearest neighbor distance, probably incompatible with crystal translation symmetry, but through two or three similar nearest neighbor distances, see Fig 1.1 and 1.2.

In the cubic DO_3 structure the Sb^{3-} anion has eight A

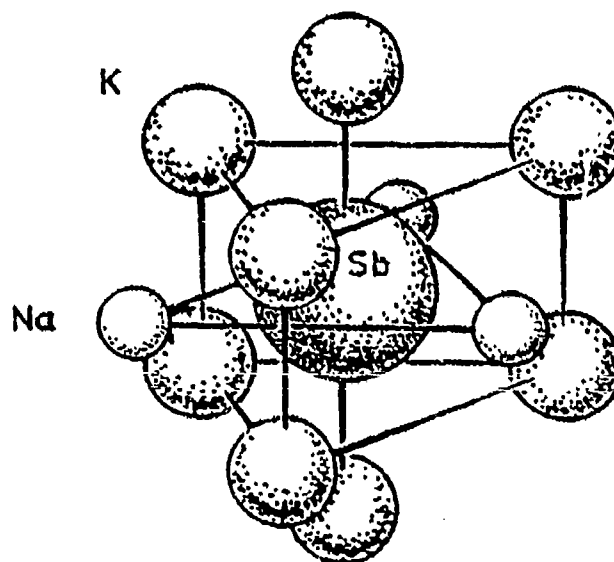
cation nearest neighbors at a distance $a_0\sqrt{3}/4$ in CsCl-structure coordination, and six A' cation nearest neighbors at a distance $a_0/2$ in NaCl-structure coordination, see Fig 5.1 . In Table 5.1 these distances are compared with the sum of ionic radii of corresponding cation and Sb^{3-} anion, for cubic alkali antimonides with known lattice constant, see also Table 5.2 . The observed agreement is very good, nearest neighbor distances represent only a variation less than -4%, +10% in the sum of ionic radii.

The cubic structure is the most stable, allowing at the same time typical ionic NaCl and CsCl structures for nearest neighbors with high coordination numbers, high crystal symmetry, and ion close packing. But in this structure the A'-Sb distance ($a_0/2$) is determined by the A-Sb distance ($a_0\sqrt{3}/4$) . The A-Sb distance is determined by the Coulomb attraction between opposite ions and the repulsive energy from electron wave function overlapping, i.e., by the sum of corresponding ionic radii. Thus when the A' cation is very small like in K_2NaSb , The A'-Sb distance becomes very large compared with the sum of corresponding ionic radii, and opposite ions A'^+ , Sb^{3-} , are not close-packed. In this case the structure may become more stable by an small distortion to the hexagonal structure. In this distortion three of the six nearest neighbor A' cations come closer to the Sb anion and the other three move closer to the next nearest neighbor Sb anions, the six A' cations moving into the same (111) plane. The eight nearest neighbor A cations are maintained essentially in a similar coordination, see Fig 5.2 . During this distortion only one out of the four cubic



COORDINATION FOR Sb NEAREST NEIGHBORS
IN CUBIC DO_3 -STRUCTURE

Fig 5.1 NaCl-structure plus CsCl-structure of nearest neighbors of Sb^{3-} ion. The (001) axis is vertical.



COORDINATION FOR Sb NEAREST NEIGHBORS IN HEXAGONAL Na_3Sb -STRUCTURE

Fig 5.2 Structure of nearest neighbors of Sb^{3-} ion. For comparing with the cubic structure in Fig 5.1 , $\text{K} \rightarrow \text{Na}$, $\text{Na} \rightarrow \text{K}$, and the vertical axis, (000.1), corresponds to the (111) axis in Fig 5.1 .

TABLE 5.1

Comparison of Nearest Neighbor Distances and Ionic Radii for some Alkali Antimonides with cubic DO_3 structure. Ionic radii 0.95, 1.33, 1.69, 2.45 Å are assumed for Na^+ , K^+ , Cs^+ , Sb^{3-} ions. Units: Å

Alkali Antimonide	Nearest Neighbor Distance		Sum of Oposite Ion Radii	
	A-Sb (2)	A'-Sb (6)	A-Sb	A'-Sb
$A_2A'Sb$				
Na_2KSb	3.35	3.87	3.40	3.78
K_2CsSb	3.73	4.31	3.78	4.14
Cs_3Sb	3.96	4.57	4.14	4.14

Ionic radii from ³⁵.

Lattice constant from Table 1.1

Coordination number in parenthesis

TABLE 5.2

Comparison of Hexagonal Na_3Sb and Cubic DO_3 structures for Alkali Antimonides having an hexagonal phase. Ionic radii 0.95, 1.33, 1.48, 1.69, 2.45 Å are assumed for Na^+ , K^+ , Rb^+ , Cs^+ , Sb^{3-} ions. Units: Å

Alkali Antimonide	Hexagonal structure		Cubic structure		Sum of ionic Radii		More stable structure
	A-Sb	A'-Sb	N.N. Distance	A-Sb	A-Sb	A'-Sb	
	(2)	(6)	(3)	(8)	(6)	(8)	
K_2NaSb	3.64	3.72	3.24	3.7*	4.3*	3.78	{H} only
Na_3Sb	3.17	3.48	3.10	3.4*	3.8*	3.40	{H} only
K_3Sb	3.56	3.91	3.48	3.68	4.25	3.78	{H}, {C} unstable
Rb_3Sb	3.73	4.10	3.65	3.81	4.40	3.93	{H}, {C}

Ionic radii from ³⁵.

Lattice constants from Table 1.1.

* from Table 5.1. Coordination number in parenthesis.

three-fold symmetry axis, is maintained, therefore ending up with only hexagonal symmetry.

The hexagonal lattice thus formed, maintains the high coordination numbers, the highest possible crystal symmetry while increasing the average opposite ion close packing. In the hexagonal Na_3Sb structure for $\text{A}_2\text{A}'\text{Sb}$ with $c \leq 2a$, Fig 5.2, Sb^{3-} anion has eight A cation nearest neighbors, two at a distance $c/3$ and six at a similar distance $(c/3)\{3(a/c) + 4\}^{1/2}$. The three nearest neighbor A' cations are at a distance $a\sqrt{3}/3$. In Table 5.2, hexagonal and cubic structure for the alkali antimonides having an hexagonal phase, are studied. Comparison of their nearest neighbor distances with the sum of corresponding opposite ion radii yields the key to explain their relative stability. Considering only Coulomb interaction, i.e., Madelung energy, between Sb nearest neighbors, it is possible to explain why K_2NaSb and Na_3Sb only exist in the hexagonal phase, why in K_3Sb the cubic phase is more unstable than the hexagonal one, and why in Rb_3Sb both phases are about equally stable.

Therefore, the ionic model for alkali antimonides, with ionic radii from values reported in the literature, explains their crystal structures, symmetry, coordination, and lattice parameters. It can also explain the relative stability of the cubic and hexagonal phases.

5.4 Heats of Formation

Standard heats of formation of about 2.0 eV/molec have been reported in the literature⁴⁹ for the alkali antimonides. These values may be explained by the ionic model for these compounds. For example, a charge transfer of about 0.9 will explain that value in Cs_3Sb .

Let us calculate the energy to separate three Cs^+ ions and one Sb^{3-} ion from the Cs_3Sb crystal. Using values in Tables 4.3 and 4.4, to separate a Cs^+ ion will take about 0.9×5.5 eV against the crystal field, minus about 4.0 eV of electronic relaxation energy, minus some energy from ionic relaxation.³⁵ To separate a Sb^{3-} ion will take $0.9 \times 3 \times 17.5$ eV against the crystal field, minus $3^2 \times 2.0$ eV of electronic relaxation energy (proportional to the square of the charge), minus some energy from ionic relaxation. The total energy required is then estimated in about 32. eV minus some ionic relaxation energy. This part of the relaxation energy remains undetermined since the static dielectric constant ϵ_s is not known. But a limit can be estimated. The ratio of the electronic relaxation energy to the total relaxation energy is $(1-1/\epsilon)/(1-1/\epsilon_s)$. Since ϵ is of the order of 10, even if $\epsilon_s = 20$, the ionic relaxation energy would add at most 5% of the electronic relaxation, this means about 1. eV. Therefore, the heat of formation of $3\text{Cs}^+ + \text{Sb}^{3-}$ free ions from the Cs_3Sb solid is about 31. - 32. eV.

The energy to produce a Cs^+ free ion from Cs metal is 0.83 eV to separate an atom³⁵ plus 3.9 eV of ionization energy.³⁵ The energy to form a Sb^{3-} free ion from the metal

is 2.7 eV to separate an atom, minus 1.0 eV of electron affinity to form Sb^- (68,p291), plus about 14 eV or less to form Sb^{3-} , estimated in section 4.2.4 . Therefore, the heat of formation of $3\text{Cs}^+ + \text{Sb}^{3-}$ free ions from the elements in their standard state is at most 30. eV .

The difference between the heat of formation of $3\text{Cs}^+, \text{Sb}^{3-}$ from the solid and from the elements in their standard state is the standard heat of formation of the Cs_3Sb solid, thus about 2 eV/molec .

5.5 Refractive Index

In previous chapter the relation between the refractive index, i.e., the dielectric constant at optical frequencies, and the relaxation energies in the photoemission process has been discussed. Both are very large, due to the high atomic polarizability of the Sb^{3-} ion, see Table 4.6. This high value is mostly due to the loosely bound $\text{Sb}5p^6$ valence electrons. The ionic radius of Sb^{3-} , 2.45 Å, is the larger ionic radius reported.³⁵ Binding energies for valence electrons of Sb^{3-} in alkali antimonides have been estimated in section 4.2.4 in about 2. - 4. eV.

Let us make an estimation of the refractive index for Cs_3Sb from its known electronic structure. Drude relation becomes in quantum theory

$$\epsilon = 1 + 4\pi \frac{e^2}{m} \sum_{ij} N_{ij} \frac{f_{ij}}{\omega_{ij}^2 - \omega^2}$$

where N_i is the density of electrons in state i , f_{ij} is the oscillator strength or matrix element of the electric dipole transition between states i and j , and $\hbar\omega_{ij}$ is the energy difference.

In a first approximation we may consider only valence electrons and virtual transitions only across the Sb5p-Cs6s electric dipole allowed band gap. Other transitions are neglected either because not electric dipole allowed or because large energy gaps. In the sum rule $\sum f_{ij}=1$, we shall also neglect other contributions and take $f_{VC}=1$. For these approximations

$$\epsilon = 1 + \frac{\hbar\omega_p^2}{E_{VC}^2 - \hbar\omega^2}$$

that is a relation frequently used,⁵⁰ where $\hbar\omega_p^2 = 4\pi Ne^2/m$ is the square of the plasmon energy for the valence electron density, and E_{VC} is the average Sb5p-Cs6s energy gap. The band gap $E_G=1.6$ eV reported in the literature is the minimum energy gap between the Sb5p, Cs6s bands, broadened by solid state effects. From our XPS measurements in Cs_3Sb

$$Cs5p_{3/2}, Sb5p \Delta E_B = 10.5 \text{ eV}$$

since, for Cs free atom³¹

$$Cs5p_{3/2}, 6s \Delta E_B = 14.2 \text{ eV}$$

therefore, it might be estimated for Cs_3Sb

$$Sb5p, Cs6s \Delta E_B = 3.7 \text{ eV}$$

sGupta has shown, using Harrison bond orbital model calculations, that solid state effects may broaden and lower the Cs6s levels.⁵¹

Measurements by Spicer, see Fig 4.8 , show an average energy gap

$$\text{Sb}5p, \text{Cs}6s \Delta E_B = 2.8 \text{ eV} \quad \text{exp. in } \text{Cs}_3\text{Sb}$$

Therefore for optical frequencies before the dielectric constant is

dominated by band gap absorption, $\hbar\omega^2 \ll E_{VC}^2$,

$$\epsilon = 1 + \frac{\hbar\omega_p^2}{E_{VC}^2} = 6.6, \quad n = 2.6$$

that is in very good agreement with reported values ^{3,39} For $\hbar\omega_p$

the valence electron density was calculated for $4 \times \text{Sb}5p^6$ electrons

in the unit cell with lattice parameter $a_0 = 9.14 \text{ \AA}$.

VI. ANALYSIS OF XPS RELATIVE INTENSITIES. COMPOSITION AND
STRUCTURE OF $\text{Na}_2\text{KSb}(\text{Cs})$ PHOTOCATHODES

XPS is being developed as a quantitative surface analysis technique. In a simple model a relation between total intensity of a XPS peak and atomic density can be derived. Contributions from intrinsic shake-up structure and extrinsic plasmon energy losses, difficult to predict, impose a limit to the obtainable accuracy. Other sources of error are unknown spectrometer factors and unknown sample inhomogeneities. In general, under certain precautions an accuracy of 10% seems to be obtainable.

We have studied experimental data in the literature from several workers, obtained with essentially the same Varian IEE spectrometer working in the same conditions as in our experiments. These data have been compared with calculated values from theoretical cross sections and with our experimental data on pure metals and CsI, for internal coherence. In this way, relative sensitivity factors for Na, K, Cs, Sb, have been determined. Except for K, XPS peaks with escape depths from 10 Å to 25 Å allow detection of relative composition variations with depth from the surface.

Experimental data obtained and discussion are summarized as follows:

a) It has been possible to detect, in good photocathodes, an small gradient in Sb atomic density, in the sense that peaks coming from the last 15 Å at the surface appear about 10% weaker than expected for an homogeneous sample. This is in agreement with current theories that show good photocathodes with strong band bending favorable to photoemission, due to a p-type bulk because of alkali defect and a n-type surface due to alkali excess.

b) Na_2KSb photocathodes with this stoichiometric composition at the surface, show low sensitivities. Good Na_2KSb photocathodes show an smaller Na content at the surface, in agreement with scanning electron diffraction and X-ray diffraction studies reported recently in the literature, that show the phases Na_2KSb and K_2NaSb present in these photocathodes. Our study show these photocathodes as a Na_2KSb bulk and a K_2NaSb surface layer of the order of 40 Å

c) In $\text{Na}_2\text{KSb}(\text{Cs})$ or S-20 photocathodes Cs is definitively in the bulk, down to a depth larger than 15 Å, i.e., 10 atomic layers. Study of relative intensities of XPS peaks with escape depths from 10 Å to 30 Å, in good photocathodes of 100 - 250 $\mu\text{A}/\text{lm}$, show that Cs is in a surface layer of average depth varying from sample to sample between 20 Å and 50 Å, in most samples of the order of 30 Å. This is in agreement with the X-ray and electron diffraction studies mentioned above, that show the phase K_2CsSb present in S-20 photocathodes.

d) The Cs content in the surface of S-20 photocathodes is quite high, assuming Cs in a surface layer of 20 - 50 Å, the Cs/Sb

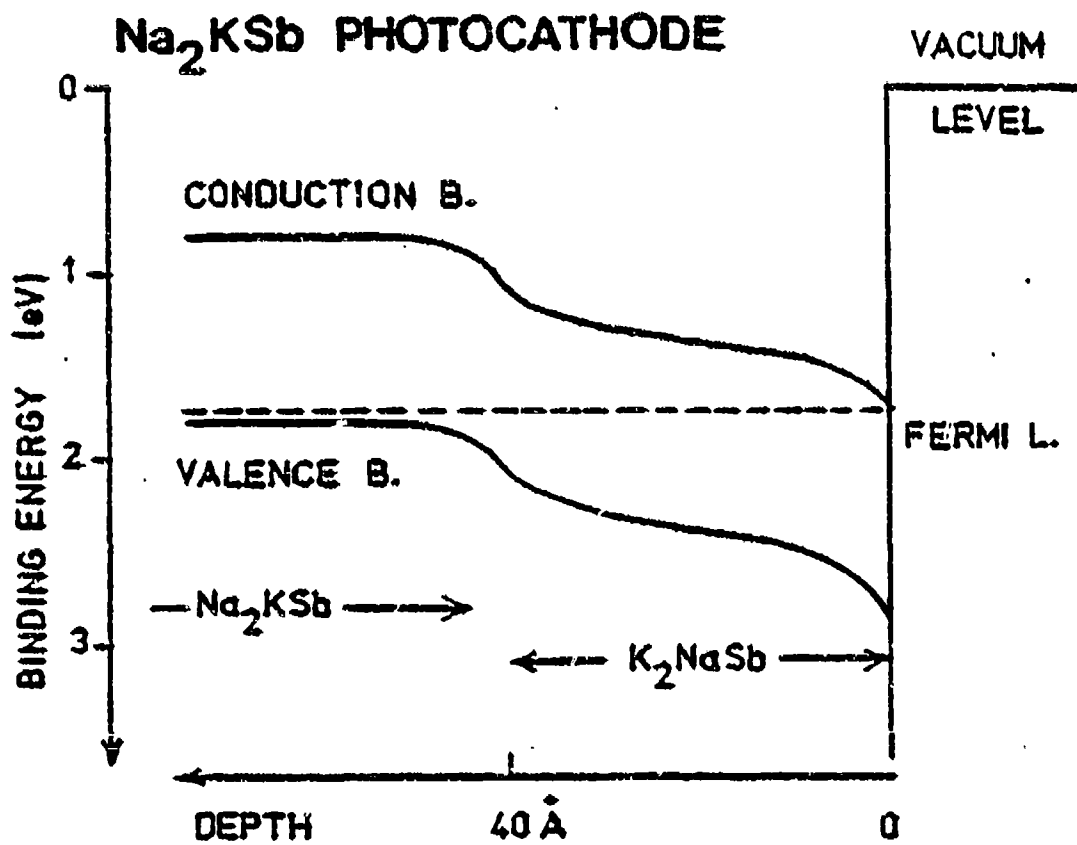


Fig 6.1 Proposed band diagram for Na₂KSb. The K₂NaSb surface layer probably allows the surface to be more strongly n-type.

Na₂KSb(Cs) PHOTOCATHODE

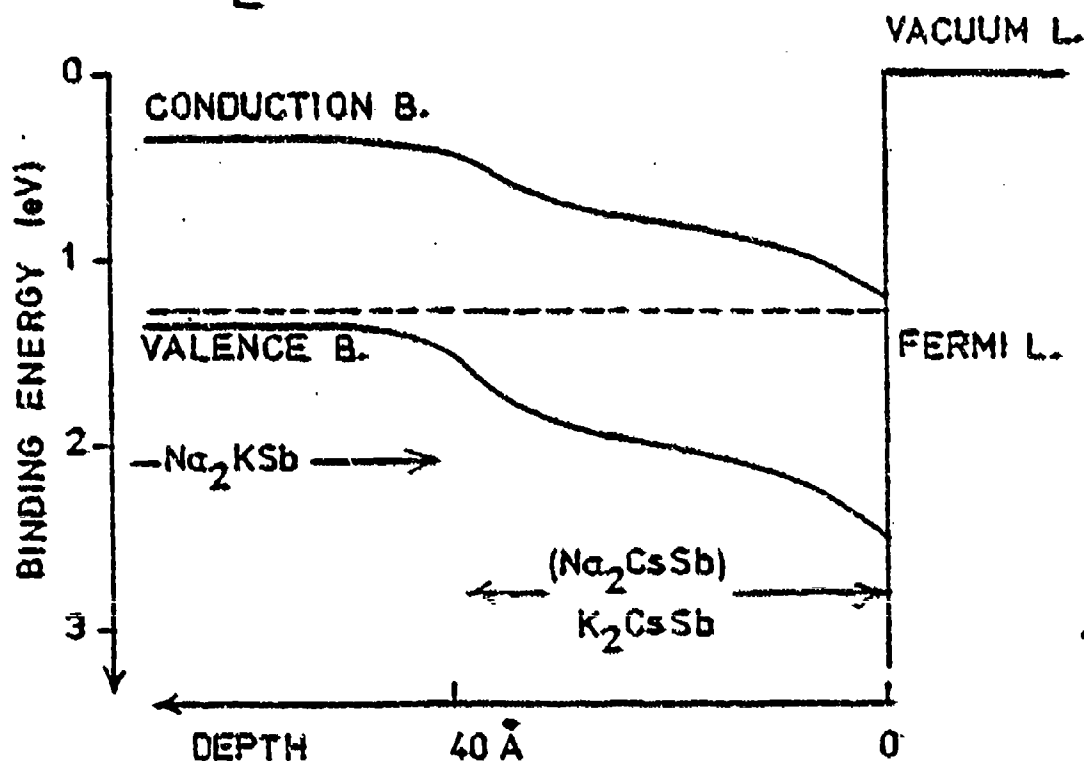


Fig 6.2 Proposed band diagram for Na₂KSb(Cs) or S-20 photocathode. Depending on temperature during surface activation by Cs and Sb deposition, a surface layer of K₂CsSb or K₂CsSb and Na₂CsSb, is formed. K₂CsSb has the optimum properties for a surface layer. It is easily alkali doped, producing n-type material, due to low ion diffusion rate. It has an small photoemission threshold (not including band bending) due to its large lattice constant. And it has a large band gap, and thus, small probability of electron-hole pair creation and large electron mean free paths.

atomic density ratio in this layer is about 1. .

a) In S-20 photocathodes the Na/K atomic density ratio is smaller than 2:1, but much larger than expected from a Na_2KSb bulk under a K_2CsSb surface layer at least 15 Å thick. Studying the Na content of S-20 photocathodes and its variation with depth, our experimental data can only be explained by the presence of a Na_2CsSb phase in the surface layer. Our experimental data for S-20 composition from XPS are well explained by a $(\text{Na}_2\text{CsSb})(\text{K}_2\text{CsSb})$ surface layer 15 - 60 Å thick over a Na_2KSb bulk, in good agreement with results in c) above.

Previous X-ray and electron diffraction studies mentioned above, did not detect the Na_2CsSb phase. This may be explained either because diffraction peaks from this phase are confused with those from K_2CsSb (same crystal structure, similar lattice constant), or more probable, because of different processing schedule. In our processing schedule, we start the final Cs/Sb deposition at 200 - 210°C, a much higher temperature than it is usual, about 160°C, for this part of the process. It is known that both Na and K easily displace Cs, but the temperatures for efficient diffusion are about 200°C and 160°C for Na and K, respectively.

The distances and escape depths reported above are more accurate as relative values than as absolute values. They have been calculated assuming that the mean free path for electrons of 1000 eV kinetic energy is 20 Å, in alkali antimonides.

VII. CONCLUSIONS

Alkali antimonide photocathodes, Na_3Sb , K_3Sb , Cs_3Sb , Na_2KSb , and $\text{Na}_2\text{KSb}(\text{Cs})$, were studied using X-ray photoemission and Auger electron spectroscopy under ultrahigh vacuum conditions.

Our measurements were studied together with known data for free ions and atoms, pure metals, and alkali halides, by means of a simple point charge electrostatic model. Correlation of shifts in photoelectron and Auger electron spectra, allows to determine independently both binding energies and relaxation energies due to electronic polarizability.

The results of the study were compared with known properties and UPS data of alkali antimonides and alkali halides.

The conclusions of this study are:

- 1) Both, electron binding energies and photoemission relaxation energies, show alkali antimonides as ionic compounds, with valence electrons strongly localized on the Sb^{3-} ions. Charge transfer was estimated to be 0.8 or larger.
- 2) Valence band region XPS spectra confirm this, showing essentially no mixing of alkali and antimony levels. The less bounded alkali p levels appear at least 10 eV below a clearly defined valence band, only 2 - 3 eV wide. Proposed models for crystal binding, involving formation of $(\text{sp})^3$ hybridized orbitals, as in III-V covalent compounds, are ruled out.
- 3) The ionic model for alkali antimonides show the top of the valence band around 2 - 4 eV below the vacuum level. The difference

with experimental photoemission thresholds, about 1 eV smaller, was explained by surface band bending effects included in their measurements.

4) The ionic model also explains the dependence of the photoemission threshold on lattice parameter and ionicity, thus explaining observed trends in experimental values.

5) Known similarities between the energy distribution in UPS of alkali antimonides and alkali halides, as well as the differences between them and covalent solids were explained by the electric dipole allowed band gap between the strongly localized, atom-like valence shells of the anions and the conduction band formed from the empty valence s orbitals of the alkalis, in those ionic compounds.

6) Experimental hole mobility values confirmed that explanation.

7) Known heats of formation seems to be explainable by the ionic model. A calculation for Cs_3Sb yields a value in very good agreement with the experimental one.

8) The large electronic polarizability of Sb^{3-} ions explains the large refractive index of alkali antimonides. A calculation for Cs_3Sb from its known electronic structure yields a value in very good agreement with the experimental one.

9) Crystal structures of alkali antimonides were explained as typically ionic. Known ionic radii and electrostatic Madelung energy considerations explain their crystal structures, symmetry, ion coordination, and lattice parameters. It can also explain the

relative stability of their cubic and hexagonal phases.

10) Madelung energy considerations can also explain why some alkali antimonides are strongly p-type. In alkali antimonides $A_2A'Sb$ where cations A and A' are comparable in size but where still the cubic phase is more stable, the cations have a tendency to be displaced from their theoretical lattice positions. This seems to facilitate ion diffusion and vacance formation, producing an equilibrium configuration where the bulk is alkali deficient, p-type, and the surface has excess of alkali, being n-type. The driving force for these phenomenons seems to be maximization of Madelung energy.

11) Some unusual experimental results found in X-ray and electron diffraction studies of Cs_3Sb and Na_2KSb give support to the explanation proposed in 10), above, and are themselves explained.

12) The good properties of alkali antimonides as photocathodes are explained by their ionicity. As ionic compounds, band gap absorption is strong and structureless. The small electron binding energies and large electronic polarizability of the Sb^{3-} ion, both due to its valence shell electrons, explain their small photoemission thresholds.

13) The very good photoemission properties of Cs_3Sb and Na_2KSb are explained by surface band bending, whose relation with crystal structure and Madelung energy is pointed out in 10), above.

14) From our XPS quantitative surface analysis, a model for Na_2KSb photocathode is proposed, where a thin surface layer of

K_2NaSb is formed. This probably allows the surface to be more strongly n-type.

15) An n-type surface layer is also the explanation of the extraordinary photoemission properties of $Na_2KSb(Cs)$ or S-20 photocathodes. In this case, while surface activation by Cs and Sb deposition, a surface layer of K_2CsSb (probably, sometimes also Na_2CsSb) is formed. This phase, K_2CsSb , has the optimum properties for a surface layer. It is easily alkali doped, producing n-type material, due to low ion diffusion rate. It has small photoemission threshold (not including band bending) due to its large lattice constant. And it has a large band gap, and thus, small probability of electron-hole pair creation and large electron mean free path.

16) From our XPS quantitative surface analysis of Na_2KSb and $Na_2KSb(Cs)$ photocathodes, the surface layer mentioned in 14), 15) above, is estimated in 30 - 40 Å .

BIBLIOGRAPHY

1. P. Görlich, Z. Phys. 101, 335 (1936).
2. A. H. Sommer, IRE Trans. Nucl. Sci., 3, 86 (1956).
3. A. H. Sommer, "Photoemissive Materials", (Wiley, New York, 1968).
4. W. E. Spicer, Phys. Rev. 112, 114 (1958).
5. M. Hagino and T. Takahashi, Phys. Stat. Sol. 17, 609 (1966).
6. J. C. Robbie and A. H. Back, J. Phys. D: Appl. Phys. 6, 1381 (1973).
7. K. H. Jack and M. M. Wachtel, Proc. Roy. Soc. (London) A239, 46 (1957).
8. G. Gutzmann et al., Z. Anorg. Allgem. Chem. 309, 210 (1961).
9. J. J. Scheer and P. Zalm, Philips Res. Repts. 14, 143 (1959).
10. A. H. Sommer (private communication).
11. C. D. Wagner, Analytical Chemistry 47, 1201 (1975).
12. G. K. Wertheim, C. W. Bates, Jr., D. N. E. Buchanan, "Electronic Structure of CsAu", accepted for publication in Solid-State Communications.
13. M. Campagna, G. K. Wertheim and E. Bucher, Structure and Bonding 30, 99 (1976).
14. K. S. Kim, T. J. O'Leary, N. Winograd, Anal. Chem. 45, 2213 (1973).
15. S. P. Kowalczyk et al., Phys. Rev. B9, 381 (1974).
16. J. H. Scofield, Jour. for Electron Spectr. 8, 129 (1976).
17. W. A. Harrison (unpublished results).

19. W. E. Spicer, J. Appl. Phys. 44, 1112 (1973).
20. T. Ichikawa, Japanese Jour. App. Phys. 14, 885 (1975).
21. H. Hillig et al., Z. Phys. 26, 225 (1974).
22. D. A. Shirley et al., Phys. Rev. B 15, 544 (1977).
23. CRC Handbook of Chemistry and Physics, 58th ed. (1978).
24. A. Barrie and F. J. Street, Jour. Electr. Spectroscopy 7 (1979).
25. P. H. Citrin and T. D. Thomas, Jour. Chem. Phys. 57, 4446 (1972).
26. W. E. Morgan et al., Jour. Amer. Chem. Soc. 95, 751 (1973).
27. N. F. Mott and M. J. Littleton, Trans. Faraday Soc. 34, 485 (1938).
28. L. G. Peterson and S. E. Karlson, Physica Scripta 16, 425 (1977).
29. C. D. Wagner, in "Handbook of X-Ray and Ultraviolet Photoemission Spectroscopy" (1977) D. Briggs (Editor).
30. K. Siegbahn, "Electron Spectroscopy - An Outlook", Uppsala Univ. UUIP-880 (1974).
31. H. Peterson et al., J. Phys. B8, 31 (1975).
32. N. G. Krishnan et al., J. Phys. F7, 2623 (1977).
33. B. C. Moisewitsch and P. G. Burke, "Atomic Processes and Applications", North Holland (1976).
34. B. I. Lundqvist, Phys. Kond. Mat., 9, 236 (1969).
35. N. F. Mott and R. W. Gurney, "Electronic Processes in Ionic Crystals", Dover (1964).
36. U. Gelius, J. Elec. Spec. 5, 985 (1974).

37. F. Wooten and W. E. Spicer, Surf. Sci., 1, 367 (1964).
38. P. A. Lindfords, Thesis, Univ. of Minnesota (1977).
39. P. Dolizy et al., Acta Electronica, 20, 265 (1977).
40. A. A. Dowman et al., J. Phys. D 8, 69 (1975).
41. D. G. Fisher et al., J. Appl. Phys. 45, 487 (1974).
42. E. A. Taft and H. R. Philipp, Phys. Rev., 115, 1583 (1959).
43. H. R. Philipp et al., Phys. Rev. 120, 49 (1960).
44. W. F. Krolikowski, Ph.D. Thesis, Stanford Univ. (1967).
45. T. H. DiStefano, Ph.D. Thesis, Stanford Univ. (1970).
46. T. H. DiStefano and W. E. Spicer, Phys. Rev. B7, 1554 (1973).
47. W. E. Spicer, in "Optical Properties of Solids", F. Abeles
(Editor), North Holland (1972).
48. W. E. Spicer, in "Optical Properties of Solids, New Developments",
B. O. Serphin (Editor), North Holland (1976).
49. E. Kinsky, Adv. Electron Phys. 33A, 357 (1973).
50. D. R. Penn, Phys. Rev. 128, 2093 (1962).
51. D. DasGupta, Ph.D. Thesis, Stanford Univ. (1978).

APPENDIX A

THE BASIC PHYSICS OF X-RAY PHOTOELECTRON SPECTROSCOPY

A.1 Electron Binding Energies

Photoemission from a N -electron system (solid) leads to a manifold of states of the N -electron system in which one electron is unbounded. In the limit of infinite separation between the solid and the photoemitted electron, each of these states can be described as a $(N-1)$ -electron state and a single free electron of kinetic energy

$$E_K = h\nu - E_f^{N-1} + E_i^N$$

where $h\nu$ = photon energy, and E_i^N , E_f^{N-1} are the initial and final state energies of the solid. The binding energy of the orbital from which the electron was ejected is defined as

$$E_B = E_f^{N-1} - E_i^N = h\nu - E_K$$

In this description, which is completely rigorous and can be closely related to empirical quantities, there is no need for the concept of relaxation energy. No detailed description is given of the initial or final state, and we do not allude to one-electron orbitals.

PRECEDING PAGE NOT FILMED
BLANK

Electronic structure theories are usually developed in terms of one-electron orbitals, with the coordinates of the electron coupled through self-consistent field formulations (e.g., the Hartree-Fock method). These orbitals can be described in terms of a basis set with quantum-number designations $1s$, $2s$, $2p_{1/2}$, $2p_{3/2}$, etc. These orbital designations also label the photoelectron peaks. Moreover, solving the Hartree-Fock equations yield a set of parameters ϵ_j termed orbital energies. Koopmans theorem showed that these orbital energies would be the binding energies $E_p(j)$ if

a) there were not change in the other orbitals while an electron was removed from orbital j , and

b) if the Hartree-Fock method gave a true description of the system.

Corrections for b), i.e., differential correlation and relativistic energies, which are of course not included in the Hartree-Fock formulation, are usually very small and thus neglected. Moreover since working with energy differences usually these corrections nearly cancel out.

With respect to a) several approximations can be considered. The first one is the "three step model" for bulk photoemission. The photoemission event is split up in three processes, i) excitation of one electron to a higher energy state E_f^{N-1} after absorption of a photon,

ii) transport of the electron through the solid, and iii) escape of the electron through the surface barrier. During transport ii) and escape iii) many energy losses may occur due to electron-electron inelastic scattering, creation of extrinsic plasmons, etc. All these processes produce a complex final state structure on E_f^{N-1} very hard to predict. Measuring the kinetic energy of photoelectrons elastically scattered only, redefines the binding energy

$$E_B = E_f^{N-1} - E_i^N$$

and simplifies the photoemission event to a situation closer to the ideal one stated in a). Moreover in XPS the photoelectron in the final state is free-electron-like with no momentum-conservation selection rule, due to the high photoexcitation energy. In fact for most situations encountered in photoemission the approximation

$$E_B(j) = \epsilon_j \quad (\text{proper sign included in } \epsilon_j)$$

is close enough for diagnostic purposes. The departure from this equation defines the relaxation energy $E_R(J)$

$$E_B(j) = \epsilon_j - E_R(J)$$

Creation of phonons, electron-hole pairs, and intrinsic plasmons during photoexcitation contribute to $E_R(J)$.

Depending on the process relative time scale different processes might occur. In one extreme is the sudden approximation. In the shake-up and shake-off processes in this approximation the resulting state after photoemission is not an eigenstate of the ion, the ion is left in an excited state. By energy conservation, the energy of the emitted electron will be reduced by the excitation energy. In the other extreme is the adiabatic approximation. During the photoemission process the other electrons will relax towards the positive hole, screening its positive charge and so imparting adiabatically additional energy to the photoemitted electron.

A.2 Multiplet Splitting

In many situations, the final state of the atom with a hole in the state j is not a unique one in terms of the individual atomic-level quantum numbers. This is because each eigenstate is characterized by a definite value of the total quantum numbers L and S and there can be more than one individual subshell configuration that can correspond to these L, S values. The difference in energy between such possible states can give rise to a number of components in the XPS spectrum, instead of a single peak as previously assumed.

A.3 Configuration Interaction (CI) Effects

Configuration Interaction can be considered to be a generalized many-electron process of which both multiplet and shake-up effects are special cases. Arguing exactly in the same way as in describing the multiplet process, one can see that the simple two-electron shake-up

model may not be adequate in general. Instead, the final state may be any one of a number of more complex rearrangements consistent with the relevant selection rules.

APPENDIX B

AUGER ELECTRONS AND THE AUGER PARAMETER

After emission of one electron by the photoexcitation energy $h\nu$ the system is left in a state with a core hole in the orbital j with energy $E_f^{N-1} = E_i^{N-1}(J)$ that is the initial state of the Auger process in which the hole jumps to the orbital l $\epsilon_l < \epsilon_j$, and the energy difference is taken up by the Auger emitted electron initially in the orbital m , $\epsilon_m < \epsilon_j - \epsilon_l$, whose kinetic energy is

$$K_{JLM} = -E_f^{N-2}(L,M) + E_i^{N-1}(J) - E_D(m,L)$$

where $E_f^{N-2}(L,M)$ is the energy of the final $(N-2)$ -electron system with a hole in the l orbital and in the m orbital, and the equation defines the binding energy of the orbital in the $(N-1)$ -electron system from which the electron was ejected.

In Koopmans theorem approximation

$$K_{JLM} = \epsilon_j(J) - \epsilon_l(J) - \epsilon_m(L)$$

where $\epsilon_m(L)$ is the Hartree-Fock energy of the orbital m of the system with a hole in the orbital l . If relaxation energy corrections are included

$$K_{JKL} = \epsilon_j(J) - \epsilon_l(J) - \epsilon_m(L) + E_R(L,M) - E_R(J)$$

PRECEDING PAGE NOT FILMED

If the kinetic energy of the photoelectron

$$E_K(j) = h\nu - \epsilon_j + E_R(J)$$

is subtracted from K_{JLM} , the Auger Parameter is defined by

$$\alpha_{JLM}^j = K_{JLM} - E_K(j) =$$

$$= \epsilon_j(J) + \epsilon_j - \epsilon_L - \epsilon_M(L) + E_R(L,M) - 2E_R(J) - h\nu$$

The Auger parameter was defined and studied by Wagner¹¹ to discuss theoretical and experimental data related to effects of extraatomic relaxation in $E_R(J)$ and $E_R(L,M)$. The importance of the Auger parameter is shown when studying the differences (shifts) among $E_K(j)$ and K_{JLM} of the ion in different solids or different-chemical environments. Many workers have shown that in many situations where the point charge electrostatic model is approximate enough, the shifts in the orbital energies ϵ_j due to valence charge transfer (chemical shifts) and crystal field are the same for all core orbitals

$$\Delta\epsilon_j = \Delta\epsilon_L = \Delta\epsilon_M(L) = \Delta\epsilon_L(J) = \Delta\epsilon_j(J) = \Delta\epsilon$$

Intraatomic relaxation (roughly chemical environment independent) cancel out in ΔE_R and for extraatomic relaxation due to electronic polarizability

$$\Delta E_R(L,M) = 4\Delta E_R(J) = 4\Delta E_R$$

therefore

$$\Delta E_K(j) = -\Delta e + \Delta E_R = -\Delta E_D(j)$$

$$\Delta K_{JLM} = -\Delta e + 3\Delta E_R$$

$$\Delta a_{JLM}^j = 2\Delta E_R$$

Thus measuring Auger parameter shifts in XPS allows us to measure the extraatomic relaxation energy contribution to the binding energy shifts, and to give a more accurate computation of charge transfer or ionicity. Very often E_R is very small, <2 eV, and ΔE_R even smaller and hence so many times E_R has been forgotten in the literature when correlating binding energy shifts with valence charge transfer.

APPENDIX C

THE POINT CHARGE ELECTROSTATIC MODEL

In the point charge electrostatic model the core electrons in the ions are considered strongly localized (point charges) and so the orbital energies are easily calculated assuming the ions in the classical Coulomb potential of the crystal or Madelung potential $-\phi/R$ where R is the nearest neighbor distance and ϕ is a scalar closely related to the Madelung constant. So, if

$$E_B^{FI}(j) = \epsilon_j^{FI} - E_R^{FI}(j)$$

for the free ion, then

$$E_B^{XI}(j) = \epsilon_j^{FI} - \frac{q_\phi}{R} - E_R^{XI}(j)$$

for the ion in the crystal, q being the charge in the ion. When writing E_B^{XI} a repulsion potential term or wave function renormalization into the smaller space in the solid, has been neglected. This term has been calculated to be about 1 eV or smaller for alkali halides. For alkali antimonides it is even smaller.

The relaxation term E_R^{XI} can be split into an intraatomic relaxation term and an extraatomic relaxation or lattice term

$$E_R^{XI} = E_R^{(atomic)} + E_R^L$$

In the point charge electrostatic model intraatomic relaxation energy for the free ion, the ion in the crystal and the free atom are all approximately the same for all core orbitals, and thus

$$E_S^{XI}(j) = E_B^{FI}(j) - \frac{q\phi}{R} - E_R^L$$

The extraatomic or lattice relaxation term is due to the relaxation of the electronic charge on the other ions in the lattice towards the core hole created by photoemission. Only electronic polarization should be considered because of the time scale of the photoemission process, about 10^{-17} sec. The relaxation term due to lattice electronic polarization is

$$E_R^L = \frac{1}{2} \left(1 - \frac{1}{\epsilon}\right) \frac{e^2}{r}$$

where ϵ is the dielectric constant for optical frequencies, i.e., $\epsilon = n^2$, n = refractive index, and r is the effective polarization radius of the ion which should be of the order of the interatomic distance R_j

$$\begin{array}{ll} r = 0.6R & \text{for cations} \\ r = 0.9R & \text{for anions} \end{array} \quad \text{in alkali halides}$$

In the same approximation, for the Auger electrons

$$K_{JLM}^{XI} = K_{JLM}^{FI} + \frac{q\phi}{R} + E_R^L(L,M) - E_R^L(J)$$

where XI stands for the ion in the crystal, FI for the free ion, and $E_R^L(L,M)$ is the electronic polarization of the crystal lattice towards the two holes in the l and m orbitals. In the point charge electrostatic model polarization energies are orbital independent and proportional to the square of the charge and

$$E_R^L(L,M) = 4E_R^L$$

Therefore

$$K_{JLM}^{XI} = K_{JLM}^{FI} + \frac{q_0}{R} + 3E_R^L$$

and

$$a_{JLM}^{XI} = a_{JLM}^{FI} + 2E_R^L$$

When putting together in a solid anions and cations of not too large electronegativity differences there is always some valence electron redistribution between opposite ions and total ionicity cannot be assumed. In a first approximation

$$E_R^{XI}(j) = E_R^A(j) + k\Delta q - \frac{q_0}{R} - E_R^L$$

where k is the two-electron integral between core and valence electrons. In the point charge approximation k is assumed to be independent of

crystal structure, i.e.; the valence charge Δq on the ion is treated classically as screening charge spherically distributed at a valence shell radius $r_v = 14.4 \text{ Å} \text{ eV/e}$ ($1/k$), where the corresponding coupling constant is given. In this first approximation k can be calculated from the free ion and atom values

$$k = (E_{\text{FI}}^{\text{FI}} - E_{\text{B}}^{\text{A}})/q$$

where q is the charge in the free ion. The Auger electron energy is

$$K_{\text{JLM}}^{\text{XI}} = K_{\text{JLM}}^{\text{A}} - k\Delta q + \frac{q\phi}{R} + 3P_{\text{R}}^{\text{L}}$$

and the Auger parameter is given by

$$\alpha_{\text{jJLM}}^{\text{XI}} = \alpha_{\text{jJLM}}^{\text{A}} + 2E_{\text{R}}^{\text{L}}.$$

It should be pointed out that for ionic solids the electron binding energy shifts with respect the atomic state are very small even if Δq is very large. It is well known that for most crystalline structures the Madelung crystal potential

$$\phi \sim (1.7 \pm 0.5) \times 14.4 \text{ Å} \text{ eV/e}$$

and since the valence shell radius $r_v \sim R/2$, therefore the chemical shift

$$\Delta q(k - \frac{q}{R}) \sim \Delta q(\frac{1}{r_v} - \frac{1.7}{R}) \times 14.4 \text{ \AA eV/e}$$

is of the order of 1-3 eV, in spite of $k\Delta q$ being of the order of 10 eV. This also shows that in any valence charge transfer calculation, even if the binding energy shift and polarization energy are known to within an eV, the error in Δq may become about 30%.

APPENDIX D

MADELUNG CRYSTAL FIELD FOR THE CUBIC DO_3 STRUCTURE

The Madelung potential infinite sum for the DO_3 lattice can be rearranged in three infinite sums, each one corresponding to a lattice, NaCl or cubic ZnS, whose Madelung constant is known.

Details of the calculation will not be given in this summary.

Referring to Na_2KSb , Fig 1.1, the constant Φ in the Madelung potential Φ/R , has the values, for $R = a_0\sqrt{3}/4$,

$$\Phi_{\text{Sb}} = 1.514 \frac{q_{\text{K}}}{q_{\text{Sb}}} + 3.276 \frac{q_{\text{Na}}}{q_{\text{Sb}}}$$

$$\Phi_{\text{K}} = 1.514 - 0.248 \frac{q_{\text{Na}}}{q_{\text{K}}}$$

(units: 14.4 eV.Å/e)

$$\Phi_{\text{Na}} = 1.763$$

(q's = ion valence charges)

Since $q_{\text{Sb}} = q_{\text{K}} + 2q_{\text{Na}}$, and assuming $q_{\text{K}} = q_{\text{Na}}$

$$\Phi_{\text{Sb}} = 1.596 \qquad \Phi_{\text{K}} = 1.266 \qquad \Phi_{\text{Na}} = 1.763$$

The unusual small value of the Madelung potential at the cation octahedral site, K in Na_2KSb , is due to the large distance from Sb ions and to the eight cation nearest neighbors. This represents a difference of about 2 eV in the Madelung energy between the two cation sites, not found in any other ionic compounds.